Deutsche Fassung:
Beschluss der Curricula-Kommission für Bachelor-, Master- und Diplomstudien vom 10.11.2008
Genehmigung des Senates am 1.12.2008

EIDESSTATTLICHE ERKLÄRUNG

Ich erkläre an Eides statt, dass ich die vorliegende Arbeit selbstständig verfasst, andere als die angegebenen Quellen/Hilfsmittel nicht benutzt, und die den benutzten Quellen wörtlich und inhaltlich entnommenen Stellen als solche kenntlich gemacht habe.

Graz, am ....
(Unterschrift)

Englische Fassung:

STATUTORY DECLARATION

I declare that I have authored this thesis independently, that I have not used other than the declared sources / resources, and that I have explicitly marked all material which has been quoted either literally or by content from the used sources.

....
date (signature)

Michael Naderer

Impact of donor doping and solid solution formation on the lead-free ferroelectric material $Bi_{0.5}Na_{0.5}TiO_3$

DISSERTATION

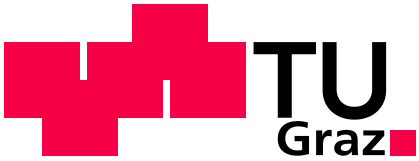
zur Erlangung des akademischen Grades eines Doktors der Technischen Wissenschaften (Dr. techn.)

an der

Technischen Universität Graz

Betreuer: Ao.Univ.-Prof. Dipl.-Ing. Dr.techn. Klaus Reichmann
Institut für Chemische Technologie von Materialien
Christian Doppler Laboratorium für ferroische Materialien





Graz, 2013

Acknowledgement

At first, I want to thank the supervisor of this work, Prof. Klaus Reichmann for his advices, help and support in finishing this project. The hints and pushes given in several discussions were highly welcome and helped to escape from dead-ends. I would also like to thank Klaus for his great way of leading our working group and the creation of a very open-minded working space, where every thought could be spoken and discussed.

I'd also like to thank the collaborators working at TDK-EPC for inputs and advices during our project meetings. Without the sample preparation at TDK-EPC the results section would be full of emptiness.

At the Graz University of Technology, I'd especially like to thank my colleagues at the Christian Doppler Laboratory for Advanced Ferroic Oxides for all the help, input and coffee breaks. Without you, this work would not have been possible. A special thank goes to our intern Michael Freiberger, who helped a lot during the sample preparation.

The majority of XRD patterns were measured by Prof. Mautner, whose input and help interpreting the results was always appreciated.

For the very beautiful SEM images, I want to thank Sanja Simic from FELMI-ZFE.

A special thank belongs to Natascha, who endured me during hard times and writing this work. Thank you for being like you are, I wouldn't want you any way else. My family, especially my parents, I want to thank for the opportunity to study and the support during the last years.

I also like to thank all my friends for offering distraction from work and consolation at hard times.

This work was supported by EPCOS OHG, a group company of the TDK-EPC Corporation. Funding was provided by the Christian Doppler Association, Austria, and the Ministry of Economy, Family and Youth, Austria.

Table of contents

Acknowledgement 3

Kurzfassung 6

Abstract 7

1. Covered scientific questions 8

2. Introduction 9

2.1. Theoretical aspects 9

2.2. Piezoelectric and dielectric parameters 11

2.3. Introduction to the lead-free (1-x)BNT-xBKT system 15

2.4. Modifications and proposed influences 17

2.4.1. Substitution of single elements 18

2.4.2. Solid solutions of perovskites and non-perovskite materials 19

2.5. Donor doping and single element substitutions 20

2.5.1. A-site donor doping with Ca 20

2.5.2. A-site donor doping with Ce 21

2.5.3. B-site donor doping with Nb 21

2.5.4. Ti-substitution with Ge 21

2.5.5. Ti-substitution with Sn 22

2.5.6. Ti-substitution with Zr 22

2.5.7. Ti-substitution with Li / V 23

2.5.8. Ti-substitution with Li / W 23

2.6. Solid solutions with other perovskites and non-perovskites 24

2.6.1. BNT-CT 24

2.6.2. BNT-CG 24

2.6.3. BNT-CS 24

2.6.4. BNT-CZ 24

2.6.5. BNT-MT 25

2.6.6. BNT-MG 25

2.6.7. BNT-MS 25

2.6.8. BNT-MZ 25

3. Experimental section 26

3.1. Sample preparation 26

3.2. Sample characterization 30

3.2.1. X-Ray diffraction 30

3.2.2. Scanning electron microscopy / Energy dispersive X-Ray spectroscopy 30
3.2.3. Small signal electrical measurement 31
3.2.4. Hysteresis loops 31
4. Results 32
4.1. The starting point: BNT 32
4.2. BNT-25BKT 36
4.3. Substitutions and donor doping on A- and B-site 42
4.3.1. Donor doping with calcium 42
4.3.2. Donor doping with cerium 45
4.3.3. Donor doping with niobium 48
4.3.4. Substitution of titanium with germanium 50
4.3.5. Substitution of titanium with tin 52
4.3.6. Substitution of titanium with zirconium 55
4.3.7. Substitution of titanium with lithium / vanadium 58
4.3.8. Substitution of titanium with lithium / tungsten 60
4.4. Solid solutions of BNT with other compounds 63
4.4.1. Solid solution of BNT and CT 63
4.4.2. Solid solution of BNT and CG 66
4.4.3. Solid solution of BNT and CS 67
4.4.4. Solid solution of BNT and CZ 68
4.4.5. Solid solution of BNT and MT 69
4.4.6. Solid solution of BNT and MG 73
4.4.7. Solid solution of BNT and MS 74
4.4.8. Solid solution of BNT and MZ 75
4.5. Summary of findings 76
4.5.1. Combination of findings to a prototype material 78
4.5.2. Detailed results, temperature dependant hysteresis loops 78
5. Conclusion 86
6. References 88
7. Image directory 91
8. Table directory 94
9. Equation directory 95
10. Appendix 96

Kurzfassung

Diese Arbeit behandelt die Auswirkungen von verschiedenen Dotierungen in $Bi_{0.5}Na_{0.5}TiO_3$ (BNT). Ziel war, den ferroelektrischen Anteil der Polarisationshysterese soweit wie möglich zu reduzieren, d.h. die von der Hysterese eingeschlossene Fläche möglichst stark zu verringern, ohne die maximale Polarisation stark zu dezimieren. Als Dotierungsmethoden stehen bei ferroelektrischen keramischen Materialien isovalente Dotierung, Akzeptor- und Donordotierung sowie die Bildung von festen Lösungen zur Verfügung. Durch den Einsatz von verschiedenartigen Dotierungen kann das ferroelektrische Verhalten gezielt verändert werden, um zu den gewünschten Eigenschaften zu gelangen. Isovalente Dotierung und feste Lösungen beeinflussen das Ausgangsmaterial BNT durch den Einbau von Ionen mit unterschiedlichen Massen, Radien und Elektronenstrukturen. Akzeptor- und Donordotierungen ziehen ihre Wirkung darüber hinaus aus ihrem Einfluss auf die Defektchemie im Material.

Zur isovalenten Dotierung wurde Ti in BNT durch Zr, Sn und Ge ersetzt. Feste Lösungen aus BNT wurden mit Bismut-Alkali-Titanaten, Erdalkali-Germanaten, Erdalkali-Titanaten sowie Erdalkali-Stannaten hergestellt, die zur Erforschung der Auswirkungen der einzelnen Bestandteile herangezogen wurden. Von einer Dotierung mit Akzeptoren wurde in dieser Arbeit abgesehen, da zur Wahrung der elektronischen Neutralität des Materials Sauerstoffleerstellen entstehen können, die für die bei erhöhten Temperaturen auftretende Leitfähigkeit von keramischen Bauteilen verantwortlich gemacht werden und die Lebensdauer von Bauelementen herabsetzen können. Als Donordotierungen kamen Calcium, Cer und Niob zum Einsatz. Weitere Varianten der Dotierung wie gezieltes Abweichen von der Sollstöchiometrie wurden ebenfalls auf ihre Einflüsse untersucht.

Die aus diesen Versuchsserien gewonnenen Erkenntnisse wurden in einem Prototypmaterial verarbeitet, welches sich durch eine sehr schlanke Polarisationshysterese mit hoher maximaler Polarisation sowie durch enorme Dehnung, induziert durch das elektrische Feld, auszeichnet.

Abstract

The scope of this work was to clarify the influence of various doping agents in the lead-free ceramic system $Bi_{0.5}Na_{0.5}TiO_3$ (BNT). The aim was to reduce the ferroelectricity of BNT to obtain a very narrow hysteresis loop without losing the high maximum polarization of BNT. The properties of ferroelectric materials are influenced by the addition of dopants as is shown in literature. Doping can be carried out mainly in four different ways; isovalent doping, acceptor doping, donor doping and the formation of solid solutions. Isovalent doping and the formation of solid solutions introduce ions with differing mass, radius or electronic structure in the material. Acceptor and donor doping affect the defect chemistry in the material.

For isovalent doping Ti in BNT was substituted by Zr, Ge and Sn. Solid solutions of BNT with bismuth alkaline titanates, earth alkaline germanates, stannates and titanates were prepared and investigated. Acceptor doping has not been investigated in this study, because the charge neutrality requires the formation of oxygen vacancies, which are responsible for high conductivities at elevated temperatures and reduce the lifetime of components. As donor dopants, calcium, cerium and niobium were used. The influence of intended nonstoichiometry was also clarified.

The knowledge gained from these series of experiments was then used to prepare a prototypic material, which shows a narrow hysteresis loop combined with a very high maximum of polarization and a giant strain induced by the applied electric field.

1. Covered scientific questions

Ferroelectric materials and components for applications in electronics are widely known in the literature and are in use for more than half a century. The ferroelectric compositions which have been explored most extensively and have got widely applied are barium titanate (BT) and lead zirconate titanate (PZT). Whereas BT is found in the majority of multilayer ceramic capacitors, PZT is the basis for actuators, sensors, generators or transducers based on the direct or inverse piezoelectric effect. With the Restriction of Hazardous Substances Directive (RoHS-directive[1]) coming into effect at the beginning of the 21st century, the use of lead is restricted because of its negative environmental impacts and the concern of health risks.

Lead-free materials like BT or BNT often show inferior properties compared to doped PZT but with the RoHS-directive in place, these materials gather rising interest in the scientific community[2][3].

Up to now, the most often used lead-free material is BT for energy storage with capacitors. Unfortunately the charge storage capacity of BT gets reduced at high fields, because of a massive reduction of the relative permittivity. For such conditions antiferroelectric ceramics based on lanthanum doped Lead-Zirconate-Titanate (PLZT) are applied. BNT is a promising candidate to replace lead in applications like actuator components or high density energy storage in energy conversion applications, e.g. hybrid vehicles, because of the occurrence of a so called nonpolar or antiferroelectric phase, which is located between the ferroelectric phase and the paraelectric phase. The transition temperature is at approximately 190 °C for undoped BNT.

The most important question answered in this work is the influence of different doping concepts on the electrical parameters in BNT. The goal is to maximize the stability range of the nonpolar or antiferroelectric phase in BNT. This phase shows excellent field induced polarization together with low dielectric losses, both favorable properties for the mentioned applications.

The use of dopants has been widely studied in literature, usually with the aim of maximizing the ferroelectric properties and hardening the material. We follow a different strategy and try to reduce the ferroelectricity of the material and make use of transitions induced by electric fields. This method leads to a material which has quite poor performance under small electric field but excels at high fields.

2. Introduction

The following sections are a resume and excerpt from literature, specifically from the books by Hanno Schaumburg[4], Bernard Jaffe, William R. Cook and Hans Jaffe[5] and A. J. Moulson and J. M. Herbert[6].

2.1. Theoretical aspects

The most often used ferroelectric materials all have one similarity, the perovskite structure, shown in Figure 1. This structure has three easily distinguishable atomic positions called A-Site, B-Site and O-Site. The A-Site is 12-fold coordinated and usually occupied by metal ions with a ionic radius > 1 Å. The 6-fold coordinated B-Site is occupied by small ions with a ionic radius < 1 Å. The O-Site is entirely occupied by oxygen, at least in the used oxide based materials.

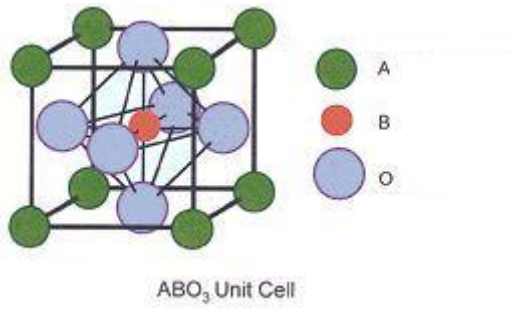


Figure 1: **Schematic drawing of perovskite structure**[7].

Table 1 presents a summary of the ionic radii of the ions used to produce BNT-BKT solid solutions. The values were published by Shannon[8] in 1976 and are often used in literature to calculate the Goldschmidt's tolerance factor[9].

Table 1: **Ionic radii at different coordination numbers for ions used in BNT-BKT. The starred values for Bi^{3+}(XII) and Ti^{4+}(XII) are linear extrapolated from literature values**[8].

c.n.	Bi^{3+}	Na^{+}	K^{+}	Ti^{4+}	O^{2-}
VI	1.03	1.02	1.38	0.605	1.4
XII	1.45*	1.39	1.64	1.07*	
Site occupation	A	A	A	B	O

The starred values for Bi^{3+}(XII) and Ti^{4+}(XII) are calculated from literature data using linear extrapolation. Since the value for Bi^{3+}(XII) is extrapolated, the calculation of the tolerance factor can only be a good estimation.

Equation 1: Calculation of the Goldschmidt tolerance factor.

The ideal perovskite structure is cubic and centrosymmetric and cannot show spontaneous polarization which is the hallmark for ferroelectricity. However, small distortions of the ideal symmetry, introduced by mismatch of the ionic radii required for a Goldschmidt's tolerance factor t of 1 or influences of lone pairs present in Pb^{2+} and Bi^{3+} destroy the centrosymmetric order of the perovskite and lead to an off-centre position of the effective positive and negative charges per unit cell and therefore a polarization. Almost all doping agents influence the symmetry of the unit cell, since there are very few elements with similar ionic radii at given coordination. The influence of the atomic weight of the different elements is also a part of this study and will be part of the following chapters.

A different way to introduce distortion and influence the electrical parameters is the formation of vacancies. Every lattice site of the perovskite (A, B and O) can be the target of vacancy formation. The most common way to describe the stoichiometry of a composition including vacancies is the Kroeger-Vink notation[10]:

M_M ion on its specific site in the lattice

O_O oxygen on its site

Va_M'' vacancy on M-site, charge 2- relative to the metal ion

$Va_O^{\circ\circ}$ vacancy on O-site, charge 2+ relative to the oxygen ion

K_{Bi}'' K^+ on Bi^{3+}-site, relative charge 2-

The nomenclature introduced above allows us to describe and quantify vacancies in materials. Vacancies itself are hardly accessible for measurement, especially absolute quantification. The amount of vacancies can therefore only be deduced from the composition or via weight losses during calcination and sintering. Any formation of secondary phase inclusions or volatilities of components renders estimations of the vacancy concentration futile.

2.2.Piezoelectric and dielectric parameters

Ferroelectric systems are described by a set of characteristic parameters, which can be used to compare different materials. The most relevant parameters are the permittivity ε_r, the dielectric loss factor $tan\ \delta$ and the piezoelectric coefficient d_{ij}. For most actuator applications, the piezoelectric coefficient of interest is d_{33}, where the strain is parallel to the electric field.

One of the key values for a ferroelectric material is the relative permittivity (ε_r). Ferroelectrics are often used as energy storage materials, the relative permittivity is used to describe how much more energy can be stored compared to vacuum with its permittivity ε_0. Since capacitors are often used in microelectronic devices, higher relative permittivities are advantageous because the size of the components can be reduced. The calculation of the capacitance for a single layer capacitor with known dimensions is shown in Equation 2.

Equation 2: **Calculation of the capacitance of a simple capacitor.**

The relative permittivity is related to the polarization and the electric field , as is shown in Equation 3.

Equation 3: **Calculation of the relative permittivity.**

The equation above is especially useful at high field measurement, where the relative permittivity cannot be evaluated directly. In the small signal case, the used impedance analyser HP 4192A can measure the capacitance and loss factor directly from the impedance and the phase angle between voltage and current.

The polarization itself is strongly material dependent, since the formation of electric dipoles using one of the mechanisms shown in Figure 2 is needed. The higher the concentration c of electric dipoles in the material is, the higher the polarization can be.

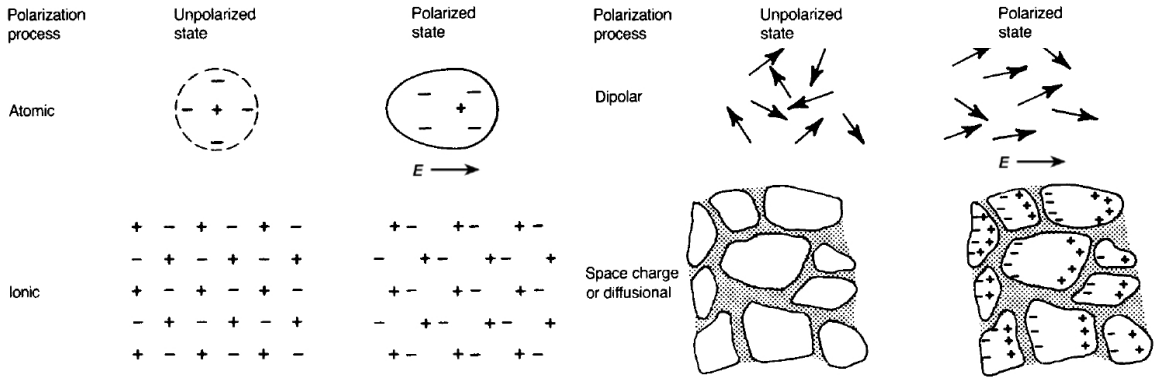


Figure 2: **Polarization mechanisms in dielectric materials**[6].

The emerging dipole moment under the application of an electric field ($q_i\delta$) is also directly proportional to the polarization, as Equation 4 shows.

Equation 4: **Calculation of the polarization.**

The mentioned loss factor describes the amount of electric losses due to conduction and reorientation of the electric dipoles in the applied alternating electric field. In general, those losses are unwanted and should be as small as possible. In addition to the lower energy output of a lossy component, both ohmic and dielectric losses are dissipated as heat and can change the behavior of a temperature dependent material dramatically. The calculation of the loss factor is shown in Equation 5.

Equation 5: **Calculation of the loss factor.**

One of the characteristics of a ferroelectric material is the piezoelectric effect. A ferroelectric material, being always piezoelectric as well, reacts on application of an external force by generating a polarization due to the shift of the charge centre in the deformed unit cell. This effect is called the direct piezoelectric effect and can be used for sensor applications and energy harvesting. Contrary, the material also reacts on the application of an electrical field by deformation. This change in shape is caused by the converse piezoelectric effect and can be used for actuation (Figure 3). Since the deformation occurs almost instantly with the applied electrical field and generates high forces, the production of very small, powerful actuators is possible. The combination of both effects in one component can be used for ultrasonic sensors, transducers or piezoelectric transformers. Ferroelectric materials, which operate at low electric fields have to be poled before usage. The poling

process aligns the polarization vectors (Figure 2, right) in a uniform direction by the application of an electric field at least as high as the coercive field.

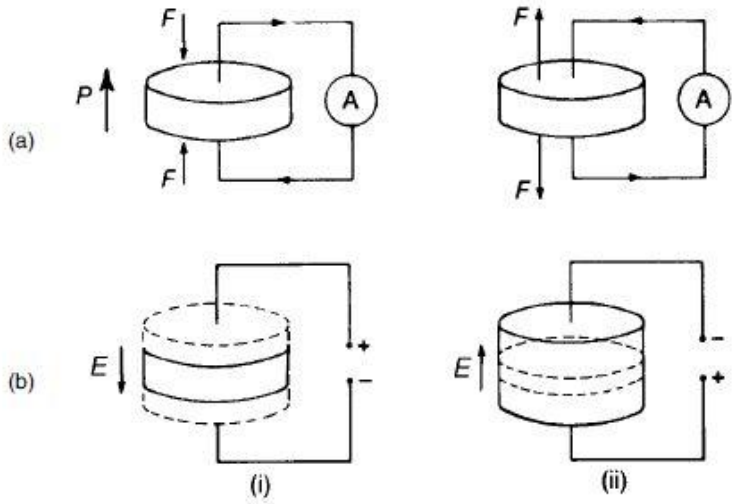


Figure 3: **Schematic illustration of the direct (a) and converse (b) piezoelectric effect.**

The high field values are more useable for high field applications like actuation, but usually require more sophisticated measurement equipment since the applied fields can well exceed 10 kV/mm and therefore high voltages are needed. The key values taken from high field measurements are the maximum and remnant polarization and the coercive field (Figure 4). Those values are also used to classify the material as hard or soft ferroelectric.

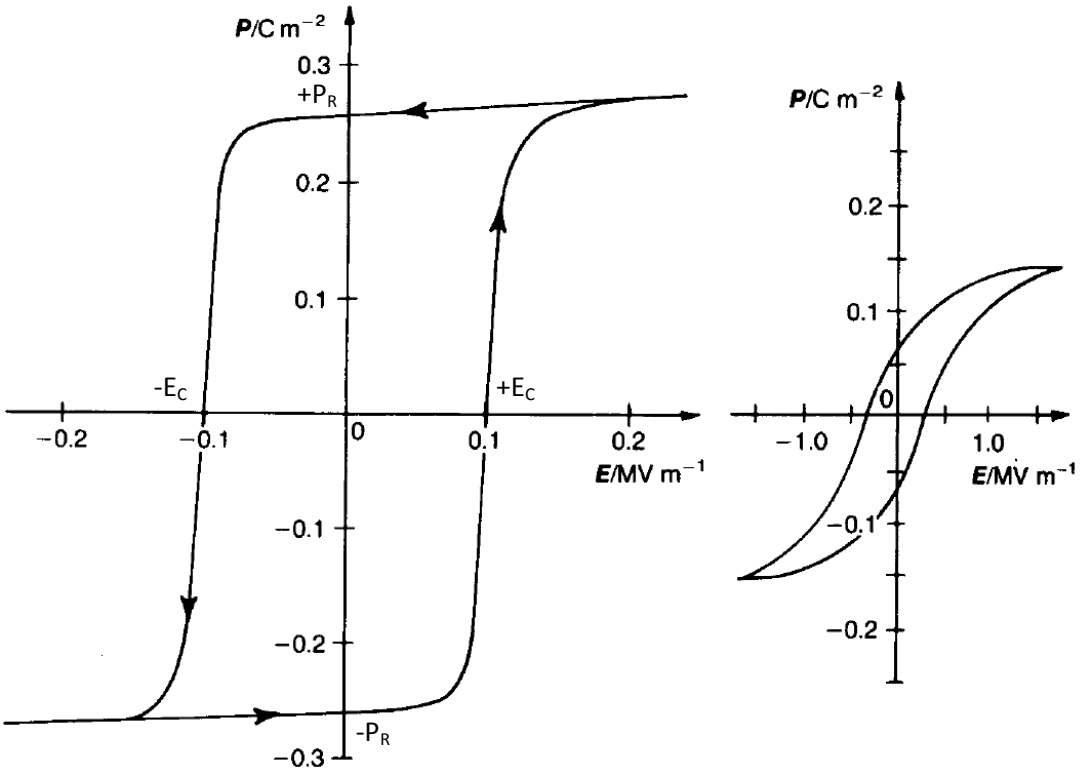


Figure 4: **Comparison of a hard (left) and a soft (right) ferroelectric hysteresis loop**[6].

Figure 4 also shows the position of the before mentioned characteristic parameters E_c, P_R and P_{max} in the hysteresis loop. The absolute value of the characteristic values at positive and negative electric field is essentially equal, since we work with an isotropic polycrystalline, nontextured material (e.g. $|-E_C| = |+E_C|$). The ferroelectric hardness complicates practical uses under high bipolar electric field, since the repolarization is a lossy process which heats up the component.

During the measurement of the electrical hysteresis loop usually the strain loop is measured simultaneously. From this curve a high field piezoelectric coefficient or a field dependant strain can be calculated. Ferroelectric materials usually operate under high fields, due to nonlinearities of the field response, the piezoelectric coefficient and therefore the achievable strain is up to one order of magnitude higher compared to the small signal piezoelectric coefficient.

2.3.Introduction to the lead-free (1-x)BNT-xBKT system

BNT is, next to $BaTiO_3$ (BT) and $(K,Na)NbO_3$ (KNN), one of the most investigated and promising lead-free ferroelectric materials. BNT shows a remnant polarization of 39.2 µC/cm² and a high coercive field of 5.5 kV/mm, shown in Figure 11 in chapter 4.1. Those values classify BNT as a hard ferroelectric material. Literature often states slightly different values for P_R and E_c, but those values are highly depending on the processing of the material[11][12]. The material synthesized in this work shows a higher maximum polarization, coupled with a lower coercive field compared to literature.

Because of its properties, BNT is a very good starting point for further examinations, especially the influence of various doping agents. The manufacturing process for BNT and its doped derivatives is described in detail in chapter 3.1.

Structurally, BNT crystallizes in a complex perovskite structure with mixed A-site occupation. As stated in Table 1, the large ions Bi^{3+} and Na^{+} are located uniformly distributed on the 12-fold coordinated A-site, forming a complex A-site ion M^{2+}. The smaller titanium ion is located on the 6-fold coordinated B-site, forming a corner linked network of $[TiO_6]^{2-}$ octahedrons. Since oxygen is the only anion in BNT, the O-site is entirely occupied by O^{2-}.

The perovskite structure itself is very flexible regarding A-site and B-site ions. The A-site can be occupied by various M^{2+} ions or, like in BNT, a mixture which forms a M^{2+} ion. The B-site is more limited in respect of the ionic radius, but the variations are also numerous. Also, the formation of a complex B-site ion using two ions of different charge and size is possible. These properties lead to a very good miscibility of perovskites and the formation of solid solutions over a wide range.

BNT, as mentioned before, shows excellent ferroelectric parameters and therefore gathered high interest among researchers. BNT can easily be prepared via a solid state method; details are given in section 3.1. The starting materials Bi_2O_3, Na_2CO_3 and TiO_2 are inexpensive, easily accessible and, most important, nontoxic and RoHS compliant. BNT is also quite tolerant regarding stoichiometric mismatch of the composition, which has been shown in literature several times[13][14][15]. This property eases the synthesis of ceramic samples dramatically compared to $NaNbO_3$ (NN) based material which shows a very strong decrease in melting temperature as a reaction on nonstoichiometry both on the sodium and niobium rich side.

BNT sinters readily at 1100 °C, which opens a convenient process temperature window since its melting point is at 1270 °C. BNT unifies very good ferroelectric parameters and easy processing. The only drawbacks are the low melting point of Bi_2O_3 (826 °C) and the solubility of the used carbonates in water. Both of these problems can be avoided with lower calcination temperatures and milling

steps in ethanol. Since the starting powders are already very fine grained, drying is obligatory to remove adsorbed water.

A very common modification of BNT is the formation of a solid solution with BKT. BNT and BKT are miscible in every ratio, forming solid solutions. BKT crystallizes with tetragonal symmetry compared to the rhombohedral BNT. Earlier studies [11][12] described the existence of a morphotropic phase boundary between 18 % and 22 % BKT content in BNT. A phase diagram of (1-x)BNT-xBKT is shown in Figure 5.

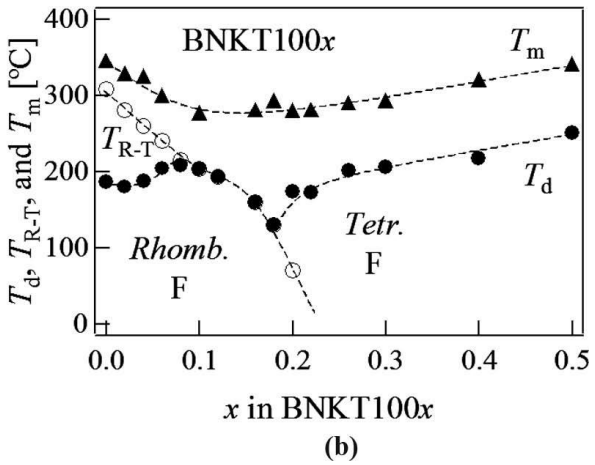


Figure 5: **Phase diagram of (1-x)BNT-xBKT showing the BNT-rich side, including transition temperatures**[11].

The morphotropic phase boundary in the system (1-x)BNT-xBKT is strongly temperature depending and is therefore avoided in this work to ensure temperature invariant material regarding electrical parameters. The temperatures T_d (depolarization temperature) and T_m (temperature of maximum permittivity) will be of further interest later. The area between T_d and T_m is often described as nonpolar or antiferroelectric in literature.

The nonpolar phase has two major advantages compared to the ferroelectric phase at lower temperatures: the permittivity of the material is higher, coupled with lower dielectric losses. Unfortunately, the temperature range of this phase is quite small and it is located well above room temperature. For applications, the existence range of this nonpolar phase has to be widened and lowered to at least room temperature. To influence the material in the desired way, the doping mechanisms described in chapter 2.4 are utilized.

Solid solutions of BNT and BKT usually show better properties than BNT, but with the addition of potassium to BNT problems may occur during the calcination when K_2CO_3 is decarbonized and K_2O is formed. K_2O decomposes at temperatures < 350 °C into oxygen and potassium, leading to potassium

losses due to evaporation. These issues of BNT-25BKT are described in detail in a published article[16].

In this work a mixture of 75 % BNT and 25 % BKT (BNT-25BKT) has been chosen, because it avoids the temperature dependent morphotropic phase boundary. The optimal sintering temperature for BNT-25BKT is slightly higher than for BNT, lying at 1150 °C. The manufacturing process is equivalent to BNT with one exception: since the used potassium carbonate is very hygroscopic, speed during weighing is of the essence.

2.4.Modifications and proposed influences

The properties of a material can be strongly modified with doping agents. Prominent examples for the usage of doping materials to control properties are the semiconductor industry or, more general speaking, formation of alloys in metallurgy. The influences of dopants on the electrical parameters are results of different atomic weight, charge, ionic radius or electronic structure. There is also the possibility of the formation of solid solutions with other materials crystallizing in the perovskite structure. In the latter case, the formation of a morphotropic phase boundary (MPB) is possible, if host and dopant have different symmetries. A MPB composition often shows maximized ferroelectric parameters due to the uncertainty of the structure which allows more degrees of freedom. Unfortunately, the compositional position of the MPB in the phase diagram is often temperature dependent and reduces the operational temperature window for application. The most common doping concepts are presented in the next chapters.

2.4.1. Substitution of single elements

Doping with single elements can be done in two different ways: substitution of an element with the dopant or addition of the doping material in excess. The first method is by far the most common, since the second method always has to deal with uncertainties regarding the site occupation of the dopant in the perovskite structure. Usually, excess doping is used to lower sintering temperatures by creating an intermediate molten phase. There were no attempts made to influence the sintering behavior in this work, the focus is clearly on controlled substitutions and their effects on electrical parameters.

Substitution of single elements with a dopant can also be carried out in various ways. The simplest is to substitute an element with an isovalent ion (e.g. Ti^{4+} / Zr^{4+}). In BNT, 3 metal ions are present: Bi^{3+}, Na^{+} and Ti^{4+}. Since the ionic radius of the substituting ion can only be varied in limited regions, the options of possible dopants are also limited, as Table 2 shows:

Table 2: **Possible substituents for metal ions incorporated in BNT**[8].

Ion	**Radius(XII) [Å]**	**Ion**	**Radius(XII) [Å]**	**Ion**	**Radius(VI) [Å]**
Na^{+}	1.39	**Bi^{3+}**	1.45	**Ti^{4+}**	0.605
Li^{+}	1.25	**Sc^{3+}**	1.12	**Zr^{4+}**	0.72
K^{+}	1.64	**Y^{3+}**	1.25	**Hf^{4+}**	0.71
Cu^{+}	1.23	**Ln^{3+}**	1.22 – 1.36	**Ge^{4+}**	0.53
				Sn^{4+}	0.69

The substitutions given in Table 2 do not introduce vacancies of any kind into the material. Stoichiometrically, a fully occupied perovskite is formed by this method. The influence on the electric parameters is mainly carried out by the differing ionic radii of the elements and / or the different mass. Notable examples are the substitutions of Bi^{3+} with rare earth elements or the substitution of Ti^{4+} with Ge^{4+}, Sn^{4+} or Zr^{4+}[17][18].

Bi^{3+} exhibits a $6s^2$ lone electron pair which can easily be polarized and is assumed to be the reason for the good specific performance of BNT compared with lead-based ceramics (see chapter 4.1). No other element in the periodic table (at least with an appropriate ionic radius) has this electron configuration, so substituting Bi^{3+} always has an influence caused by the differing electronic structure.

The same argument is valid for the substitution of Ti^{4+} with Ge^{4+} or Sn^{4+}. Both Ge^{4+} and Sn^{4+} have a d^{10}-electron configuration which leads to a very high charge density that can influence the electronic parameters of the material.

Another way of single element doping is the substitution of an element with a heterovalent ion. In this case, vacancies are created in the lattice that also influence the electrical behavior. Doping ions with a higher valence state are called donors; substituents with a lower valence state are called acceptors. Acceptor dopants usually generate oxygen vacancies to maintain charge neutrality, which can get conductive at elevated temperatures. For this reason, acceptor doping has not been studied in this work. Also, in PZT based materials donor doping usually leads to a softened hysteresis loop, which is favorable for most applications. Table 3 shows possible donor dopants for BNT.

Table 3: Possible donor dopants in BNT[8].

Ion	Radius(XII) [Å]	Ion	Radius(XII) [Å]	Ion	Radius(VI) [Å]
Na^{+}	1.39	Bi^{3+}	1.45	Ti^{4+}	0.605
Mg^{2+}	1.20	Ce^{4+}	1.14	V^{5+}	0.54
Ca^{2+}	1.34	Te^{4+}	1.90	Nb^{5+}	0.64
Sr^{2+}	1.44			Ta^{5+}	0.64
Ba^{2+}	1.61			Mo^{6+}	0.59
Bi^{3+}	1.45			W^{6+}	0.6

While Na^{+} can be substituted with all earth alkaline ions, the options are very limited for Bi^{3+}. The formulation of the stoichiometry including the vacancies using the Kroeger-Vink notation will be part of the subsequent chapters.

2.4.2. Solid solutions of perovskites and non-perovskite materials

BNT is often combined with other ferroelectric perovskites to enhance its electrical parameters. Notable examples are solid solutions like $Bi_{0.5}Na_{0.5}TiO_3$-$BaTiO_3$ (BNT-BT)[19], $Bi_{0.5}Na_{0.5}TiO_3$-$BaTiO_3$-$(Na,K)NbO_3$ (BNT-BT-KNN)[20], $Bi_{0.5}Na_{0.5}TiO_3$-$Bi_{0.5}K_{0.5}TiO_3$ (BNT-BKT) [12]. All of those mentioned examples combine BNT with another ferroelectric material, mostly using the effects of the morphotropic phase boundary because of the different symmetry of the added compound. Doping with non-ferroelectric perovskites is rarely found in literature but offers a way to move the temperature levels for T_D and T_m in the desired direction. Examples for doping with non-ferroelectric perovskites are BNT-ST ($Bi_{0.5}Na_{0.5}TiO_3$-$SrTiO_3$)[21] or BNT-KT ($Bi_{0.5}Na_{0.5}TiO_3$-$KTaO_3$)[22].

2.5.Donor doping and single element substitutions

As mentioned in chapter 2.4.1, there are many ways to substitute ions in BNT with other elements. To clarify the influence of different doping agents, different samples were prepared.

The influence of A-site donor doping has been clarified using Ca^{2+} replacing Na^{+} and Ce^{4+} replacing Bi^{3+}, creating vacancies on the A-site of the perovskite. This doping concept can also be found in lead lanthanum zirconate titanate (PLZT), a commonly used antiferroelectric material with the following composition:

Equation 6: Composition of PLZT, donor doped with lanthanum.

In literature[23], values for *x* up to 0.3 are reported without the formation of secondary phase inclusions or decomposition reactions. A lanthanum content of 0.3 creates 0.15 A-site vacancies, meaning that 15 % of the A-site positions are unoccupied. According to this publication[23], lanthanum stabilizes the anti-ferroelectric phase at cost of the ferroelectric phase, possibly a result of the introduced vacancies. Since the A-site of BNT is occupied by bismuth and sodium, the influences of donor doping for each A-site element are studied.

Ti-substitutions were carried out using Ge^{4+}, Sn^{4+} and Zr^{4+}. All those substitutions are isovalent and do not create any vacancies. As a donor dopant on the B-site of the lattice, Nb^{5+} was used. The influence of mixed B-site occupation was investigated using mixtures of Li^{+} / V^{5+} and Li^{+} / W^{6+} as substitution for Ti^{4+}. By adjusting the ratio of Li^{+} / V^{5+} and Li^{+} / W^{6+}, theoretically vacancy free compositions were prepared.

2.5.1. A-site donor doping with Ca

As previously mentioned, PLZT is a donor doped lead based material, which has an antiferroelectric characteristic. To achieve a similar composition in BNT, one of the possibilities is to replace Na^{+} with Ca^{2+}. Ca^{2+} has been chosen mainly because of its ionic radius which is almost equal to the radius of Na^{+} in 12-fold coordination. The Kroeger-Vink notation of Ca^{2+} doped compositions is shown:

Equation 7: Composition of Ca-doped samples.

To maintain charge neutrality, two Na^{+} are replaced by 1 Ca^{2+}, creating one vacancy.

2.5.2. A-site donor doping with Ce

The motivation in this case is the same as before, with the difference that the only possible ion M^{4+} to replace Bi^{3+} is Ce^{4+}. Other ions like Te^{4+} are too big; every other M^{4+} ion is too small to fit on the A-site of the perovskite. The composition of the Ce-doped samples is shown in Equation 8:

Equation 8: Composition of Ce-doped samples.

The samples were again prepared electronically neutral, meaning that every introduced ion of Ce^{4+} replaces – Bi^{3+} to maintain charge neutrality. This method also leads to the creation of – vacancy per replaced Bi^{3+}.

2.5.3. B-site donor doping with Nb

Donor doping can also be done on the B-site of the perovskite, replacing Ti^{4+} with M^{5+} or M^{6+}. Again, the ionic radius of the ion replacing Ti^{4+} should roughly match. This experiment was carried out using Nb^{5+} as a replacement, creating vacancies on the B-site of the perovskite.

Equation 9: Composition of Nb-doped samples.

The substitution of Ti^{4+} with Nb^{5+} is carried out with respect to maintain electronic neutrality. The addition of x Nb^{5} then creates x/4 vacancies, which can influence the electrical behavior of the material.

2.5.4. Ti-substitution with Ge

Another isovalent doping agent is Ge^{4+}. Germanium, being a main group element, has a fully occupied d-shell and a d^{10} electron configuration as Ge^{4+}. The ionic radius is slightly smaller than Ti^{4+}, leading to a high charge density.

Equation 10: Composition of Ge-doped samples.

Ge^{4+} is isovalent to Ti^{4+}, so no vacancies are formed. The smaller ionic radius influences the structure of BNT; the high electron density can influence the temperature behavior of BNT by weakening Bi-O interactions.

2.5.5. Ti-substitution with Sn

Sn^{4+} has, like Ge^{4+}, a d^{10} electron configuration. The effects should therefore be comparable. The ionic radius of Sn^{4+} is about 20 % larger than the radius of Ti^{4+} so limited solubility can be expected.

Equation 11: Composition of Sn-doped samples.

Again, the substitution of Ti^{4+} with Sn^{4+} has no influence on the vacancy concentration. The high electron density influences the ferroelectricity of BNT as well as the structure. The comparison of the influences of Zr^{4+} / Ge^{4+} / Sn^{4+} leads to an understanding, how radius and d^{10} configuration influences the behavior of the material.

2.5.6. Ti-substitution with Zr

The most obvious substituent for Ti^{4+} is Zr^{4+}. Titanium and zirconium are chemically very alike, with Zr^{4+} being the larger ion. The solubility of Zr^{4+} in BNT is limited, pure BNZ ($Bi_{0.5}Na_{0.5}ZrO_3$) has not been synthesized yet. The substitution of Ti^{4+} with Zr^{4+} does not create vacancies since it is an isovalent substitution.

Equation 12: Composition of Zr-doped samples.

The main influence of this doping variant is the different size of Ti^{4+} and Zr^{4+} which can influence the symmetry. Also Zr^{4+} has a higher mass and a possible influence on the frequency dependent behavior.

The radius of Zr^{4+}(VI) is with 0.72 Å very close to the radius of Sn^{4+}(IV). The comparison of tin- and zirconium-doped samples can therefore be used to compare the influence of radius, mass and electron configuration on the electrical parameters and temperature dependence.

The influence of zirconium doping on the properties of BNT has rarely been studied, literature states reduced sintering activity, lower permittivity and larger grain size with rising zirconium content[24][25][26].

2.5.7. Ti-substitution with Li / V

Another way to introduce a B-site ion in BNT is the formation of a complex ion. In BNT this is already the case on the A-site, being a complex ion M^{2+} consisting of 0.5 Bi^{3+} and 0.5 Na^{+}. In lead-based materials, lead magnesium niobate (PMN) with a formula of $PbMg_{1/3}Nb_{2/3}O_3$ is a popular representative of complex B-site doping. Applying this scheme for a B-site ion, one of the possibilities is the combination of Li^{+} and V^{5+} to a complex ion M^{4+}.

To avoid the formation of vacancies, two constraints are made:

-
-

These two conditions ensure, that a single ion Ti^{4+} is replaced by a complex ion, consisting of 0.25 Li^{+} and 0.75 V^{5+}. For the average ionic radius of this complex ion (LV^{4+}) the weighted average of the radii of Li^{+}(VI) and V^{5+}(VI) is considered,

resulting in a value of 0.595 Å, which is about 1.7 % smaller than r(Ti^{4+}(VI)). The ion LV^{4+} should therefore fit nicely into the structure, despite the big Li^{+}(VI) ion, which has a radius of 0.76 Å. Since the combination of Li^{+} and V^{5+} also forms a compensated acceptor / donor couple, the effects of this kind of doping are very interesting.

2.5.8. Ti-substitution with Li / W

Equivalent to the scheme presented in chapter 2.5.7, samples with a complex ion consisting of Li^{+} and W^{6+} were prepared with constraints similar to the substitution with Li / V:

-
-

Due to the high valence state of W^{6+} compared to V^{5+}, the coefficients change. The complex ion LW^{4+} is now formed by 0.4 Li^{+} and 0.6 W^{6+}. The weighted average of the ionic radii r(LW^{4+})(VI) is now at 0.664 Å, which is about 10 % bigger than Ti^{4+}(VI). Like in BNT-xLV before, the size of the complex ion should ensure the fit in the structure, even with the big W^{6+}(VI) ion. The combination of Li^{+} and W^{6+} again forms a compensated acceptor / donor couple with the possibility of a high impact on electrical parameters.

2.6.Solid solutions with other perovskites and non-perovskites

In the following chapters, a short overview of the used doping materials is given. The reason why the specific elemental combinations were chosen is also given in this section. In literature several studies suggest an influence of the ionic radius of a doping element on T_D and T_m[27][28]. Since a main goal of this study is to narrow the area of the hysteresis loop, a composition with a lower T_D (approximately 160 °C for undoped BNT) and a higher or equal T_m is desired. Between those temperatures, the material shows a nonpolar or antiferroelectric behavior, which matches the needs for application.

2.6.1. BNT-CT

$CaTiO_3$ (CT) is the naming compound for the perovskite structure found in many ferroelectric materials. CT itself shows no ferroelectric hallmarks at room temperature, but its structure suggests high miscibility in solid solutions with BNT. Previous works, especially the studies from Takenaka [27][28] show a positive influence of Ca^{2+} in BNT. The addition of CT lowers T_D and raises T_m, which is unique among the investigated earth alkaline metals.

2.6.2. BNT-CG

The addition of $CaGeO_3$ (CG) is similar to the addition of CS before. Ge^{4+} also has a d^{10}-electron configuration which raises the electron density on the B-site. Ge^{4+} has a smaller ionic radius than Ti^{4+}, so the influence of the radius can also be deduced by comparing CT, CS and CG samples.

2.6.3. BNT-CS

The motivation of adding $CaSnO_3$ to BNT is partially the same as with CT. Ca^{2+} has a favorable influence on thermal behavior; the addition of Sn^{4+} raises the electron density due to d^{10}-electron configuration on the B-site of the perovskite. Ti^{4+} and Sn^{4+} slightly differ in regards of the ionic radius (see Table 2) so the formation of solid solutions with BNT is very likely. The samples with this composition can be used to confirm whether the effects of Sn-doping and doping with CT add up.

2.6.4. BNT-CZ

$CaZrO_3$ (CZ) is probably the nearest relative to CT, regarding its composition. Ti^{4+} and Zr^{4+} are chemically very much alike and usually accompany each other in minerals. Like CT, CZ crystallizes in a perovskite structure, suggesting high miscibility with BNT. The influence of the compared to Ti^{4+}(VI) bigger Zr^{4+}(VI) on the electrical and thermal parameters will be of interest.

2.6.5. BNT-MT

The introduction of $MgTiO_3$ (MT) into BNT could lead to an even stronger shift of the temperature levels than the one observed using CT as a doping agent. The magnesium-based compound MT does not crystallize in the perovskite structure, so limited solubility can be expected. Also, Mg^{2+} can occupy the B-site, due to its small ionic radius. The latter point would lead to acceptor doping on the B-site, which is encountered by the formation of oxygen vacancies. Oxygen vacancies can get conductive at higher temperatures, with conductivity being the least wanted property for a ferroelectric material.

2.6.6. BNT-MG

The effect of Magnesium, being much smaller than calcium has not been investigated so far. $MgGeO_3$ (MG) also introduces the d^{10} ion Ge^{4+} into BNT. Both ions Mg^{2+} and Ge^{4+} are small compared to the ions they should substitute. Also, MG does not form a perovskite structure, solubility problems can again be anticipated. This composition can be used to clarify the influence of radius and electron configuration of MT, MS and MG addition.

2.6.7. BNT-MS

$MgSnO_3$ (MS) introduces a high electron density on the B-site due to the d^{10} ion Sn^{4+}. Mg^{2+} should influence the temperature levels of T_D and T_m in a positive way. Unfortunately, MS does not crystallize in a perovskite structure, so miscibility problems can be expected. The small size of Mg^{2+} can lead to the same problems described in 2.6.5.

2.6.8. BNT-MZ

$MgZrO_3$ (MZ) combines the small Mg^{2+} and the large Zr^{4+} ion. MZ does not form a perovskite structure, so limited solubility in BNT can be expected. The influences on T_d and T_m should be similar to the samples doped with MS, the comparison of MS and MZ can be helpful to describe the influence of electron configuration (Sn^{4+} as d^{10} ion) and radius ($r(Sn^{4+})$ similar $r(Zr^{4+})$).

3. Experimental section

This chapter introduces the used methods of preparation and examination of the samples. The preparation method of choice is, due to its simplicity, the mixed oxide route. The examination methods are common techniques for the characterization of solids and are presented in a compact way.

3.1.Sample preparation

The preparation of the samples was carried out using a common mixed oxide route. This preparation method is very easy to do in the lab, compared to other techniques like sol-gel processing or organometallic routes. The main advantage of the mixed oxide route lies in the use of simple metal oxides or carbonates, which are easier to handle and much cheaper than precursors for the above mentioned solution based routes.

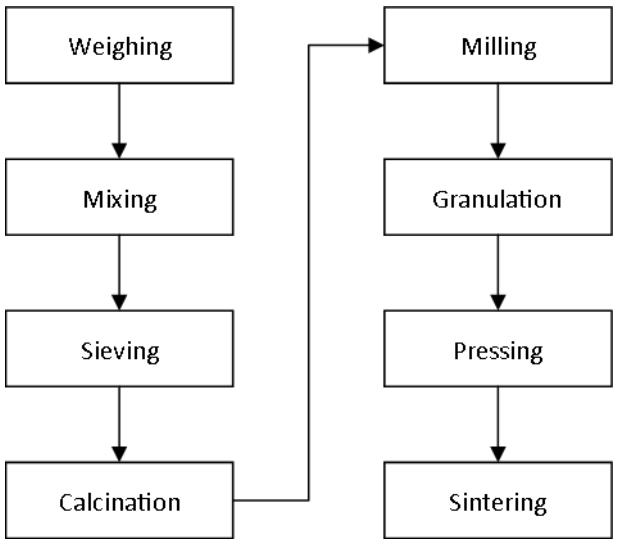


Figure 6: **Workflow mixed oxide route.**

The disadvantage of the mixed oxide method is its vulnerability to stoichiometric deviations. These deviations can either be introduced by relative humidity of the air in the lab which highly affects hygroscopic carbonates such as K_2CO_3 or simply by weighing errors due to small amounts of doping material. Overall, the easiness of the mixed oxide route is the crucial point; the disadvantages mentioned can be overcome by careful drying of the starting materials and very careful work. Weighing is therefore a very sensitive part of preparation which has a high influence on stoichiometry and hence defect chemistry in the material.

The following mixing process is used to get a homogeneous mixture of the different oxides and carbonate starting materials. Since water soluble chemicals are used, this step is carried out in ethanol. As mixing medium, milling balls and bowls made of tungsten carbide were used, mainly

because of the hardness of the material. Milling media fabricated of yttrium or magnesium stabilized zirconia turned out to be prone to abrasion, which influences the stoichiometry of the material, since zirconium can replace titanium in a wide range. The milling parameters depend on the used mill and batch size.

Table 4: Milling parameters.

Batch size	Used mill	Milling bowl	Ball diameter	Milling speed	Milling time
15 g	Fritsch Pulverisette 7	45 ml	5 mm	300 U/min	30 min
100 g	Fritsch Pulverisette 6	250 ml	10 mm	450 U/min	30 min

The resulting ethanol / oxide / carbonate suspension was then dried in a forced air flow drying oven at 120 °C, the ethanol was thereby evaporated. Compared to other drying methods like using a rotary evaporator, the ethanol cannot be recycled using the drying oven. On the other hand, the yield of homogeneous material is much higher because there is no irretrievable residue compared to using round bottom flasks on the rotary evaporator. The subsequent sieving step was used to reduce the agglomerate size below 500 µm before the calcination.

The calcination reaction is a very crucial point in the fabrication of a ferroelectric material. In this step, the homogenized starting materials react with each other and form the final compound with perovskite structure. In this work, the calcination was carried out at 800 °C, which is relatively low, compared to literature data. The heating and cooling rates were set to 10 K/min, the cooling rate could not be achieved due to passive cooling.

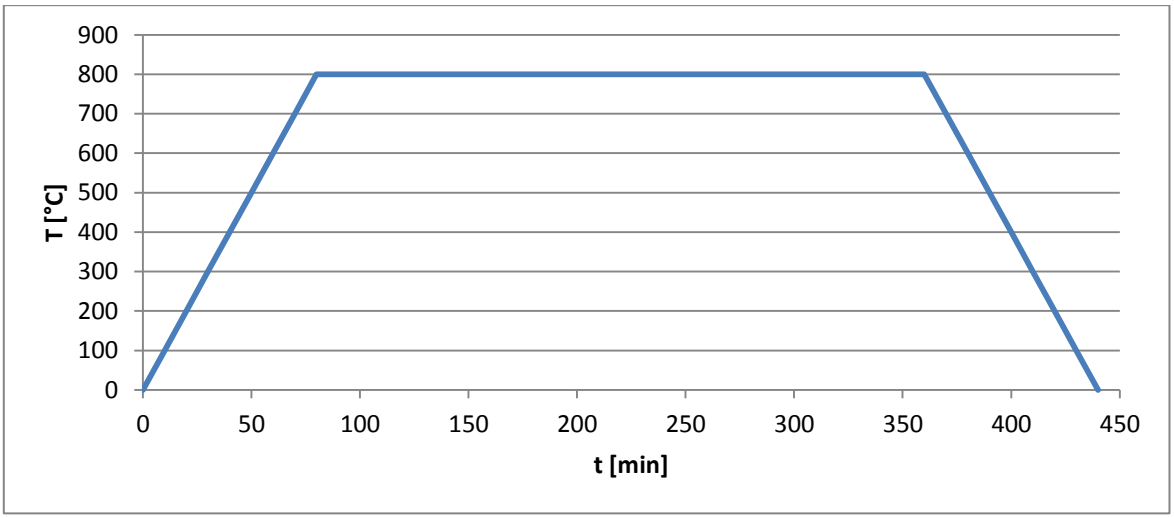


Figure 7 Temperature characteristic for the calcination process.

The temperature was set at moderate 800 °C to avoid melting of Bi_2O_3 (T_M = 826 °C) and, at high doping levels, possibly existing eutectic compositions between the starting materials. In earlier experiments, XRD-analysis of calcined powder showed no presence of unreacted starting material, so 800 °C and the relatively long time of 5 h are sufficient for a complete calcination reaction with the used batch size (15 – 100 g).

The following milling step was done similar to the mixing step. The same milling parameters were used; the dispersion liquid was again ethanol. Although there are no water-soluble compounds left in the calcined material, ethanol was chosen for speed reasons. Evaporation of ethanol is far more readily done than drying the same amount of suspension based on water. This milling step was used to reduce the particle size before granulation to a d_{50} of less than 1 µm. The particle size achieved ensures good sinterability and handling. Smaller particle sizes require longer milling times or multi-step milling with reducing milling ball diameter.

In order to get the calcined powder into disc shaped samples, a forming step is needed. Since fine powders can hardly be pressed into dense samples, poly ethylene glycol with an average molar mass of 20000 g/mol (PEG20000) was added to reduce friction between the particles. In this work, an addition of 5 % w/w of PEG20000 as binding agent was chosen. An aqueous binder solution and calcined powder were mixed in the desired ratio of approximately 5 % w/w PEG20000 and 100 % w/w powder and dried in a drying oven at 80 °C for at least 20 min. The material was then sieved to a agglomerate size less than 180 µm before pressing.

As sample geometry, discs with 13 mm green body diameter were chosen. The discs were pressed using standard tools for the manufacture of KBr-samples for IR-spectroscopy. In order to get green bodies with sufficient green body density, a maximum pressure of 150 MPa was applied. The duration of pressing was set to 5 min which showed good results in earlier experiments. The pressed samples show a relatively high mechanical stability, if pressed without faults.

The final processing step was sintering of the green bodies prepared before. The aim of a successful sintering process is to achieve dense samples without decomposition of the material or evaporation of components. Also, sintering is usually a solid state process; molten phases should be avoided unless they are intended. The temperature profile is shown below; the maximum temperature was set to 1100 °C.

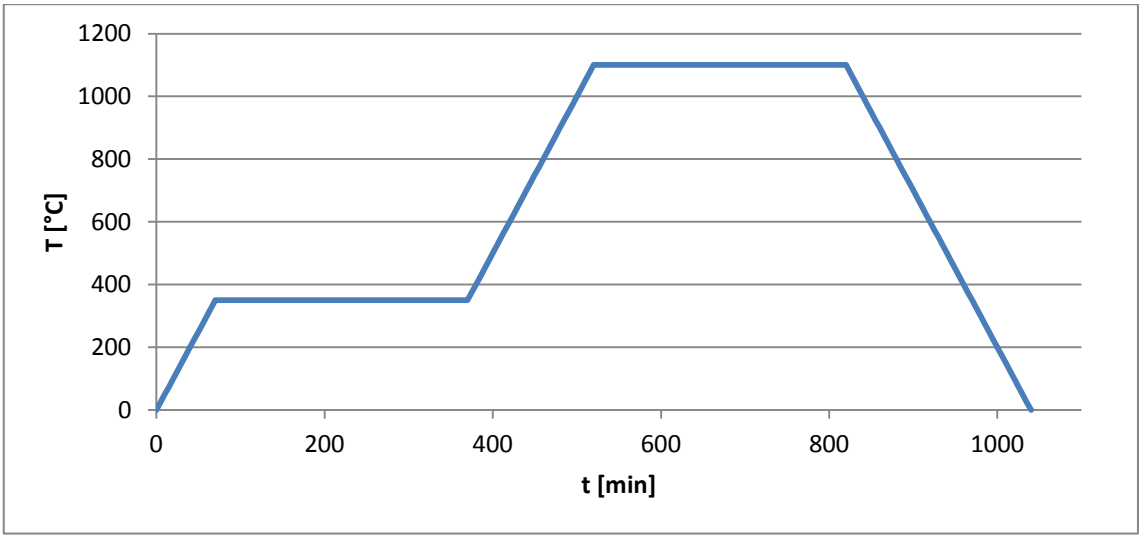


Figure 8: **Temperature characteristic for the sintering step.**

The sintering profile shows two distinctive areas, one at a temperature of 350 °C, the other at 1100 °C. The lower area is needed to decompose the binding agent PEG20000. In this section, no densification of the samples occurs; PEG20000 is pyrolized to H_2O and CO_2. To ensure open channels for the gaseous reaction products, this step has a long holding duration in which all decomposition products can evaporate. In the second area at 1100 °C the densification of the samples takes place. The sintering temperature of 1100 °C is valid for all samples in this work.

3.2.Sample characterization

In this chapter, basic evaluation methods for ferroelectric ceramic samples are presented. The used methods are standard techniques for solid state analysis and ferroelectric evaluation, so this should serve as an overview of the performed measurements.

3.2.1. X-Ray diffraction

X-Ray diffraction (XRD) experiments were carried out in this work to determine the lattice parameters and theoretical density of the sintered material. Since the produced ceramic discs are polycrystalline, powder diffraction patterns were obtained. The sintered samples were ground up using a corundum mortar and pestle to a particle size of approximately 100 µm before measurement. The measurement equipment was a BRUKER D8 Advance using a Cu K_α radiation source, the data was processed using Panalytics X'Pert Highscore Plus with default settings. For all basic compositions, crystal information file No. 154040[29] was used. Compositions containing potassium were refined using crystal information file No. 98046[30]. In this work, XRD was mainly used to check the samples for secondary phase inclusions and to determine the cell volume. Changes of the cell volume gives an indication, if doping elements are incorporated in the material because of differing ionic radii compared to the substituted element. The ratio of the theoretical density and the density derived by the Archimedes' method (Mettler Toledo XS204 DeltaRange) is called the relative density, which is an indicating value for the porosity of the material. For high field measurements, a relative density > 95 % is favoured.

3.2.2. Scanning electron microscopy / Energy dispersive X-Ray spectroscopy

The evaluation of the microstructure was carried out using scanning electron microscopy (SEM). The used electron microscope (Zeiss Ultra 55) also features a detector for energy dispersive X-Ray spectroscopy (EDX), which was used for elemental analysis. The samples were prepared with a polishing process using silica gel to ensure a smooth surface for channelling contrast measurements. The conductive layer on the samples consisted of carbon. Pictures were taken with secondary electron and backscattered electron detection for better distinguishing between pores and inclusions. Also, channelling contrast pictures were taken to show domains and single grains of the material. The EDX spectra were processed using standard routines.

The channelling contrast images were used to determine the average grain size of the prepared samples. This evaluation was carried out on the basis of DIN EN ISO 643:2003[31] using the line intersection method (Linienschnittmethode). Because of the high used magnification, the recommended minimum intersection points of 50 could be not achieved in all samples; the grain size can therefore only be counted as estimation.

3.2.3. Small signal electrical measurement

Small signal electrical measurements are the first electrical characterisations of new produced samples. Prior to this, the geometry (diameter, thickness) of the samples has to be measured with a sliding calliper (Mitutoyo CD-15DCX). The small signal values include permittivity and dielectric loss, usually measured at room temperature with a Hewlett-Packard HP4192A Impedance Analyzer at a frequency of 1 kHz and amplitude of 1 V sine. These values give basic information about the sample and its electrical behavior. After a poling process with field in the kV/mm-range, the samples get measured again. In the case of strong ferroelectric and therefore mostly high temperature sensitive samples, the values for permittivity and dielectric loss change. After poling, the piezoelectric coefficient can be measured using mechanical actuation to further evaluate the ferroelectricity of the sample.

Temperature dependent small signal values can give information about transition points like the depolarization temperature (T_D) or the transition between distorted and cubic perovskite (T_m). Such measurements were done on a Novocontrol Quatro Cryosystem coupled with a Novocontrol Beta Single Unit Analyzer. To evaluate the material closer, simultaneously to the temperature dependence the frequency dependence is checked over a large frequency range. The frequency behavior delivers valuable data, if the material has relaxor properties.

3.2.4. Hysteresis loops

The measurement of hysteretic loops is a very powerful tool in the field of ferroelectric materials. The high applicable field is used to measure the maximum polarization of a material. Also, other ferroelectric properties like remnant polarization and coercive field are easily accessible.

Ferroelectric materials are often used as actuators; the electric field needed for high strain values usually is in the kV/mm-range. The used aixACCT-aixPES Piezoelectric Evaluation System features, next to polarization measurement under high fields, an interferometer for strain measurement. This combination can be utilized to perform measurements close to practice conditions on disc shaped samples, which are easy to prepare. All measurement methods can also be performed at varying temperature and with bi- or unipolar actuation.

4. Results

The following chapters describe the results of the used doping methods on their influence on the material properties. Each chapter closes with a short evaluation of the usability of a certain doping method concerning its electrical parameters. The compositions with isovalent substitutions of titanium, BNT-xCT and BNT-xMT can be considered as key compositions which ease the interpretation of the behavior of materials like BNT-xCG, which can also be described as germanium substituted BNT doped with CT. To keep the prosaic parts more easily to read, the used elements are often referred to in their metallic name. In the material, those elements are of course incorporated as ions.

4.1. The starting point: BNT

The ferroelectric material BNT, synthesized with the parameters and methods described in chapter 3.1, crystallized in a rhombohedral structure with a cell volume of 352.8229 Å³ per unit cell. This value serves as a point of reference for the following doping experiments, since the size of the unit cell is related to the size of the incorporated ions. Replacing a small ion with a larger one results in a bigger cell volume, confirming the successful fit on the right lattice site. The XRD-pattern, displayed in Figure 9, shows no secondary phase in the material.

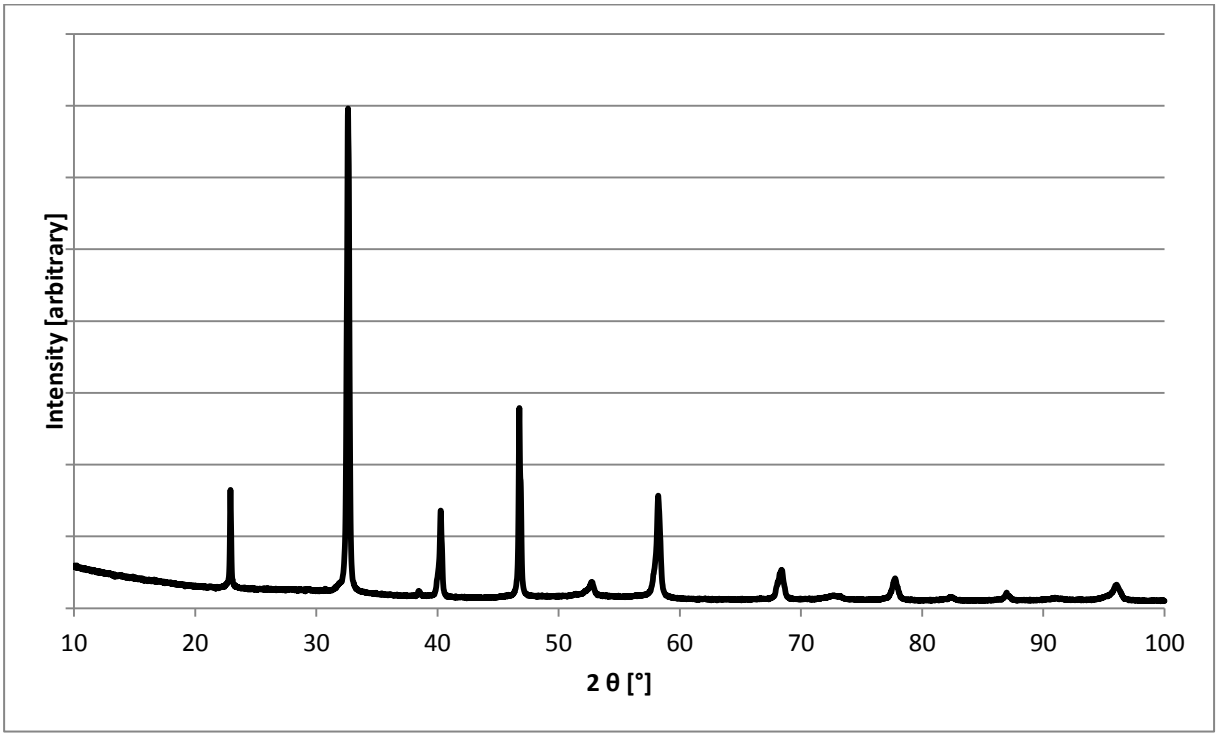


Figure 9: XRD pattern of BNT.

BNT without secondary phase inclusions is quite hard to synthesize, because of the volatility of Bi_2O_3 and, to a lower extent, Na_2O. The use of a calcination temperature of 800 °C helps avoiding these losses due to evaporation, since it is well below the melting temperature of the mentioned Bi_2O_3 and Na_2O. The completeness of the calcination has also been checked using XRD; the reaction is complete after 5 h, leaving no detectable residue of the starting materials.

The SEM image (Figure 10) shows a nicely formed ceramic microstructure with relative densities above 95 %. Secondary phase inclusions were not detected; the material can therefore be considered single phase.

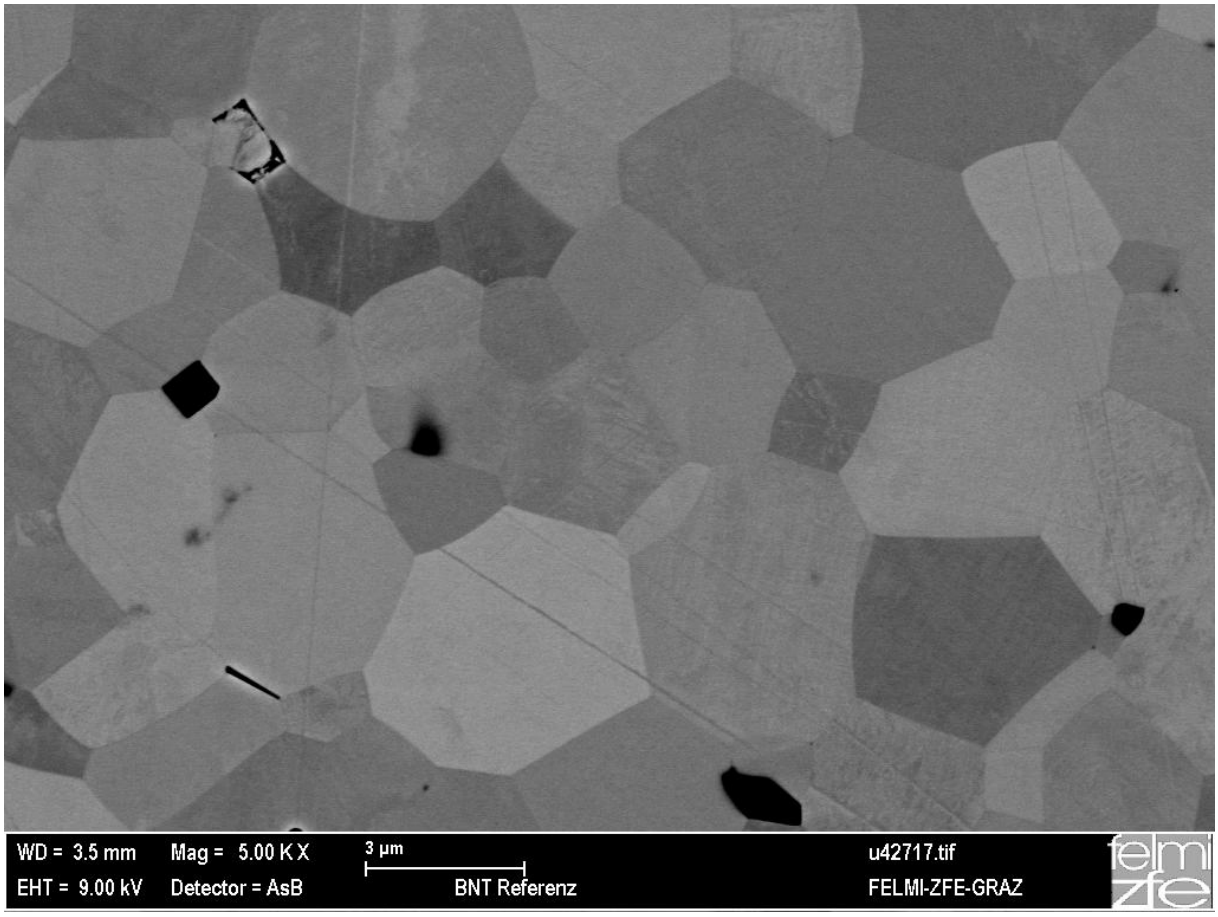


Figure 10: **Channeling contrast SEM image of BNT.**

The grain size of BNT was determined using the line intersection method described in DIN EN ISO 643:2003[31]. The grain size will be further used to describe differences between the synthesized materials and the influence of the different doping agents. The cell volume of BNT was derived using the XRD-pattern.

Table 5: Average grain size and cell volume of BNT.

	BNT
Grain size [µm]	2.0
Cell volume [Å³]	351.8229
Theoretical density [g/cm³]	6.00
Archimedes density [g/cm³]	5.90
Relative density [%]	98

The far more important result is the ferroelectric polarization loop, being measured at high electric fields well above E_C, shown in Figure 11. The hysteresis is typical for a hard ferroelectric material. The strain has a very high remnant part which leads to mechanical destruction of the ceramic and high losses if bipolar driven. Generally spoken, high remnant polarization leads to high remnant strain and little usability of the material for actuation devices.

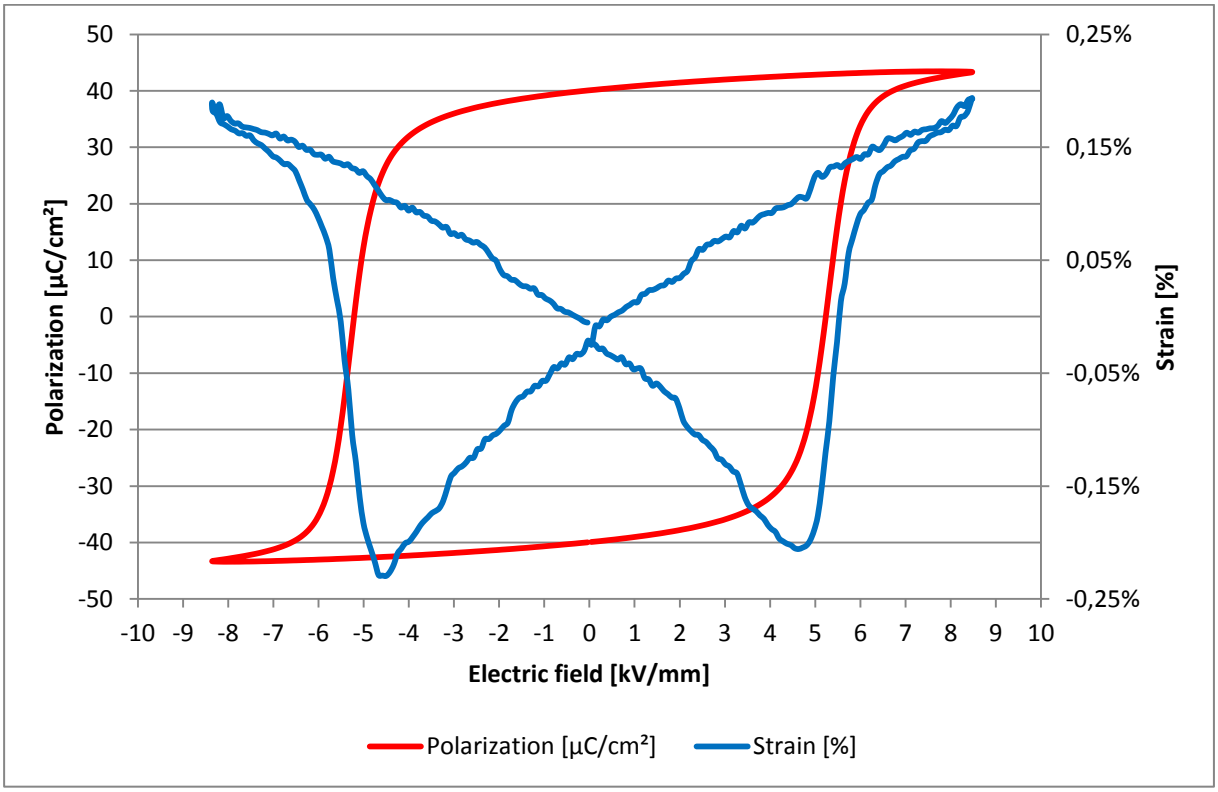


Figure 11: Hysteresis loop of BNT.

The ferroelectric properties of BNT are excellent. The maximum polarization P_{max} lies at 42.3 µC/cm², the remnant polarization has a very high value of 39.4 µC/cm² or 93 % of P_{max}. The coercive field E_c is with 5.5 kV/mm also very high. Hard PZT, as a comparable material shows a maximum polarization of

37 µC/cm² and a remnant polarization of 26 µC/cm² or 70 % of P_{max}. The coercive field is with 1.1 kV/cm very low compared to BNT[32].

The temperature dependence of ferroelectric materials is always a point of interest, since capacitors or actuators should show constant properties over a certain temperature range. BNT has, according to the phase diagram shown in Figure 5 in chapter 2.3, only one transition temperature in our measuring range between -50 and 250 °C. The depolarization temperature T_d is located at 177 °C[11], marking the transition between ferroelectric and antiferroelectric / nonpolar characteristics. The transition T_{R-T}, the temperature of symmetry change from rhombohedral to tetragonal is located at temperatures > 300 °C[11] and therefore not covered in this measurement. T_m, being the temperature of the maximum permittivity is located at approximately 340 °C[11] and also out of reach. The properties of BNT synthesized for this work are shown in Figure 12. The temperature levels may differ because of differing synthesis methods.

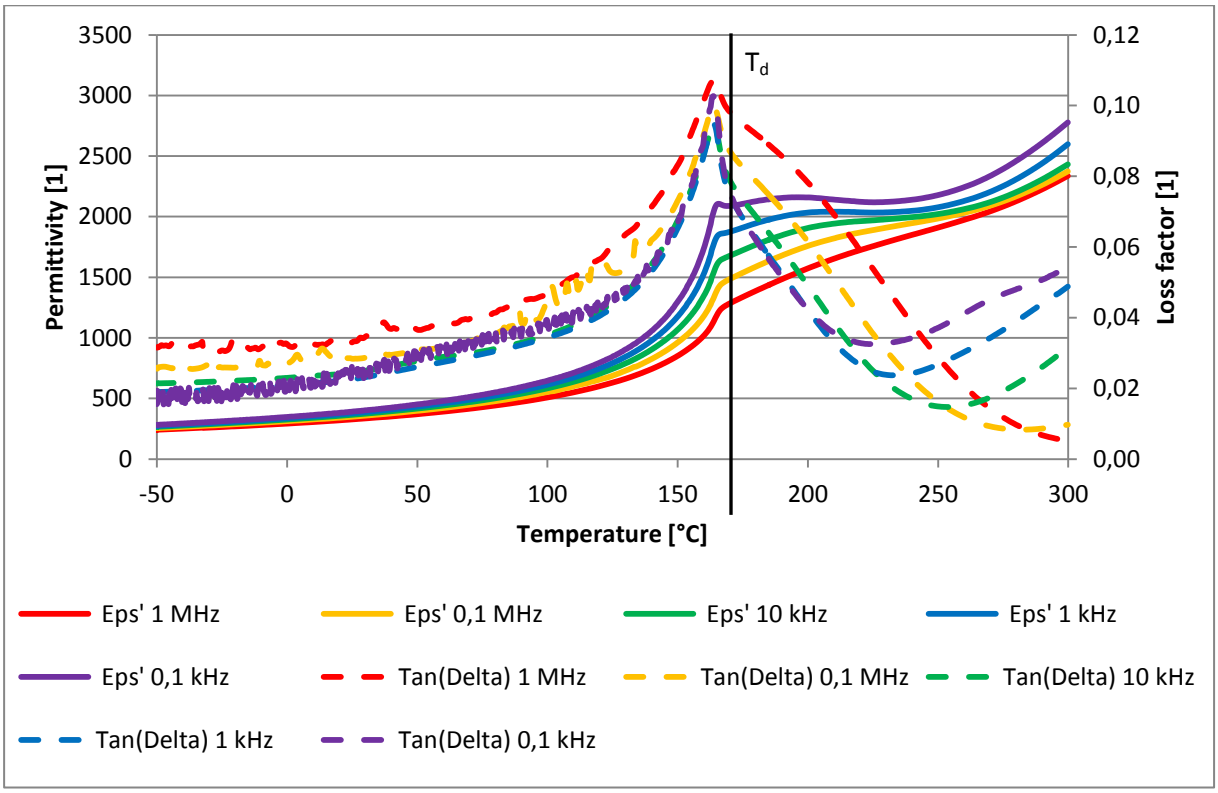


Figure 12: Temperature dependence of permittivity and loss tangent in BNT.

The temperature dependence of the permittivity and the loss factor is very high. The material also shows a distinctive maximum of the loss factor at 161 °C, being the temperature of depolarization T_d. As mentioned before, T_m is not visible due to the low maximum measurement temperatur, but this transition influences this measurement at higher temperatures. Compared to T_d, T_m is highly

frequency dependant, already visible at these low temperatures. Between T_d and T_m is a region with very high values for the permittivity and low losses, which is of certain interest.

4.2. BNT-25BKT

BNT-25BKT is a solid solution, consisting of 75 %mol BNT and 25 %mol BKT. This composition yields excellent properties, as previous works of our group[16] show. The hysteresis loop exhibits considerable pinching at room temperature, meaning that it is constricted at low electric fields (Figure 15 in chapter 4.2). The maximum polarization is slightly lower compared to BNT, as is the remnant polarization.

The work with potassium containing materials requires more attention, since K_2CO_3 is extremely hygroscopic. There is also the possibility of potassium losses during the calcination reaction, because K_2CO_3 reacts to K_2O, which decomposes at 350 °C and easily evaporates.

The properties, however, justify the use of potassium as a modifying agent. The area of the hysteresis loop becomes much smaller, reducing the dielectric losses during repolarization. As an effect of the lowered remnant polarization, the remnant strain is also considerably reduced, making BNT-25BKT a possible starting material for actuator compositions.

BNT-25BKT crystallizes in the tetragonal modification of the perovskite with a cell volume of 119.5074 Å³. Differently to BNT, there are small peaks in the XRD pattern (Figure 13) between 30 ° and 40 °, which are the result of a secondary phase with the composition $K_2Ti_6O_{13}$. The formation of this phase is extensively covered in an research article[16].

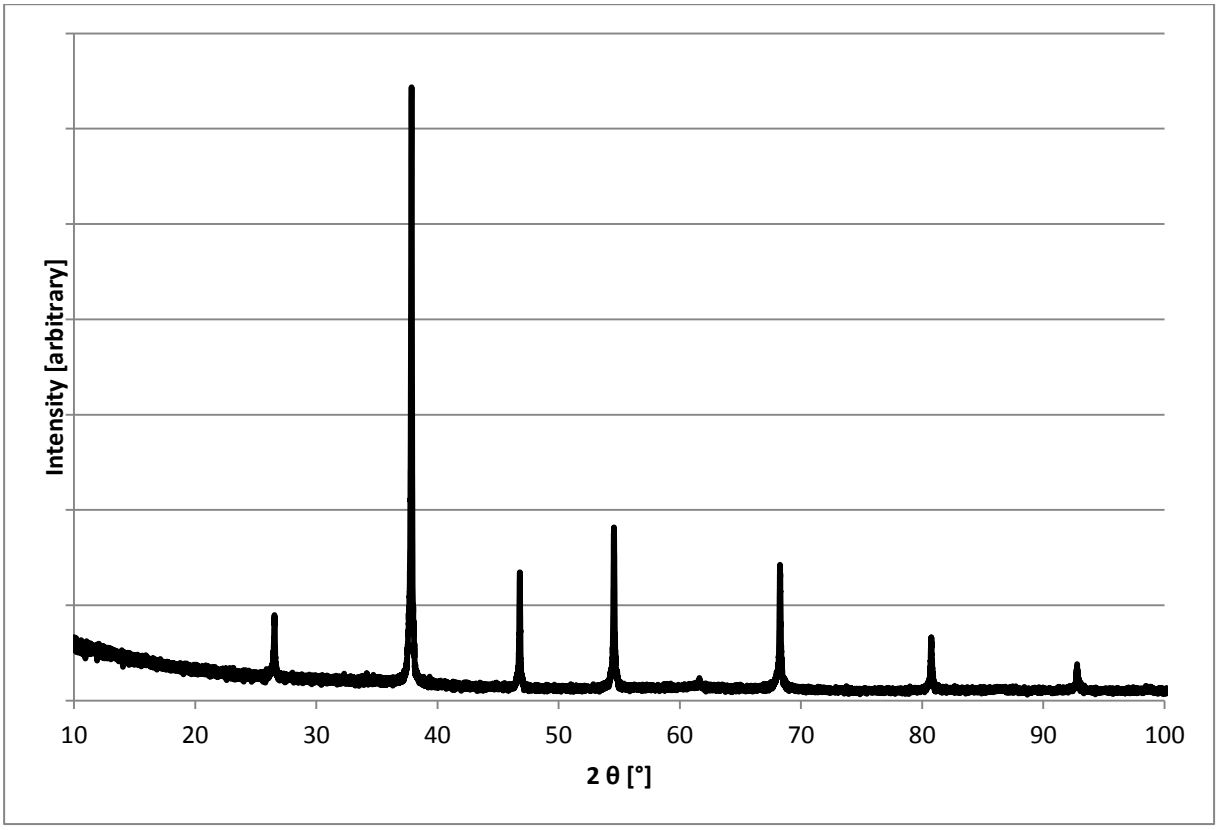


Figure 13: XRD pattern of BNT-25BKT.

The SEM image (Figure 14) of the microstructure again shows a dense, uniform grain structure in the ceramic. This material needs a slightly higher sintering temperature of 1150 °C to produce dense samples.

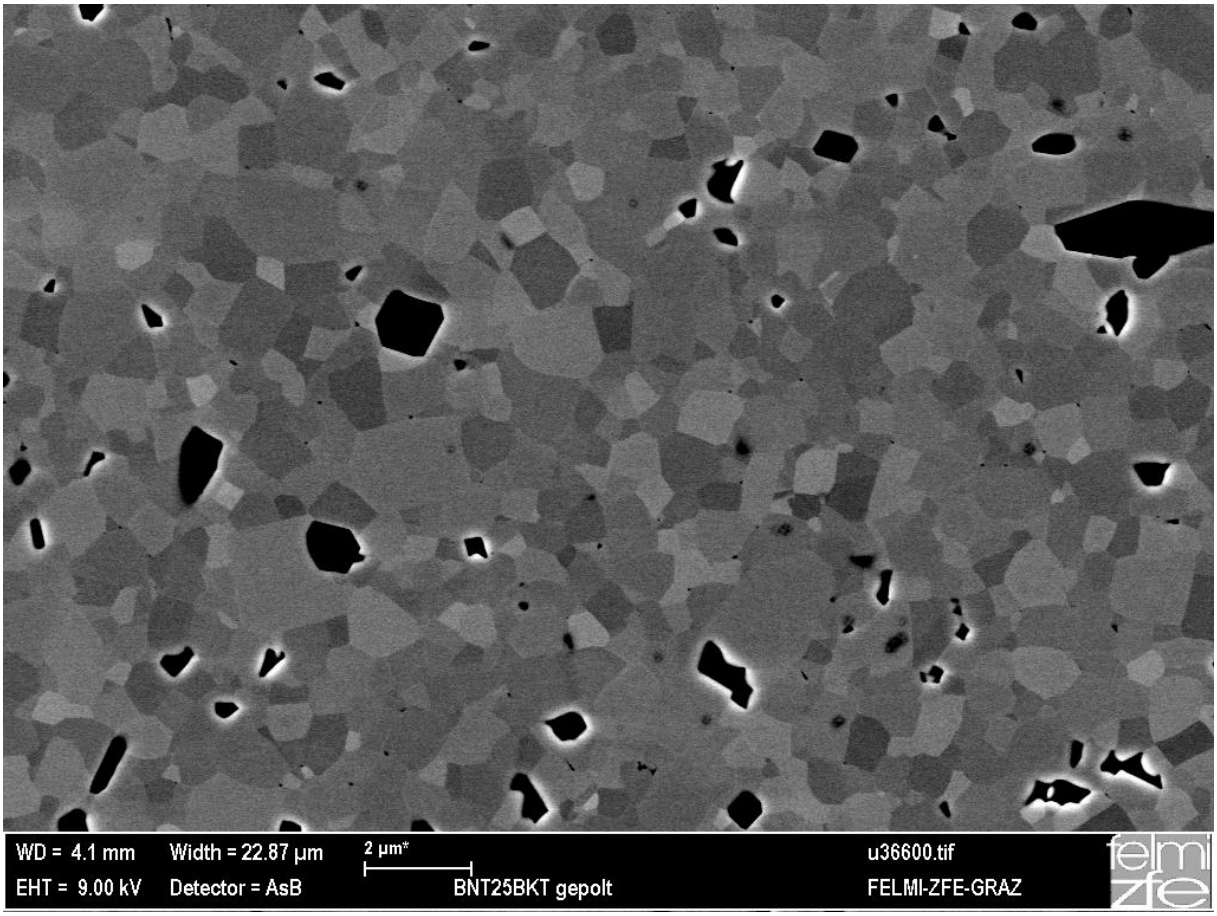


Figure 14: SEM image of the microstructure of BNT-25BKT, sintered at 1150 °C.

The average grain size is noticeable smaller than in pure BNT. Sintering at 1150 °C obviously is not high enough to produce samples as dense as BNT sintered at 1100 °C, but for our purposes the obtained density is sufficient. The cell volume of BNT and BNT-25BKT are not directly comparable, because BNT forms a rhombohedral perovskite and BNT-25BKT crystallizes in a tetragonal symmetry.

Table 6: Average grain size and cell volume of BNT-25BKT.

	BNT-25BKT
Grain size [µm]	0.56
Cell volume [Å³]	119.5074

The hysteresis loop (Figure 15) of BNT-25BKT shows a completely different behavior than BNT. The maximum polarization is only slightly lower, the remnant polarization and the coercive field drop to very low levels. The graph shows both hysteresis loops to enable a quick comparison.

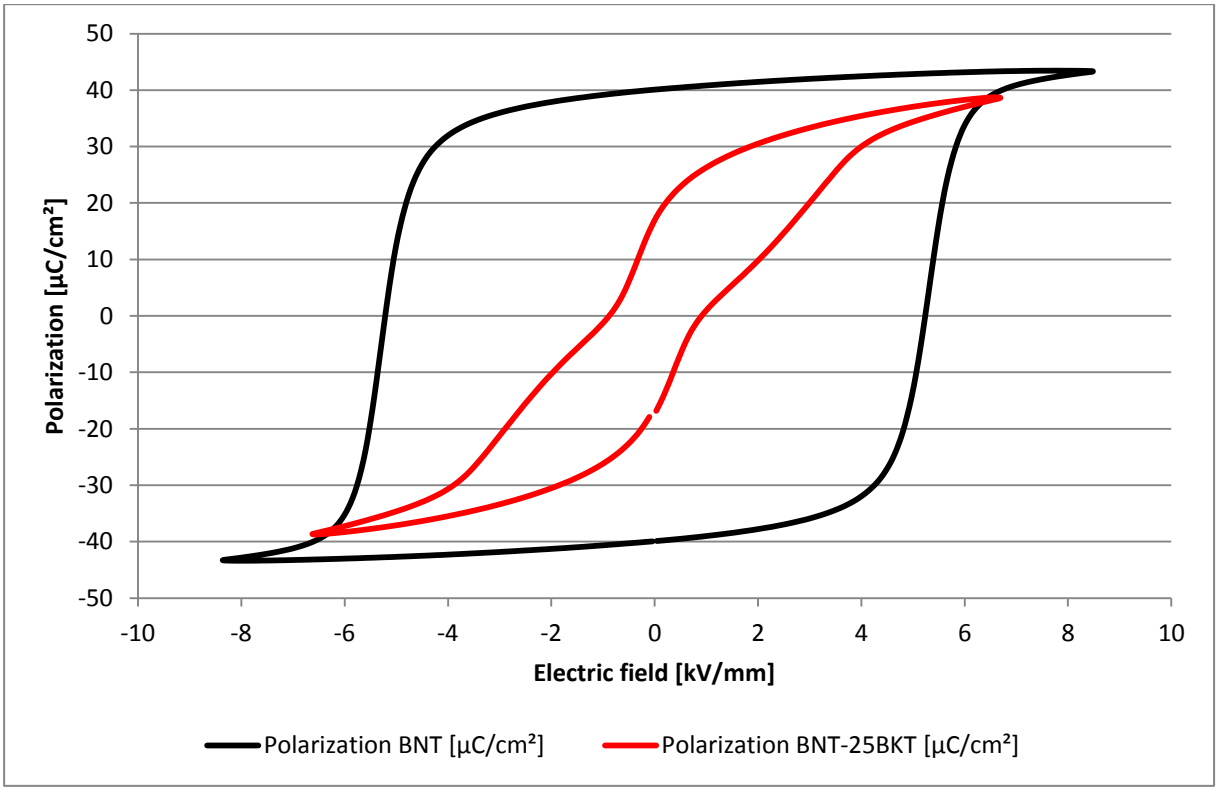


Figure 15: **Polarization loops for BNT and BNT-25BKT.**

The area of the hysteresis loop of BNT-25BKT is remarkably smaller compared to BNT. This also reduces the losses during repolarization under an alternating electric field, because the product of polarization and voltage is related to the energy stored in the material. During repolarization, most of this energy is dissipated as heat, so a small area hysteresis loop is highly favorable.

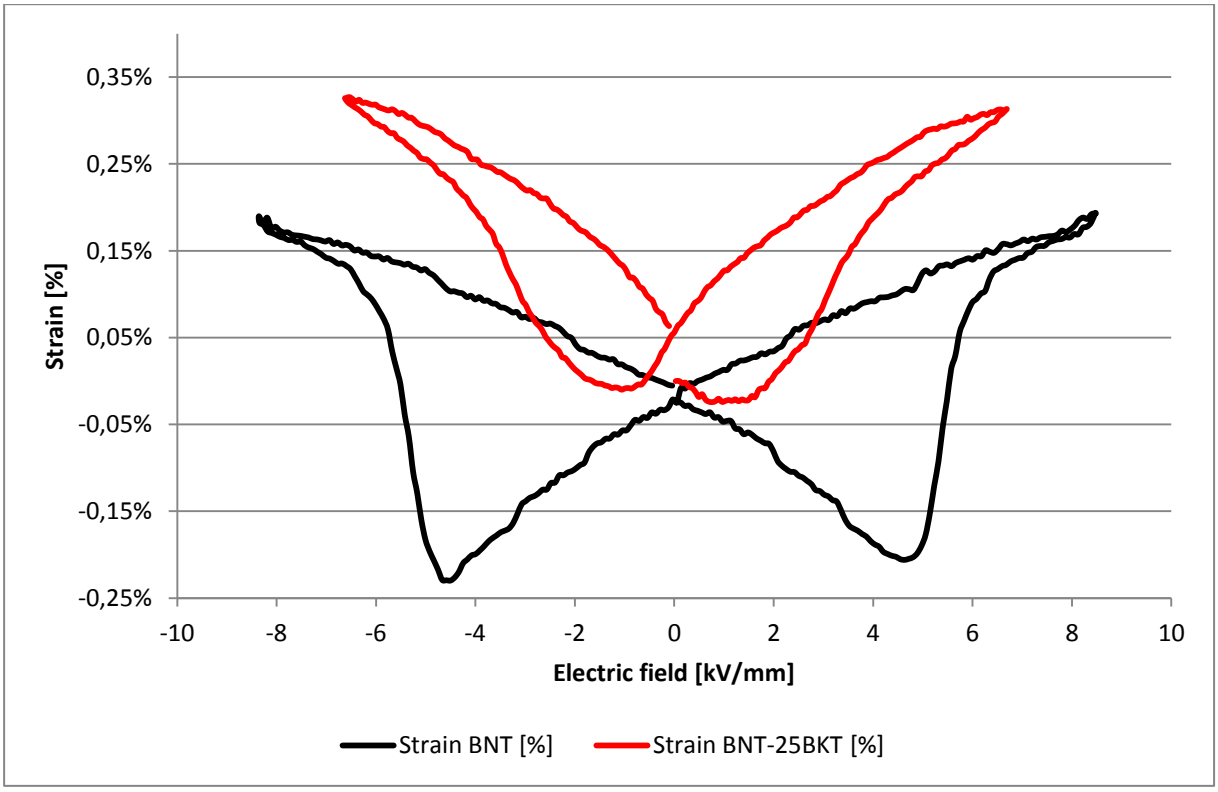


Figure 16: **Strain loops for BNT and BNT-25BKT.**

Figure 16 shows a comparison of the strain loops of BNT and BNT-25BKT. While BNT displays a textbook butterfly loop with a very high amount (approximately 0.23 %) of remnant strain, BNT-25BKT only shows a remnant strain of approximately 0.05 %. For actuator applications, this behavior is highly desired.

The temperature dependence of the permittivity and the loss factor of BNT-25BKT is displayed in Figure 17. Compared to BNT, the permittivity is higher at all temperatures. The transition temperature T_d is now located at lower temperatures and frequency dependant.

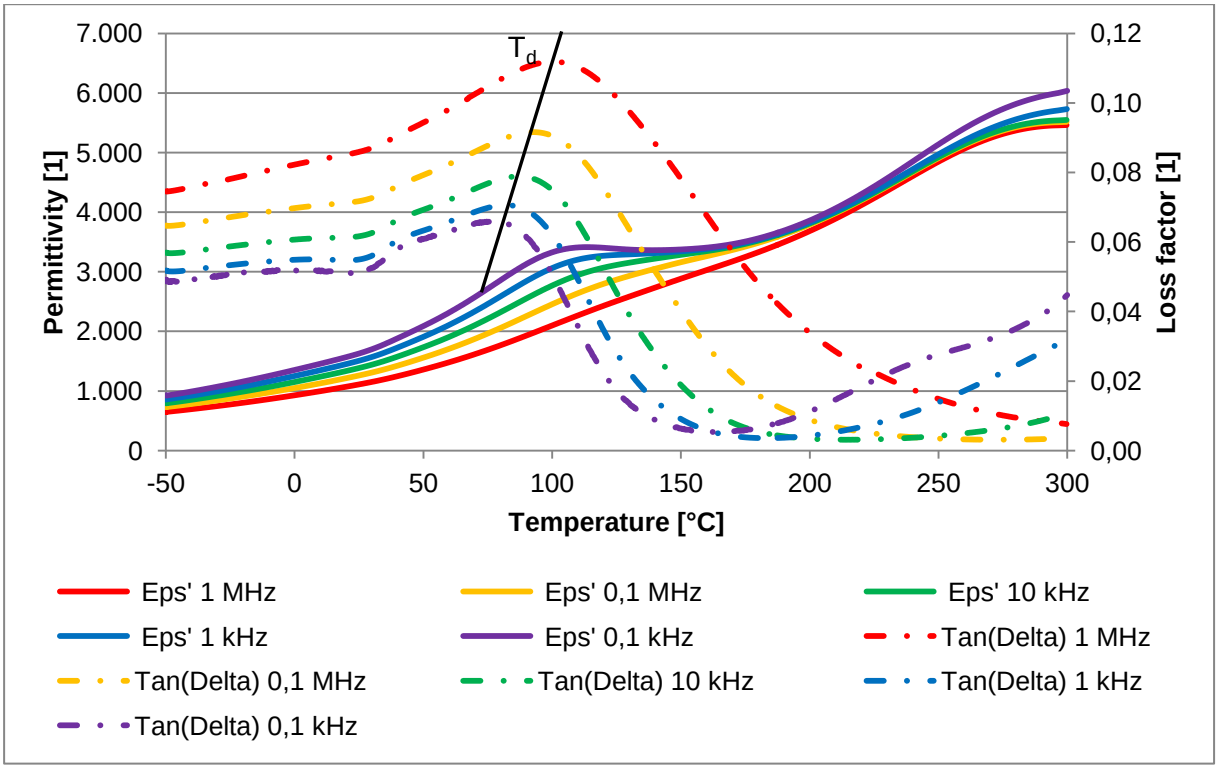


Figure 17: **Temperature dependence of permittivity and loss tangent in BNT-25BKT.**

Compared to BNT, the region between T_d and T_m with low losses and high permittivity becomes wider, which makes the material more useful. T_d is now strongly frequency dependant and located between 74 °C and 100 °C, with the first value for lower frequencies.

The overall performance of BNT-25BKT is much better than of BNT, which is a typical hard ferroelectric material. BNT-25BKT, albeit having high losses at room temperatures, excels at higher temperatures with a permittivity of approximately 3500 and very low losses. The downside of this material is the high affinity of titanium towards potassium, resulting in the formation of a secondary phase which can alter the composition[16].

4.3.Substitutions and donor doping on A- and B-site

In the first part section, the results of the experiments using Ca^{2+}, Ce^{4+} and Nb^{5+} as donor dopants are presented and discussed. The second part focusses on four out of five possibilities of isovalent titanium substitution in BNT. The basic compound in this chapter is BNT, because of its unproblematic synthesis. BNT-25BKT based compositions would probably be more interesting from the application point of view, but the tendency to form secondary phase inclusions is very problematic, when one wants to investigate the influence of a single doping element. All compositions have been prepared as described in chapter 3.1 with 1100 °C sintering temperature and 5 h sintering duration.

4.3.1. Donor doping with calcium

Calcium or more precisely Ca^{2+}, is one of many possible choices to replace Na^{+} with a M^{2+} ion. The reason it was used in this work is its ionic radius, being very close to Na^{+}, which it shall replace. Donor doping on the A-site creates, as described in chapter 2.5.1, vacancies in the lattice. Since 2 Na^{+} ions are replaced by one Ca^{2+} and one A-site vacancy, the electronic balance in the material is not affected. The vacancies generated with this method can also influence the ferroelectric behavior like in PLZT, mentioned in chapter 2.5.

BNT tends to reduce vacancies on both A- and B-site of the lattice during thermal treatment. This behavior has been studied in two publications from our group[16][33]. The situation is similar in the donor doped system. The XRD pattern (Figure 18) shows a reflection, caused by a secondary phase, starting at 1 % Ca^{2+} doping.

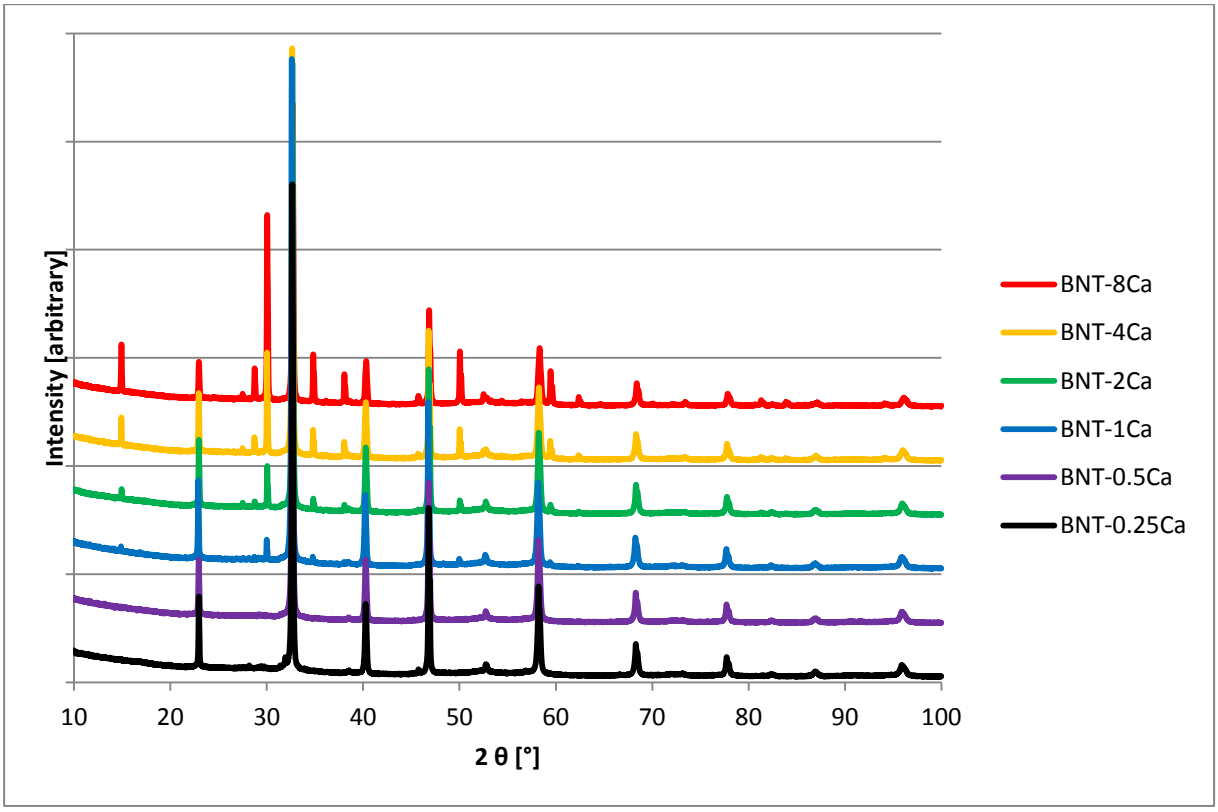


Figure 18: XRD patterns of donor doped BNT with calcium. The emerging peaks at Ca-concentrations > 0.5 % are caused by inclusions of $Bi_2Ti_3O_9$.

This secondary phase originates from a reaction caused by the vacancies introduced by donor doping. The material heals up those vacancies by forming a secondary phase (

Equation 13). This secondary phase consists of Bi^{3+}, Ti^{4+} and O^{2-}, which are residual excess after forming BNT and CT with a lower and stable vacancy concentration. BNT and CT still form a solid solution. The ionic radius of calcium is smaller than the radius of sodium, so a reduction of the cell volume can be anticipated.

Table 7: Comparison of the cell volume of BNT and calcium donor doped materials.

	BNT-0.25Ca	BNT-0.5Ca	BNT-1Ca	BNT-2Ca	BNT-4Ca	BNT-8Ca
Cell volume [Å³]	352.0713	352.0586	351.8907	351.8261	351.3069	350.4247

Equation 13: Decomposition reaction of calcium donor doped BNT.

The decomposition reaction effectively reduces the vacancy concentration by forming two ferroelectrically inactive products, $Bi_2Ti_2O_7$ and TiO_2. These compounds form solid solutions over a very broad compositional range, structurally building a network of cornerlinked $[TiO_6]^{2-}$ octahedrons

and intercalated layers of $[Bi_2O_2]^{2+}$. At a doping level of 8 %, the resulting material BNT-8Ca consists of 83 % active material, forming a solid solution of 89 % BNT and 11 % CT and 17 % secondary phase with the summarized composition $Bi_2Ti_3O_9$.

The hysteresis loops shown in Figure 19 also resemble the decomposition behavior. The maximum polarization drops continuously with rising calcium content; as a product of the decomposition and the resulting lower amount of active phase.

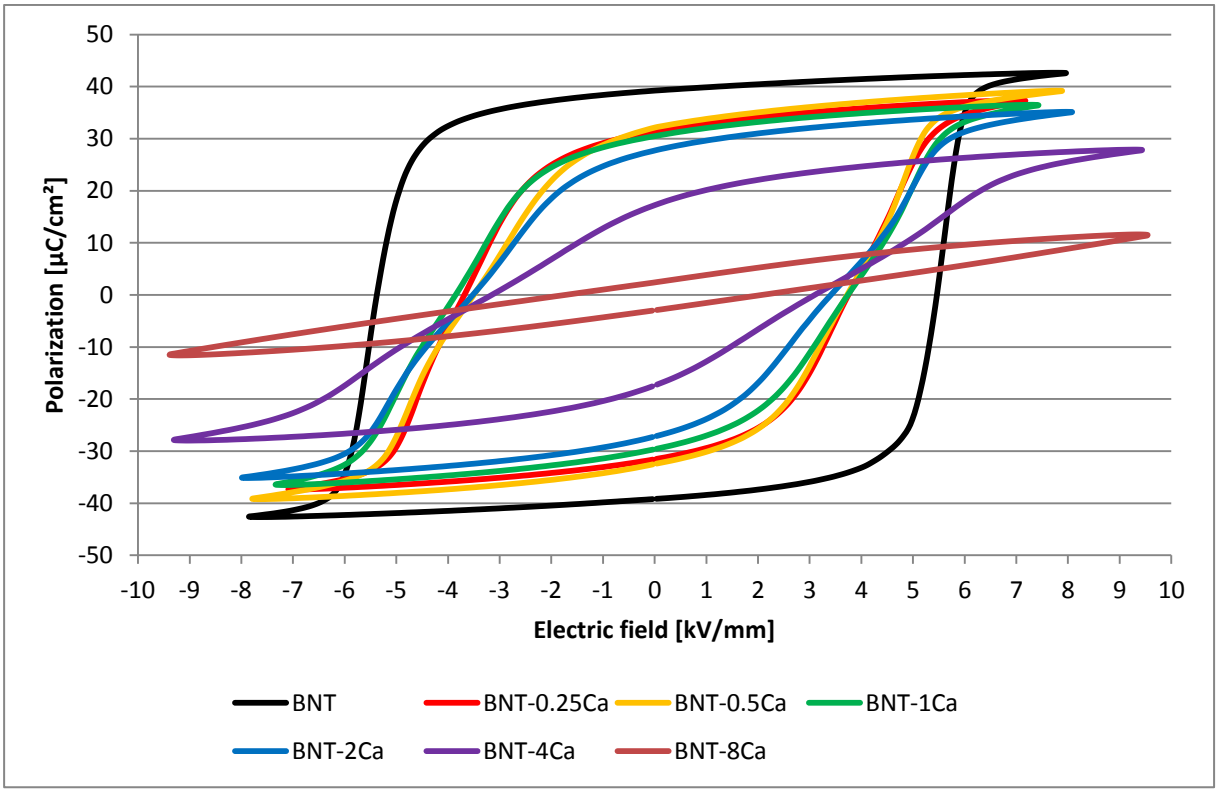


Figure 19: **Hysteresis loops of Ca-donor doped BNT.**

The influence on the hysteresis loops is clearly visible, even at low doping levels of 2 % Ca. With rising dopant concentrations, the electric field needed for saturation gets higher; at 8 % it was not possible to reach saturation with disc-shaped samples with a thickness close to 1 mm. Also, as mentioned shortly before, the maximum polarization drops due to the rising amount of inactive volume, occupied by the secondary phase.

The compositions BNT-0.25Ca and BNT-0.5Ca show no signature of the secondary phase inclusions in the XRD-pattern and their hysteresis loops are almost congruent. It can therefore be assumed, that these materials are in proximity to the maximum A-site vacancy concentration for BNT, lying close to 0.5 % $V_{a'_{Na}}$. Compared to PLZT, this is a rather low value, but it still has a noticeable effect on

lowering the ferroelectric hardness of the material. Combined with other influences, this material behavior can be used to prepare a compound with favorable properties.

4.3.2. Donor doping with cerium

As mentioned in chapter 2.5.2, cerium as Ce^{4+} is the only suitable donor substituent for Bi^{3+} in the periodic table. Every other ion M^{4+} is, due to the ionic radius, a substituent for Ti^{4+}. The only exception is Te^{4+}, which is a very big ion with an ionic radius of 1.90 Å in 12-fold coordination. The substitution of $-\ Bi^{3+}$ with x Ce^{4+} creates $-$ vacancies on the A-site of the perovskite lattice. The motivation of this doping method is similar to Ca-donor doping in the previous chapter and basically based on the behavior of PLZT ceramic.

Compared to the Ca^{2+} donor-doped material, Ce^{4+} donor-doping creates far less vacancies. In practice, this results in a higher dopant concentration. Cerium doping also reduces the concentration of highly polarizable bismuth in the material, so a lowered maximum polarization can be anticipated. Ce^{4+}(XII) has an ionic radius of 1.14 Å which is lower than the ionic radius of Bi^{3+}(XII) with 1.45 Å; a result is more lattice distortion and higher possibility of secondary phase formation. The XRD-pattern (Figure 20) shows no indication of a secondary phase, but a visible shift to bigger angles at high cerium concentrations.

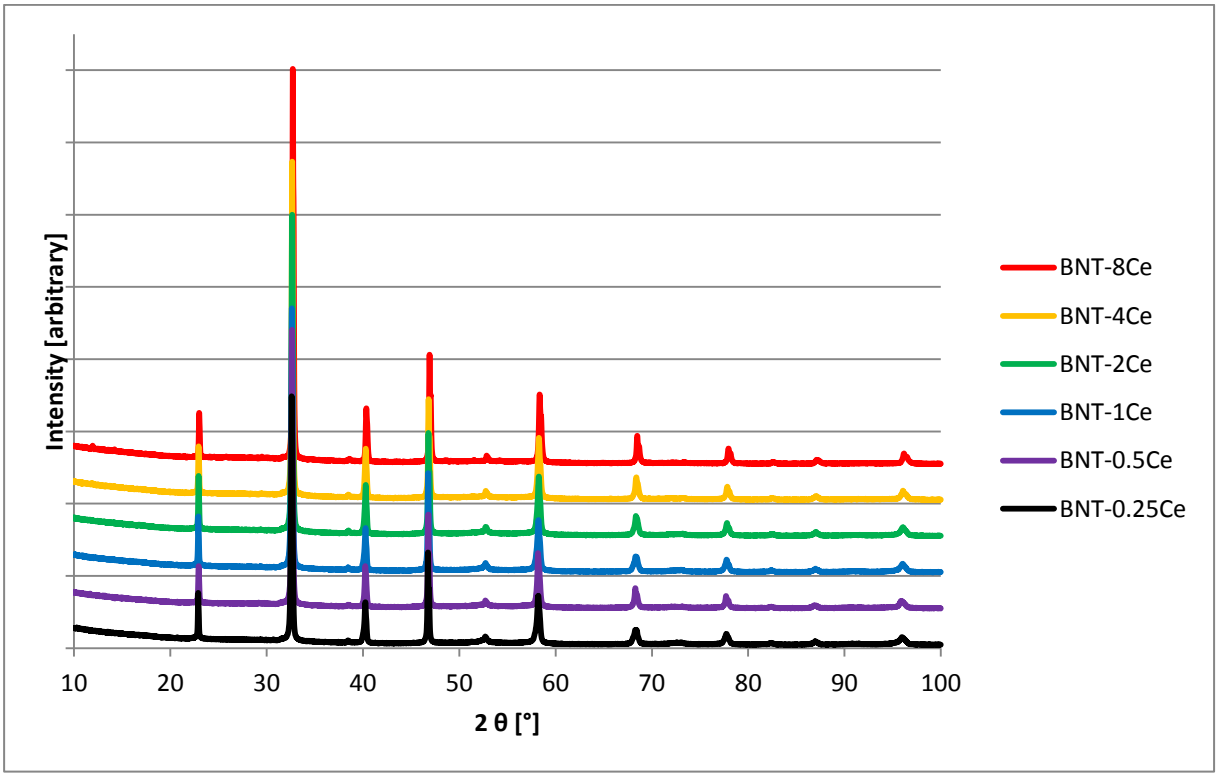


Figure 20: XRD patterns of BNT donor doped with cerium.

The before mentioned shift of the peaks to bigger angles is caused by a reduction of the lattice parameters and as a result, lower cell volume. This behavior is a direct consequence of the substitution of the big ion bismuth with the 22 % smaller cerium.

Table 8: Comparison of the cell volume of BNT and Ce donor doped materials

	BNT-0.25Ce	BNT-0.5Ce	BNT-1Ce	BNT-2Ce	BNT-4Ce	BNT-8Ce
Cell volume [Å³]	351.5359	351.3458	351.2015	350.8204	350.2841	349.3787

The decrease of cell volume also is a strong indication that cerium is accepted as a substituent for bismuth in the perovskite lattice. This observation supports the lack of secondary phase reflections in the XRD pattern.

The high field electrical measurements shown in Figure 21 display an uncommon behavior. Up to 2 % cerium doping, the maximum polarization drops as anticipated, at 4 % and 8 % cerium doping, the losses rise to a very high level and the hysteresis loops get lemon-shaped.

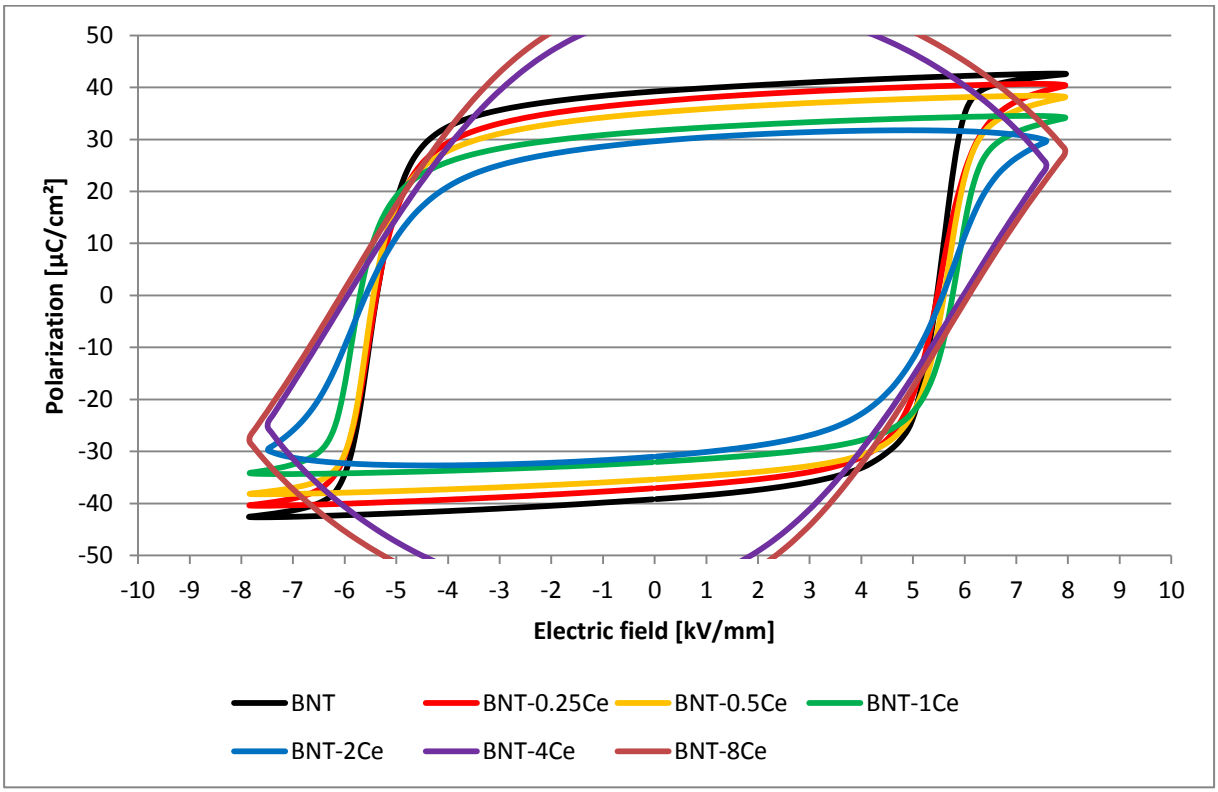


Figure 21: Hysteresis loops of Ce-donor doped BNT.

As an explanation for the lossy behavior at high cerium concentrations it is worth mentioning, that the samples get darker with higher doping levels. The samples with a cerium content ≤ 2 % have a yellow-brown tone, the sample with 4 % cerium is dark-brown, and the sample with 8 % cerium is

almost black. In oxides, color is usually the result of the band gap of the material, meaning that the samples with high cerium content are more likely to be semiconductors than isolators. Since there are no visible secondary phase inclusions according to XRD, the only cause for this property has to be the vacancy concentration on the A-site.

The most interesting result of this section is the obvious possibility of introducing vacancies on the A-site by bismuth substitution. While the calcium doped / sodium substituted materials start the formation of a secondary phase at an A-site vacancy concentration of 1 % (see sample BNT-1Ca in Figure 18), the substitution of bismuth with cerium does not lead to problem up to 2 % A-site vacancies. Compared to PLZT, donor doping does not stabilize an antiferroelectric phase in BNT, but promotes semiconductor-like behavior.

4.3.3. Donor doping with niobium

A different approach of doping in BNT is donor doping on the B-site of the lattice. In this case, titanium is substituted with an ion with higher valence; in this case niobium is used. Donor doping, as described in chapter 2.5.3 does not create oxygen vacancies and should therefore not cause problems at higher temperatures.

The substitution of – titanium with one niobium only creates – vacancy on the B-site. In BNT, the network of cornerlinked $[TiO_6]^{2-}$ octahedrons forms the structural backbone, the effects of disturbing this network can be very high, even at low concentrations of the dopant. The integrity of this structure is again preserved by decomposition of the material, visible in the XRD-pattern (Figure 22).

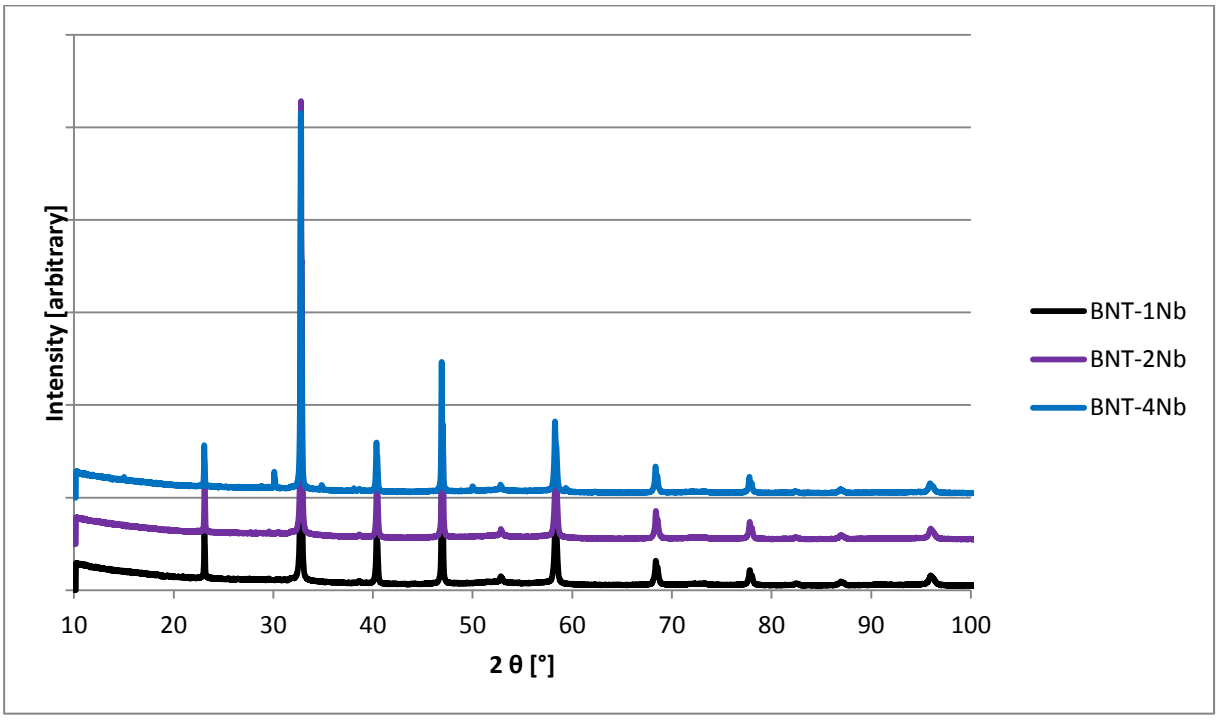


Figure 22: **XRD patterns of donor doped BNT with niobium. The emerging peaks at Nb-concentrations > 2 % are caused by inclusions of $Bi_2Ti_2O_7$.**

Niobium is a bigger ion than titanium, so the cell volume of the doped material rises with higher niobium concentrations:

Table 9: **Comparison of the cell volume of BNT and niobium donor doped materials.**

	BNT	BNT-1Nb	BNT-2Nb	BNT-4Nb
Cell volume [Å³]	351.8229	352.6692	352.8896	353.2225

The reflections caused by the secondary phase inclusions in the XRD-pattern are produced by $Bi_2Ti_2O_7$, a compound that was also formed by a decomposition reaction of calcium donor-doped material. The reaction in this case could not be exactly determined and most likely contains an evaporation of excess bismuth oxide to form a compound with a stable vacancy concentration. The remaining material is a solid solution of BNT, NN and a bismuth / titanium-rich secondary phase. The acceptable vacancy concentration on the B-site of the perovskite structure is below 1 %, higher values lead to decomposition.

Despite the low achievable vacancy concentration, the impact of donor doping on the B-site of the perovskite is very high. The hysteresis loops are displayed in Figure 23.

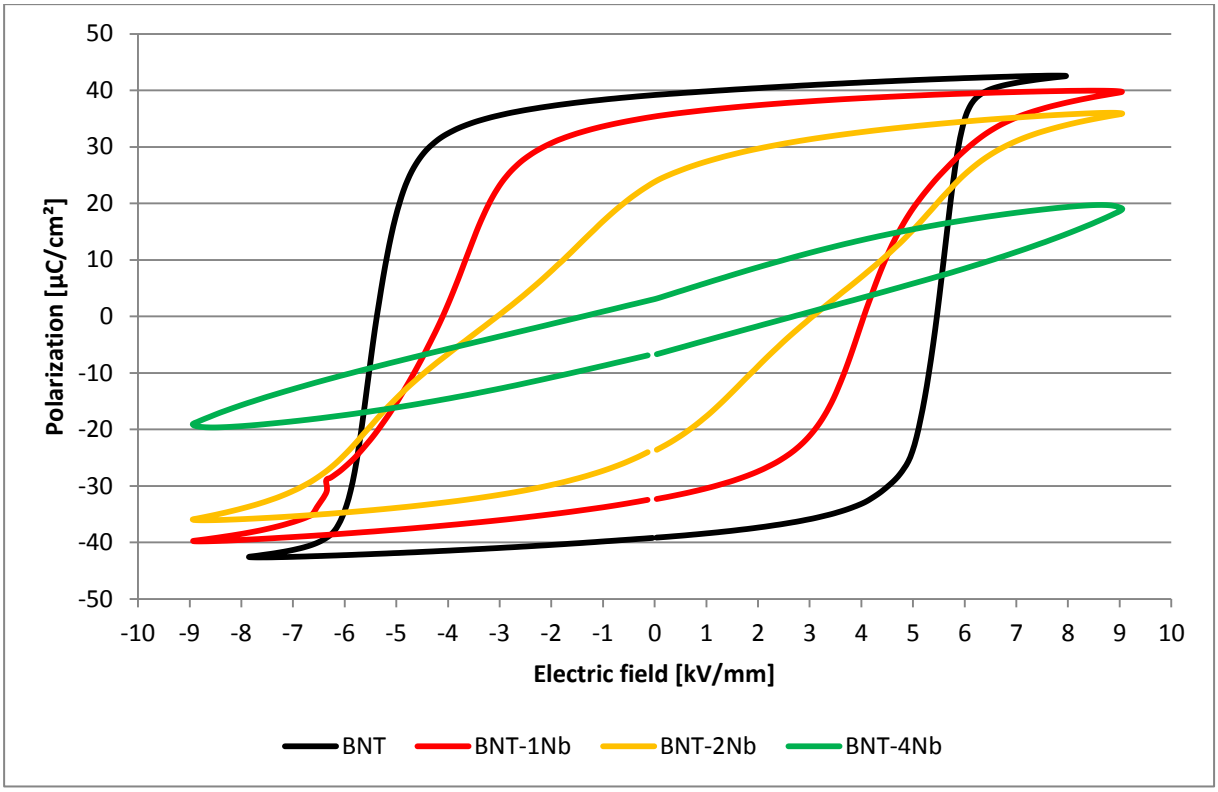


Figure 23: **Hysteresis loops of Nb-donor doped BNT.**

The impact on the ferroelectric parameters E_c and P_r are very high, considering the low amount of dopant and resulting vacancies. Since the material contains as much bismuth as BNT, the maximum polarization is very little affected by this doping method. The necessary electric field to achieve saturation in the material rises with higher dopant concentration, at 4 % niobium concentration, the used measurement setup was not sufficient to reach the high fields needed for saturation. This behavior is in accordance with the decomposition of niobium doped BNT to BNT and NN; as NN is considered antiferroelectric in literature[34]. The result of this chapter show, that donor doping

using niobium is a suitable way to reduce ferroelectric parameters without reducing the maximum polarization at high electric fields.

4.3.4. Substitution of titanium with germanium

Germanium is one of the possible elements that can substitute titanium in BNT. Its main differences are the smaller ionic radius (see Table 2 in chapter 2.4.1) and the d^{10} electron configuration, which results in a high electron density on the B-site of the perovskite. Since germanium is isovalent with titanium, this substitution does not create vacancies of any kind in the lattice.

The small radius of Ge^{4+}(XII) leads to problems during the formation of the perovskite, visible in the XRD-pattern shown in Figure 24. At germanium concentrations ≥ 4 %, reflections caused by a secondary phase become visible.

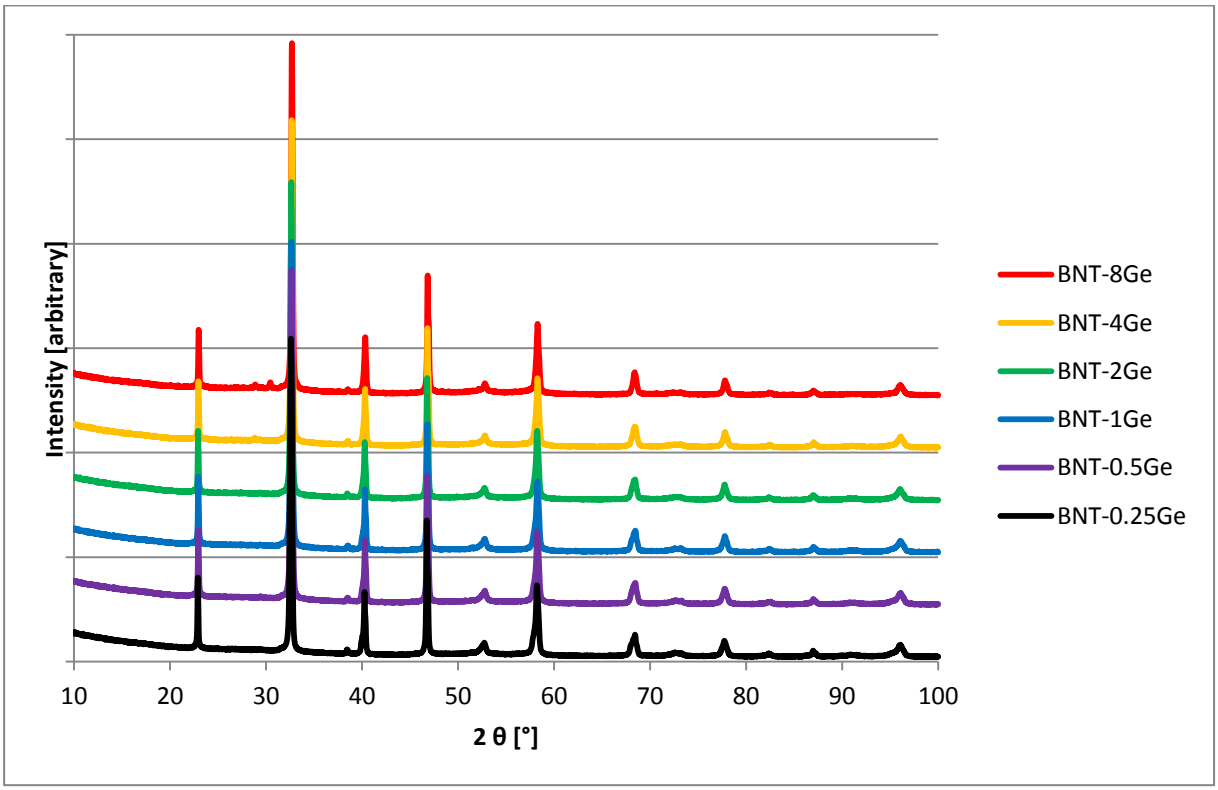


Figure 24: **XRD patterns of Ti-substituted BNT with germanium.**

The emerging reflection of the secondary phase is again caused by a compound with the composition $Bi_2Ti_2O_7$. It is the result of a decomposition reaction caused by the insertion of the very small Ge^{4+}-ion. With the exception of 0.5 % and 8 % germanium, the cell volume shrinks with higher germanium content. The spike at 0.5 % is most likely caused by sample preparation (e.g. coarse grain size for powder samples), the spike at 8 % can be caused by the decomposition. The average grain size of sintered samples and the cell volume are shown in Table 10.

Table 10: Comparison of the cell volume of BNT and Ge doped materials.

	BNT-0.25Ge	BNT-0.5Ge	BNT-1Ge	BNT-2Ge	BNT-4Ge	BNT-8Ge
Grain size [µm]	2.6	2.0	2.5	0.9	1.0	1.0
Cell volume [Å³]	351.8491	352.0682	351.7598	351.7562	351.4841	351.8185

The high field polarization loops (Figure 25) show a drop of the maximum polarization only. The coercive field is virtually constant, regardless the germanium content.

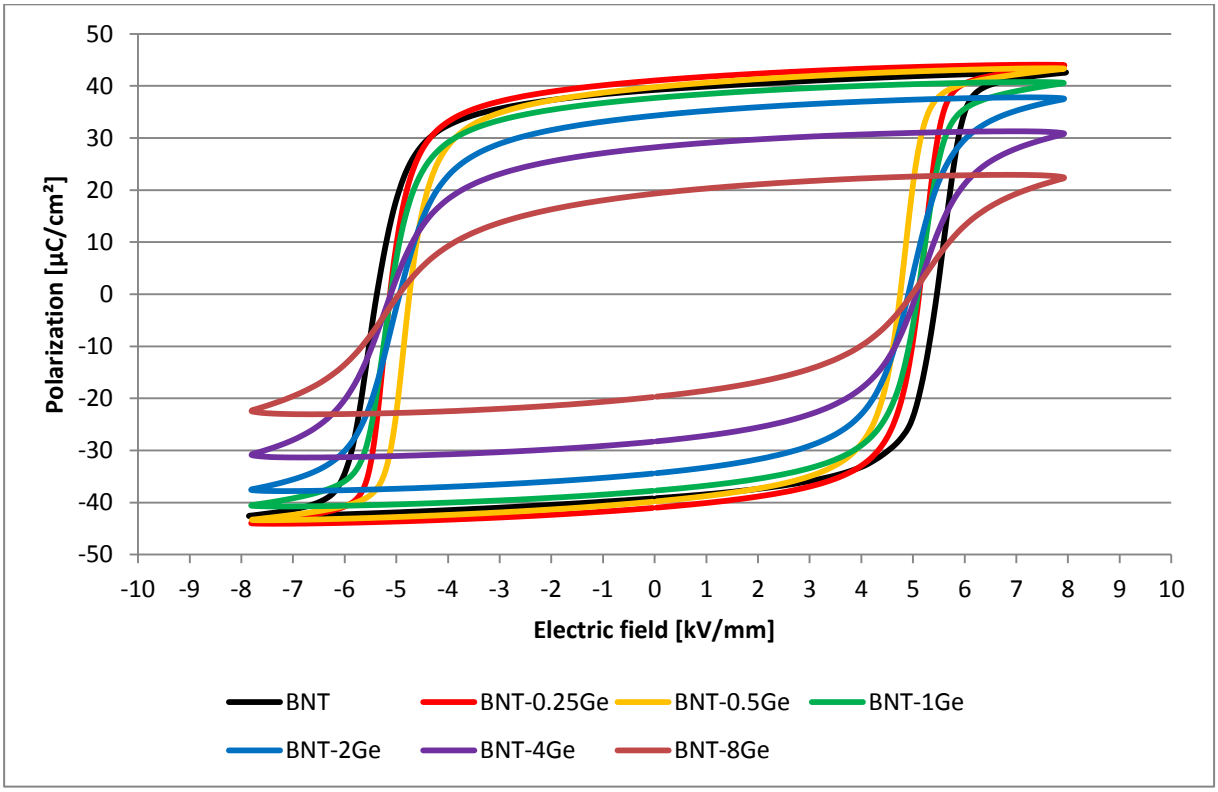


Figure 25: Hysteresis loops of Ge-doped BNT.

Beside the drop of the maximum polarization at higher germanium concentration, this substitution has no influence on the hysteresis loops. The sintering behavior is rather unsatisfactory with low densification, but strong deformation of the disc shaped samples. The low relative density also causes lower polarizability and higher losses.

Since the deviation of size and atomic weight to the substituted titanium is quite small, the influence of germanium doping on the temperature dependence is low, as can be seen in Figure 26.

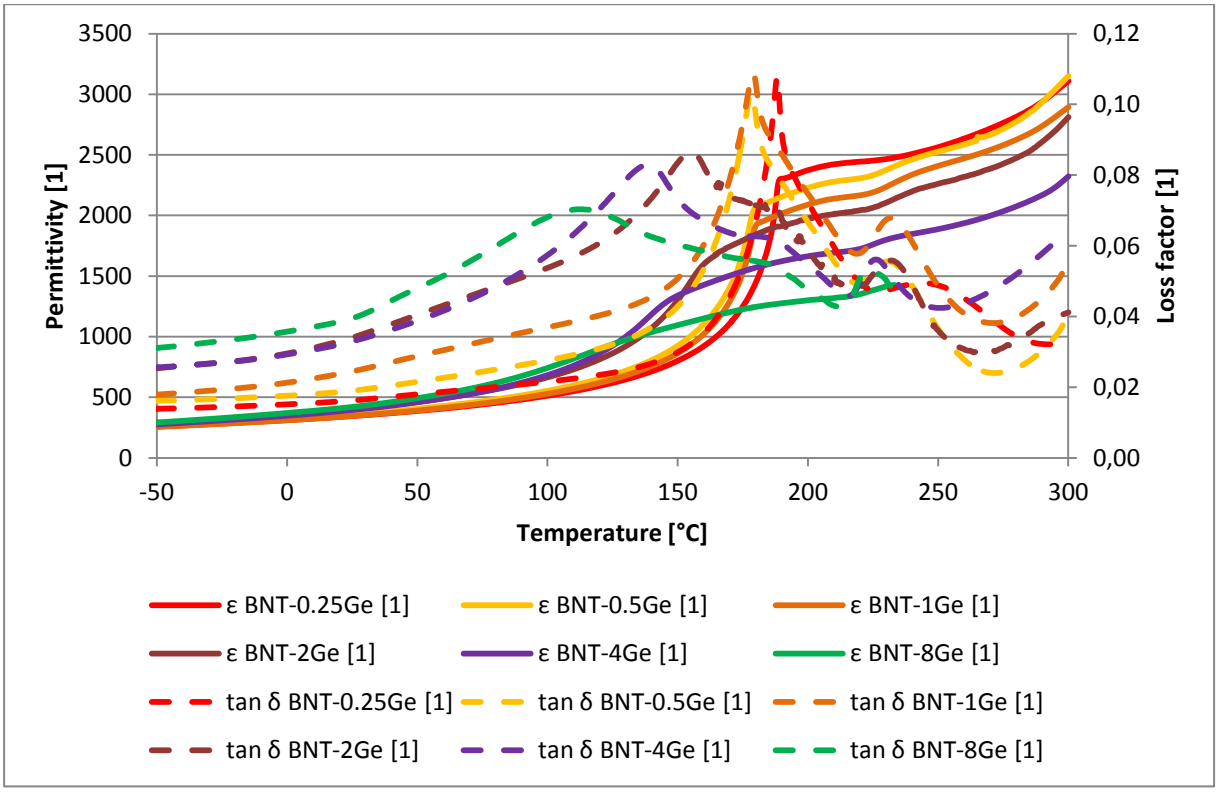


Figure 26: **Temperature dependence of permittivity and loss tangent in BNT-xGe.**

Germanium lowers the depolarization temperature significantly, but the impact is very low. At 8 % doping level, T_d lies at 112 °C. Considering the difficult sintering behavior, germanium is no favorable dopant for BNT, at least as a single method.

4.3.5. Substitution of titanium with tin

A different element usable to introduce a d^{10}-ion on the B-site of the perovskite is tin. Tin is located directly under germanium in the periodic table, a circumstance that results in a bigger ionic radius than germanium; Sn^{4+}(VI) is slightly larger than Ti^{4+}(VI) and should therefore fit nicely into the lattice.

Compared to germanium, tin is known to form perovskite structures with earth alkaline metal ions like calcium or strontium. This is also a direct consequence of the close-to titanium ionic radius. In BNT, because of these properties, no miscibility problems are expected. The XRD-pattern (Figure 27) shows a single phase up to samples with 8 % titanium substituted by tin.

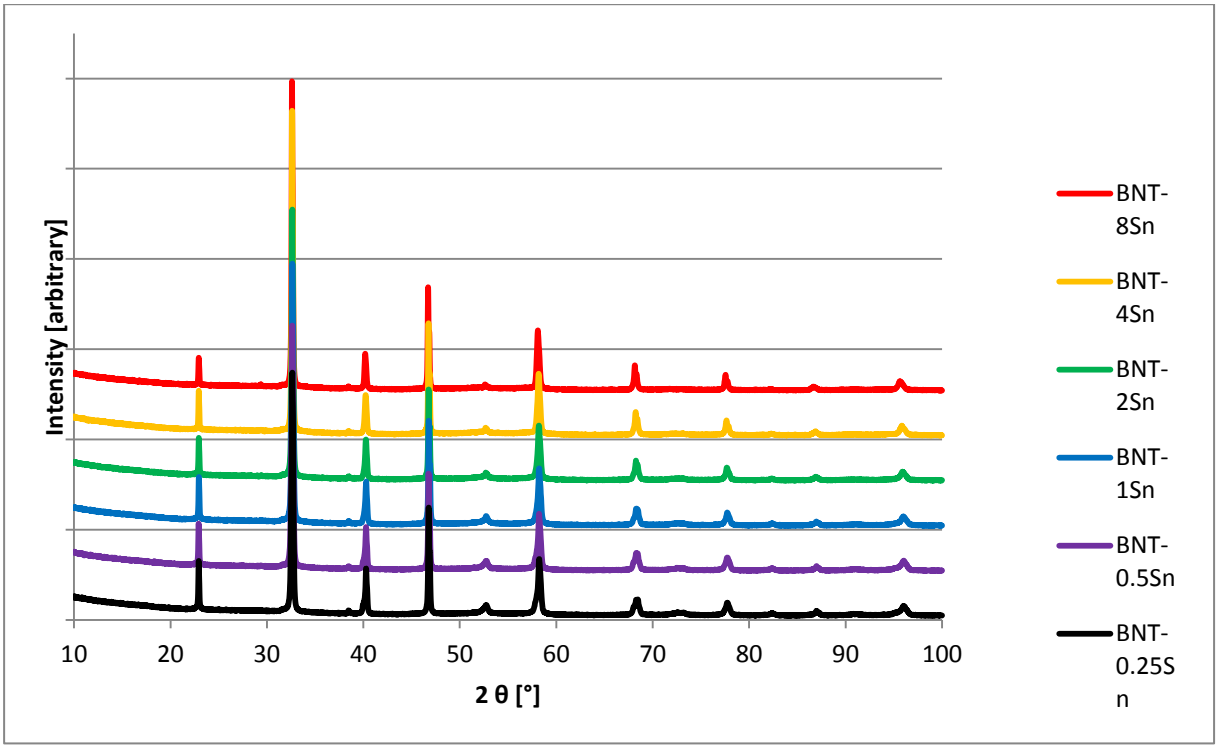


Figure 27: XRD patterns of Ti-substituted BNT with tin.

At high titanium substitutions, a shift of the reflection positions to smaller angles is visible. Due to the larger radius of tin compared to titanium, the volume of the unit cell of the material grows with higher tin content. Table 11 shows the influence of tin doping on the grain size and the cell volume.

Table 11: Comparison of the cell volume of BNT and tin doped materials.

	BNT-0.25Sn	BNT-0.5Sn	BNT-1Sn	BNT-2Sn	BNT-4Sn	BNT-8Sn
Grain size [µm]	6.7	3.6	2.5	7.3	1.6	1.8
Cell volume [Å³]	351.9682	351.8171	352.0279	352.4504	352.9688	354.7461

The grain size of BNT is highly affected by the addition of tin. The maximum grain size is achieved at 2 % tin content with 7.3 µm. The growth mechanism has not been studied in this work, but the high influence of small doping variations is definitely worth mentioning. The cell volume resembles the substitution of an ion with a larger counterpart which results in a growing cell volume.

The hysteresis loops in Figure 28 show a very interesting behavior. While the influence of germanium in the previous chapter is limited to the maximum polarization, tin behaves completely different.

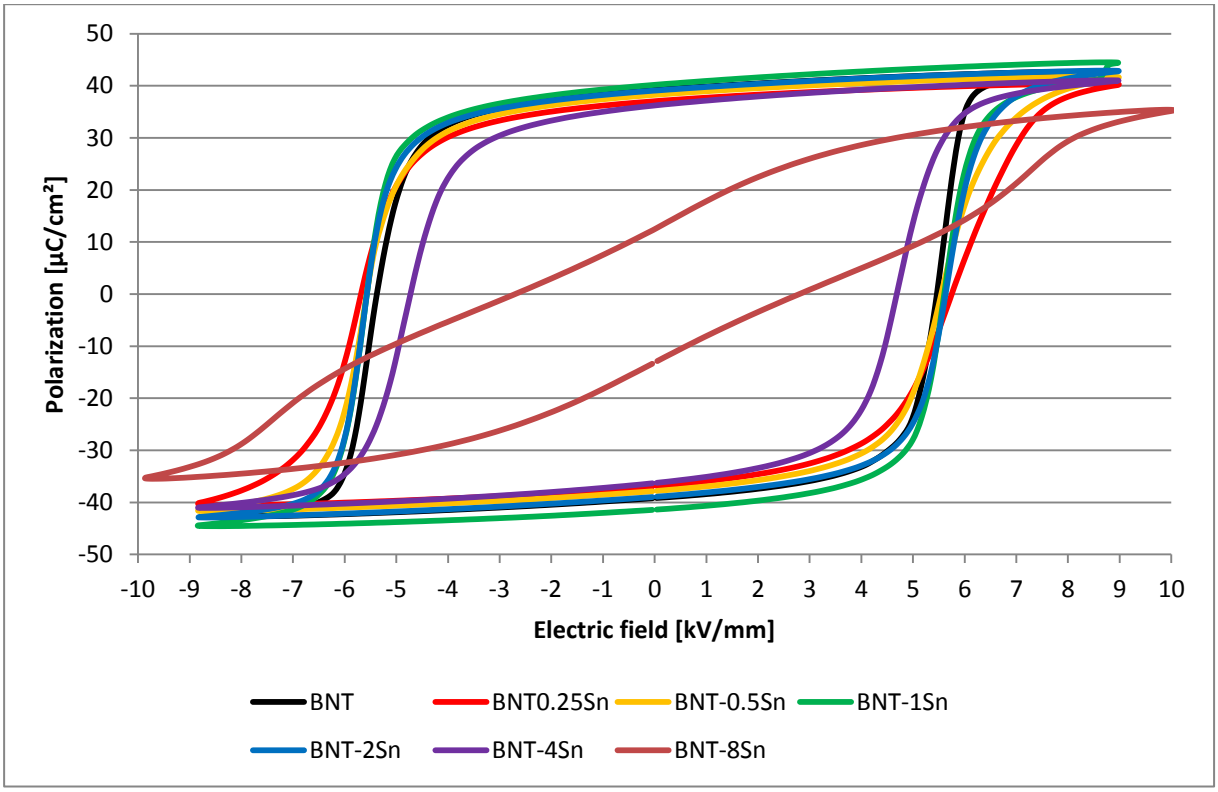


Figure 28: **Hysteresis loops of Sn-doped BNT.**

At low tin concentrations, there is very little change in the polarization loop compared to BNT; E_c, P_r and P_{max} stay virtually constant up to 2 % tin content. At 4 % tin content, the coercive field drops to a significantly lower level while the other ferroelectric parameters stay unaltered. Tin contents of 8 % drastically change the shape of the hysteresis loop. Instead of a standard hard ferroelectric loop as usual in BNT, the values for E_c and P_r drop to very low values. Also, the needed electrical field to achieve maximum polarization rises to 10 kV /mm (other compositions: 8.5 kV/mm). These new properties of BNT-8Sn result in a strongly reduced area of the hysteresis loop with only slightly reduced maximum polarization; overall most favorable material characteristics.

Tin is more than twice as heavy as the replaced titanium, also its ionic radius is 14 % larger. Also, there is the possible impact of the high electron density due to its d^{10} configuration. The combined influences of these properties are summarized in Figure 29.

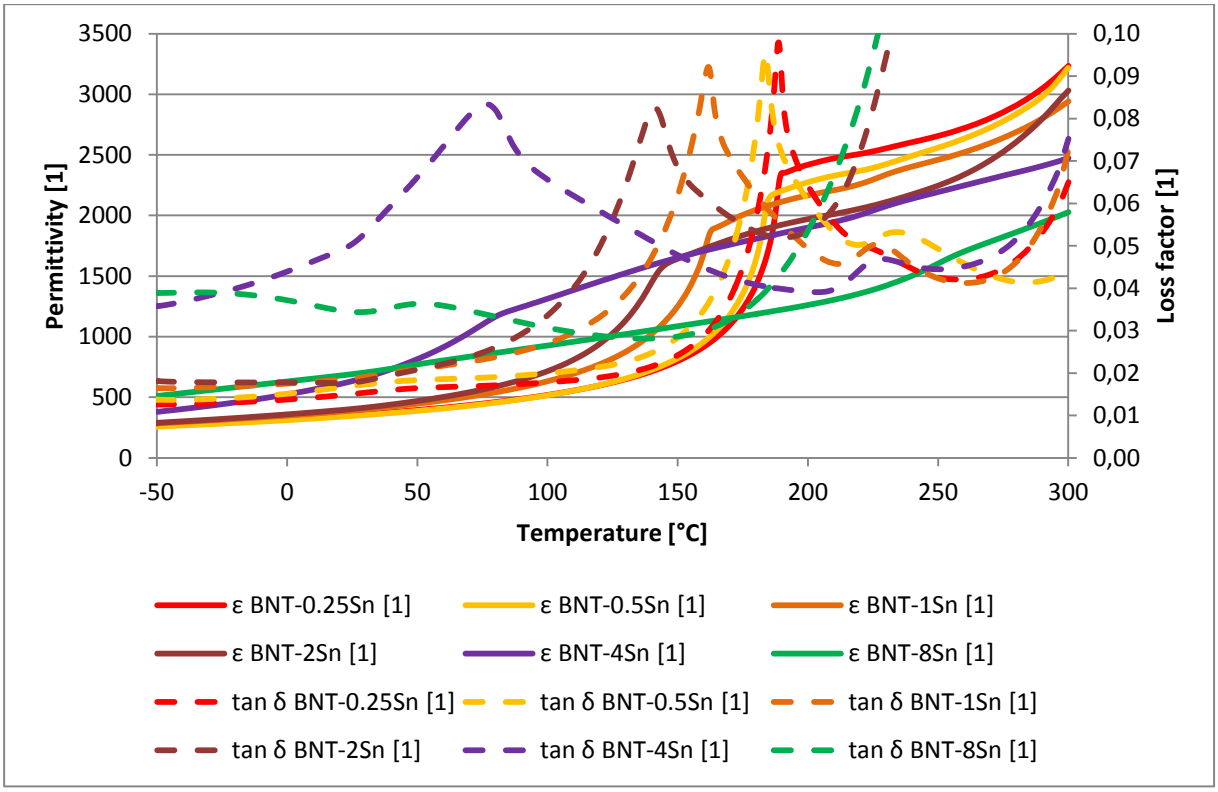


Figure 29: **Temperature dependence of permittivity and loss tangent in BNT-xSn.**

Tin effectively shifts T_d to lower levels. The substitution of 4 % titanium by tin results in a T_d of 75 °C. The depolarization temperature only appears as a sharp peak in the loss tangent graph in poled samples. Since the composition with 8 % tin is very hard to pole and shows very little remnant polarization, T_d could not be determined here. Because of the unchanged sintering properties and the big influence on the temperature dependence, tin is a highly recommended dopant in BNT.

4.3.6. Substitution of titanium with zirconium

The probably most obvious substituent of titanium in BNT is zirconium. Zirconium is widely used as doping agent in PZT and can alter the electrical properties of PZT dramatically. The ionic radius of zirconium is about 20 % larger than the radius of titanium and it is slightly larger than tin. The main difference between zirconium and tin is the electronic structure (Zr^{4+}: d^0, Sn^{4+}: d^{10}).

Like tin, zirconium also forms perovskites with earth alkaline ions, so miscibility problems are not to be expected. The larger ionic radius should again lead to a growth of the volume of the unit cell, even larger than the increase in tin doped materials. The XRD-pattern (Figure 30) shows no trace of secondary phase reflection up to doping contents of 8 % zirconium.

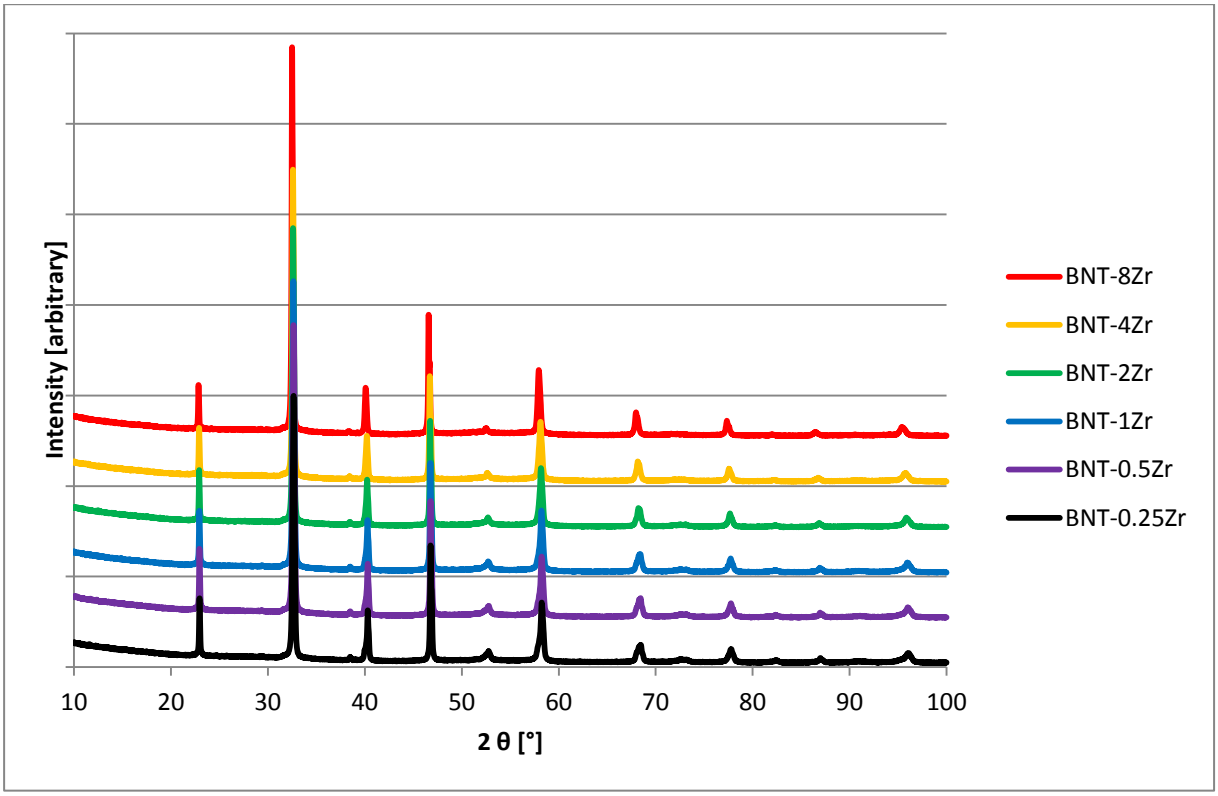


Figure 30: XRD patterns of Ti-substituted BNT with zirconium.

The reflections in the pattern above again shift to smaller angles at higher zirconium contents, a direct consequence of the larger ionic radius compared to titanium. The growth of the unit cell is presented in Table 12.

Table 12: Comparison of the cell volume of BNT and zirconium doped materials.

	BNT-0.25Zr	BNT-0.5Zr	BNT-1Zr	BNT-2Zr	BNT-4Zr	BNT-8Zr
Grain size [µm]	2.4	3.5	6.4	1.5	1.1	1.2
Cell volume [Å³]	352.2592	352.1758	352.3360	352.7252	354.0030	356.4846

The grain size is again influenced by the dopant concentration with comparable influences as tin doping. The cell volume again shows a trend to increase with higher doping levels. This conforms to the large radius of zirconium. The influence is remarkably bigger compared to the volume growth in tin whose radius is only 0.03 Å lower.

The polarization loops displayed in Figure 31 show a quite similar behavior to the samples doped with tin, at low dopant concentrations the influence on the shape of the hysteresis loop is almost negligible, at 8 % zirconium substitution the behavior changes dramatically.

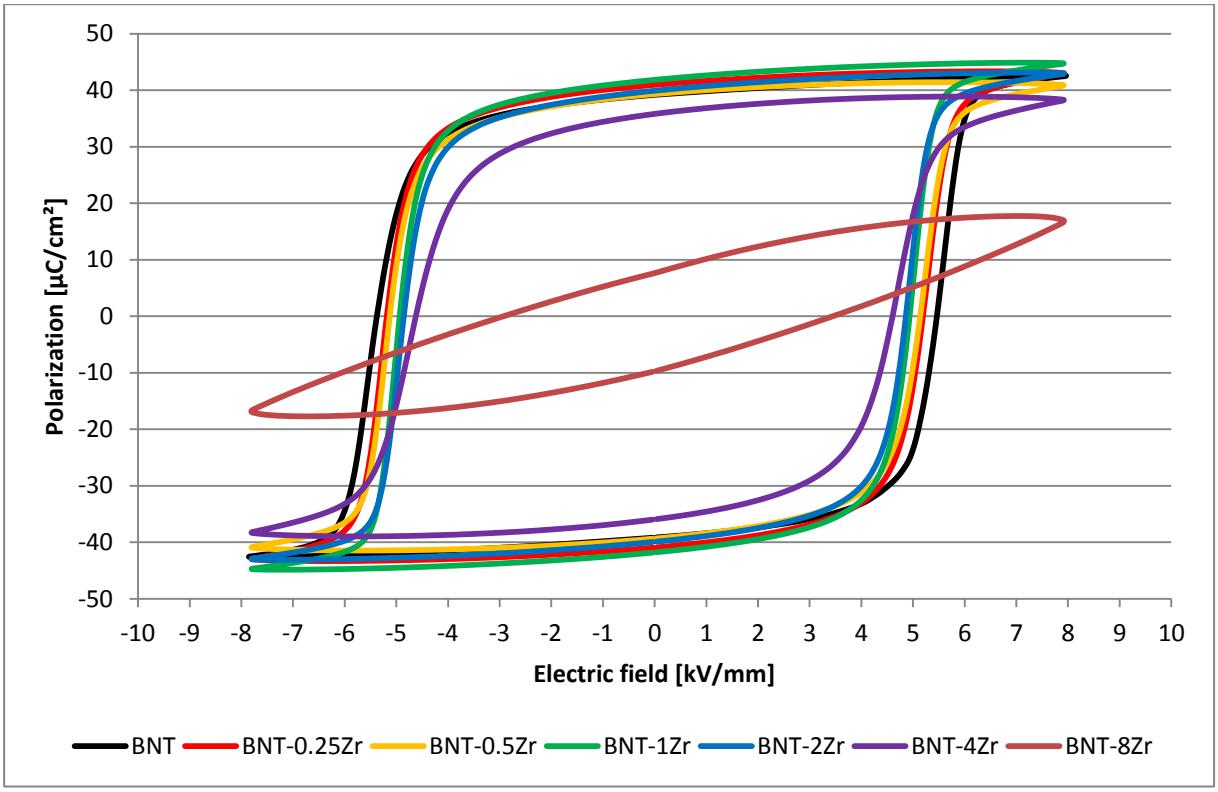


Figure 31: **Hysteresis loops of Zr-doped BNT.**

The influence of zirconium is very low at least at low doping levels. At 8 % zirconium concentration the hysteresis loop gets cigar-shaped, most certainly a result of the low applied electric field, which was not sufficient to reach saturation. Since the hysteresis loops up to 4 % zirconium almost exactly resemble the behavior of the tin doped samples, it is very likely, that the hysteresis loop for 8 % zirconium doping will also show a similar behavior to the hysteresis loop for 8 % tin. A major conclusion of this measurement is that the electron configuration has very little influence compared to the ionic radius.

Of the three doping agents that were used to substitute titanium on the B-site of the perovskite, zirconium has the largest ionic radius. It is almost 20 % larger than titanium and almost twice as heavy. Its influence should be comparable to tin, unless the d^{10}-configuration of tin has a major influence. The temperature dependence of the permittivity and the loss tangent (Figure 32) in combination with the hysteresis loops should clarify that.

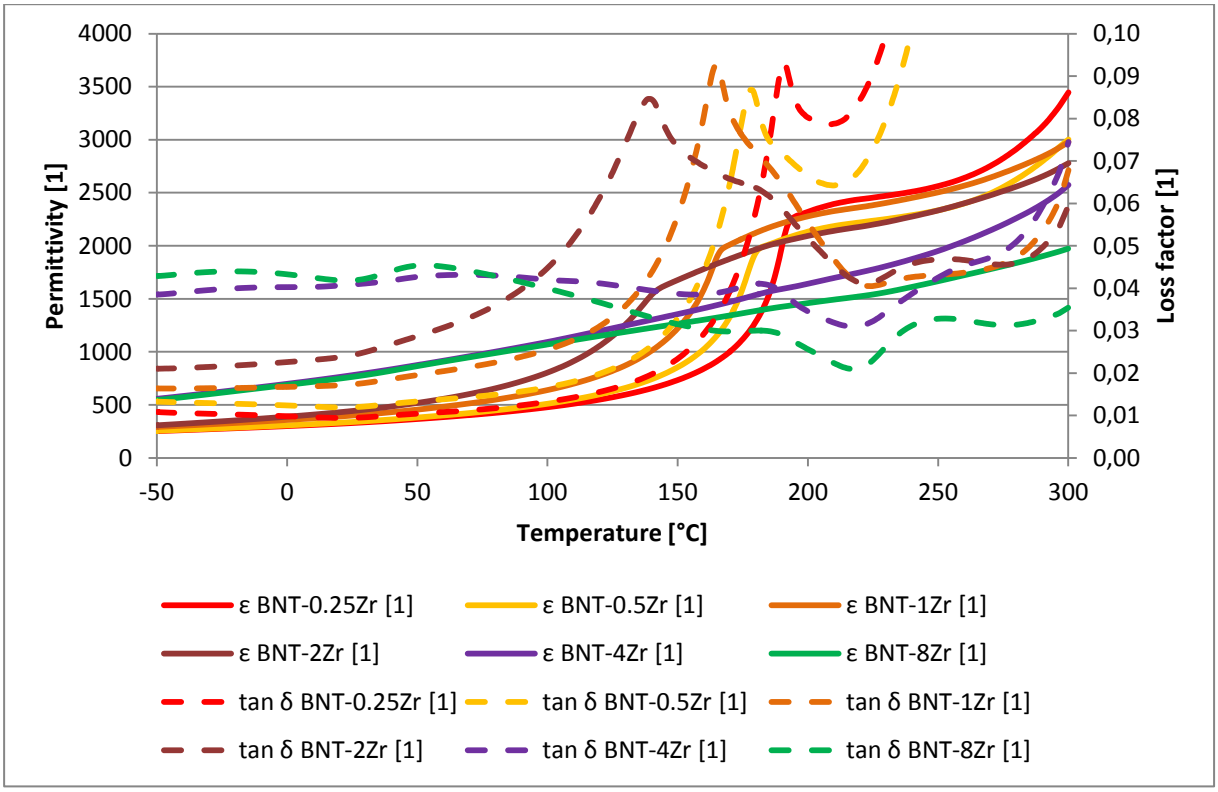


Figure 32: **Temperature dependence of permittivity and loss tangent in BNT-xZr.**

The influence of zirconium is almost exactly the same as tin. Titanium also reduces the depolarization temperature strongly, at 2 % doping, T_d is at 139 °C (BNT-2Sn: T_d = 140 °C). The samples BNT-4Zr and BNT-8Zr were obviously not poled prior to this small signal measurement, with BNT-8Zr being unable to be poled with our experimental setup. A comparison of the results of tin and zirconium doping comes to the conclusion, that both dopants have the exactly same influence which is simply caused by the larger ionic radius. There is no evidence, that the d^{10}-configuration of tin has an additional impact on the material. As a conclusion, tin and zirconium can be considered as equally strong doping agents in regard of lowering T_d.

4.3.7. Substitution of titanium with lithium / vanadium

This chapter describes the influence of a complex M^{4+}-ion, consisting of 0.25 Li^{+} and 0.75 V^{5+} (LV^{4+}) with a resulting radius of 0.595 Å which is slightly smaller than the radius of titanium on the material behavior. These experiments clarify if BNT can be modified with a complex B-site ion like $PbMg_{1/3}Nb_{2/3}O_3$ (PMN). The combination Li / V should have very little influence on the cell dimensions because of the similar radius to titanium; also the acceptor- and donor-effect should be compensated and have no impact on the defect concentration. The material is theoretically free of vacancies.

The XRD-patterns shown in Figure 33 have, with the exception of BNT-8BNLV, very little deviation. The reflex positions stay virtually the same; 8BNLV shows a hint of a secondary phase reflection. At low concentrations, the complex ion Li^{+} / V^{5+} seems to perfectly fit into the lattice.

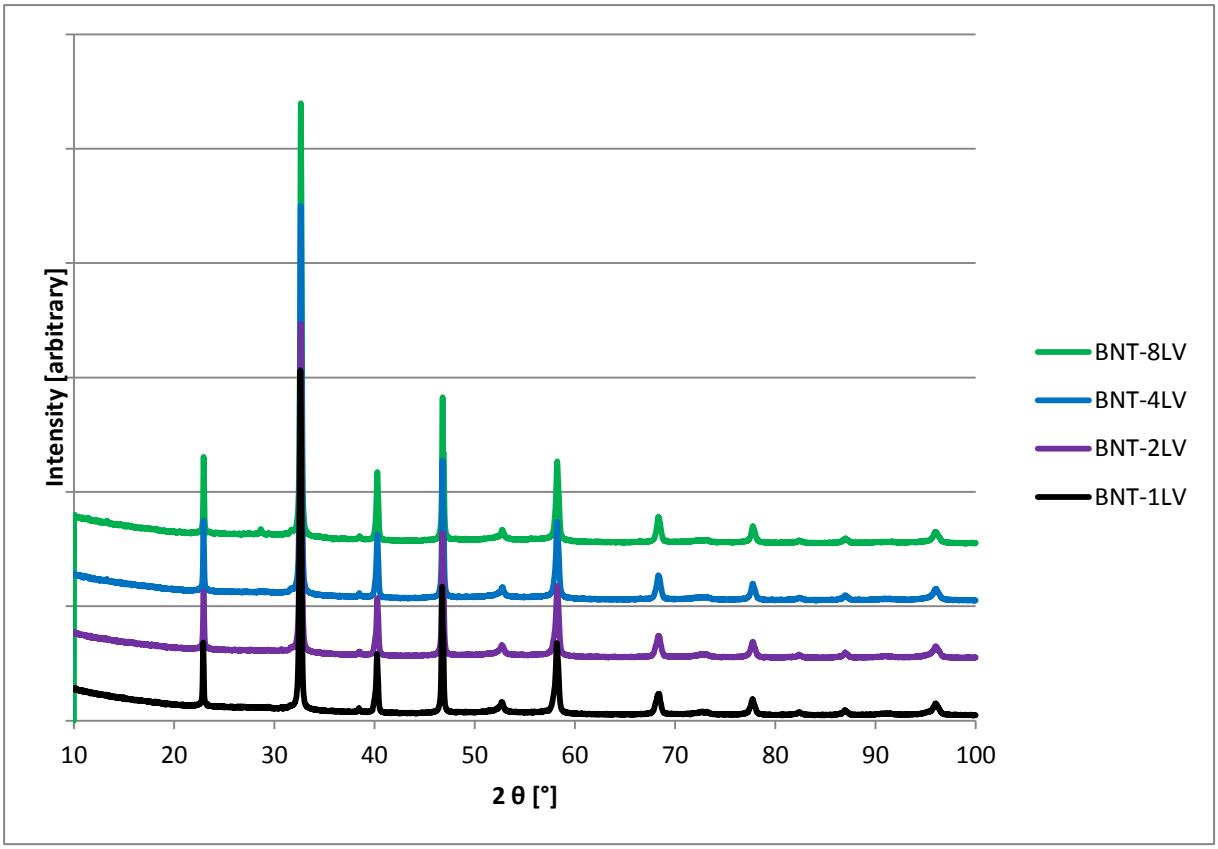


Figure 33: XRD patterns of Ti-substituted BNT with a compensated lithium / vanadium mixture.

The values in Table 13 summarize the results from XRD. The cell volume changes slightly with the amount of dopant, a trend to smaller cell volumes can be found. The spike at 2 % LV can have been caused by sample treatment and is of little concern. Because of the lithium content in the material, the secondary phase inclusions promoting at high LV concentrations are not analyzable using EDX, evaluation of the XRD data gives no clear result.

Table 13: Comparison of the cell volume of BNT and LV doped materials.

	BNT-1LV	BNT-2LV	BNT-4LV	BNT-9LV
Cell volume [Å³]	351.7195	351.8306	351.6280	351.6056

The little change of the lattice parameters caused by the similar radius and the combined molar mass of LV of 39.94 g/mol which is close to the molar mass of titanium leave no expectations for big differences in the hysteresis loops (Figure 34).

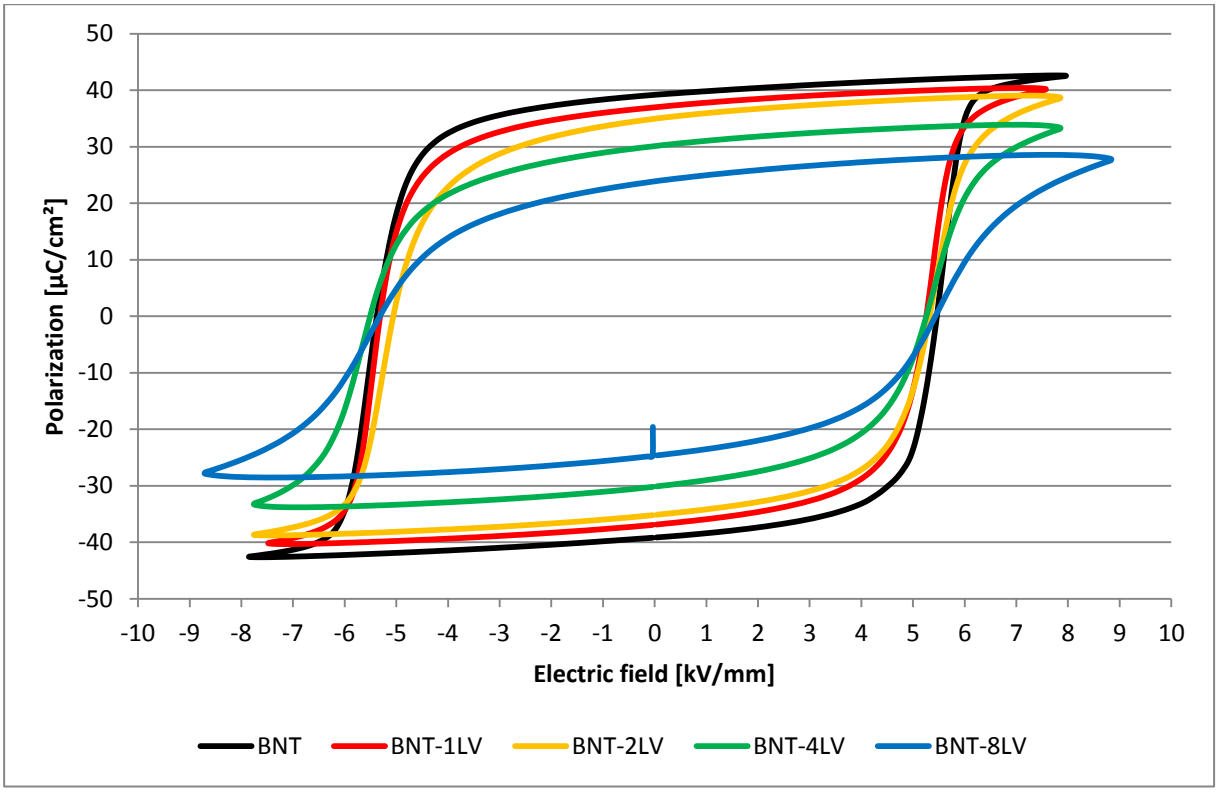


Figure 34: **Hysteresis loops of Li / V-doped BNT.**

The influence of LV is comparable to the impact of germanium on BNT, but far less pronounced. The composition BNT-8Ge (Figure 25 in chapter 4.3.4) has a maximum polarization of 21.8 µC/cm², compared to BNT-8LV with 28.4 µC/cm². The influences of germanium and lithium / vanadium can be directly compared, with germanium being far more potent as a dopant because of its larger deviation of the ionic radius of titanium. LV does not influence sintering, even at 8 % doping, the sintering behavior matches BNT. Since the influence is limited to lower the maximum polarization, LV is not considered as a dopant in later experiments.

4.3.8. Substitution of titanium with lithium / tungsten

Doping with Li^+ / W^{6+} follows the same concept as doping with LV. Both ions form a complex B-site ion LW^{4+} consisting of 0.4 lithium and 0.6 tungsten. This combination is again free of vacancies; the acceptor- and donor-properties compensate each other.

The resulting ionic radius of LW is 0.664 Å and about 10 % larger than the radius of titanium. Regarding the previous result with elements substituting titanium, a material behavior comparable to BNT-xSn or BNT-xZr should be expected. The XRD-patterns in Figure 35 draw a different picture.

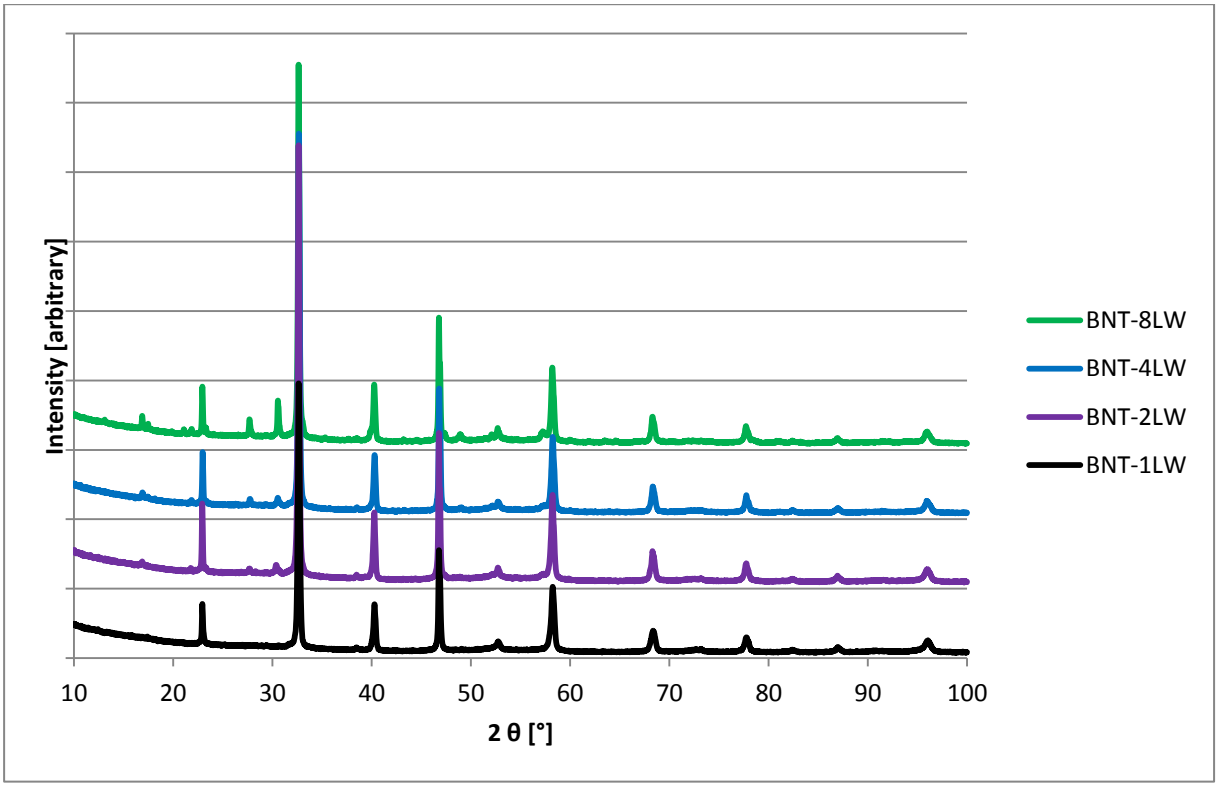


Figure 35: XRD patterns of Ti-substituted BNT with a compensated lithium / tungsten mixture.

The prepared samples exhibit the formation of a secondary phase, most likely $Bi_2Ti_2O_7$, already at 1 % titanium substitution. The cell volume (Table 14) grows slightly with higher LW content. This is caused again by the larger ionic radius of the complex LW ion.

Table 14: Comparison of the cell volume of BNT and LW doped materials.

	BNT-1LW	BNT-2LW	BNT-4LW	BNT-8LW
Cell volume [Å³]	351.7925	351.6537	351.9621	351.9460

The decomposition of BNT-xLW causes unknown defect chemistry in the material. Since $Bi_2Ti_2O_7$ contains A- and B-site ions, the composition of the matrix cannot be predicted. Another complicating issue, next to the impossible EDX analysis of lithium containing material, is that lithium can also occupy the A-site of the material. If the secondary phase formation reaction in BNT-xLW moves lithium from the B- to the A-site of the perovskite, an A-site acceptor-doped material is formed. The hysteresis loops (Figure 35) quite conforms this behavior.

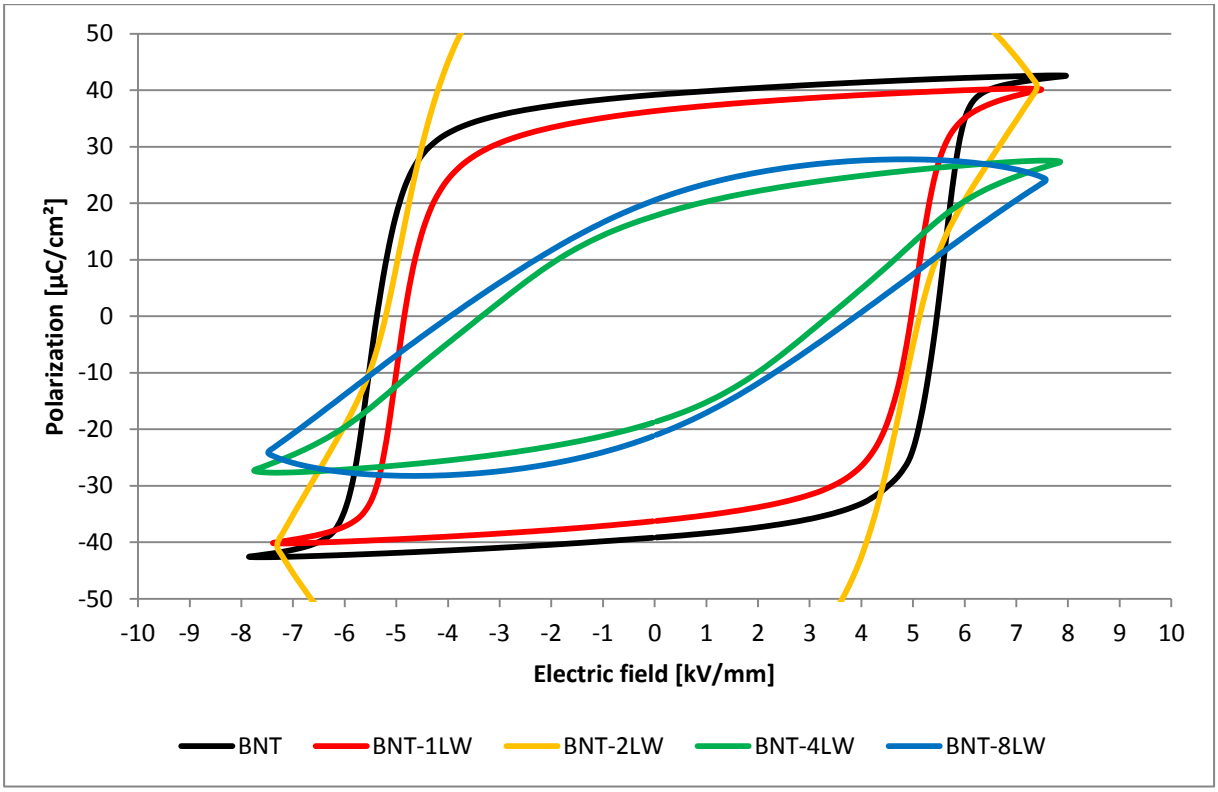


Figure 36: **Hysteresis loops of Li / W-doped BNT.**

The hysteresis loops can easily be divided in three sections: low (≤ 1 % LW), medium (2 % LW) and high (≥ 4 %LW) content. At low dopant concentration, the hysteresis loop stays mainly unchanged. High doping contents show a cigar shaped hysteresis loop, which is very hard to saturate. This behavior is quite common in decomposition afflicted materials. Medium dopant concentrations show very little secondary phase reflections in the XRD-pattern but a very lossy hysteresis loop. At this point, the decomposition reaction of BNT-1LW to $Bi_2Ti_2O_7$ moves the remaining lithium form the B-site to the A-site and produces an acceptor-doped material.

The sintering behavior is also afflicted to the worse by LW doping. The material needs temperatures > 1100 °C to produce dense samples, combined with the inferior electrical performance, LW is not further used in following experiments.

4.4.Solid solutions of BNT with other compounds

In this chapter, the results of solid solutions containing BNT and compounds with the formula $A^{2+}B^{4+}O_3$ (A = Ca, Mg; B = Ge, Sn, Zr) are discussed. The compounds BNT-xCT and BNT-xMT can be considered key compositions; the properties of the other compound can be deduced by combining those results with the results of BNT-xGe, BNT-xSn and BNT-xZr of the previous chapter.

4.4.1. Solid solution of BNT and CT

$CaTiO_3$ (CT) is the naming compound for the perovskite structure. In this work, it is used to form solid solutions with BNT. CT is not ferroelectric at room temperature, but earlier works cited in section 2.6 show the positive influence of CT on BNT, regarding its temperature levels.

In BNT, with its complex A-site ion consisting of 0.5 Bi^{3+} and 0.5 Na^{+}, calcium can also be looked at as a single element doping, substituting said complex ion. For more clarity regarding the following chapters, the result of this substitution is looked at as a solid solution of BNT and CT.

The ionic radius of calcium is slightly smaller than the combined radius of bismuth and sodium, the main structural effect should be shrinkage of the unit cell. The XRD-patterns in Figure 37 show a small shift of the reflections to larger angles and no evidence for a possible secondary phase.

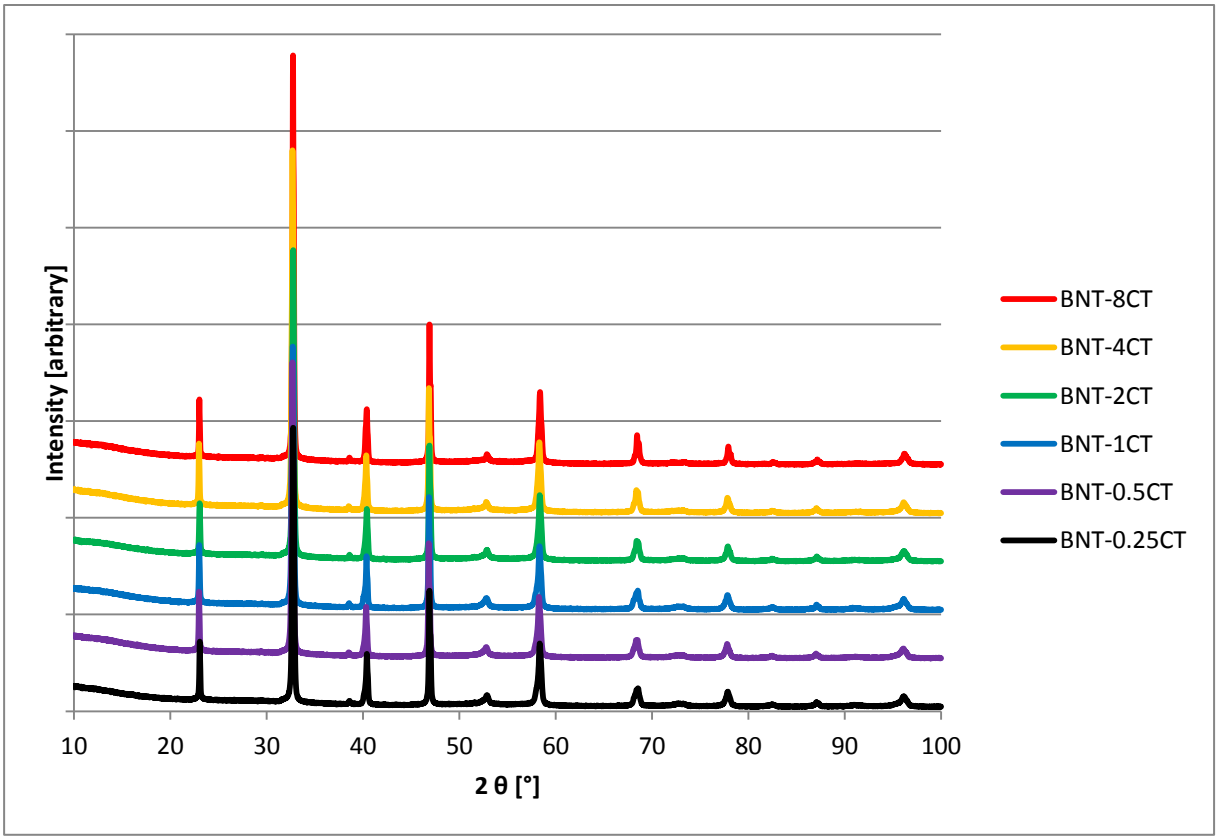


Figure 37: XRD-patterns of BNT-xCT solid solutions.

The before mentioned shift of the reflections to larger angles is a result of the smaller volume of the unit cell, caused by the incorporation of calcium. The findings of the cell volume and the grain size of the sintered ceramics are shown in Table 15.

Table 15: Comparison of the cell volume and grain size of BNT-xCT solid solutions.

	BNT-0.25CT	BNT-0.5CT	BNT-1CT	BNT-2CT	BNT-4CT	BNT-8CT
Grain size [µm]	3.4	7.6	8.9	5.0	3.6	4.3
Cell volume [Å³]	352.0431	351.9728	351.8197	351.5398	350.8204	350.2344

The cell volume nicely follows the trend to smaller volumes at higher doping contents. Calcium is obviously incorporated into BNT; there is no hint of miscibility problems. Sintering of the samples is also not influenced; the disc-shaped samples are dense and show no sign of melting or porosity.

According to the literature, calcium has a strong influence on T_d, lowering the depolarization temperature drastically without lowering T_m. In the room temperature hysteresis loops (Figure 38), this behavior could not be found, the polarization loops differ very little from undoped BNT. A relaxor like BNT should show distinctly pinched hysteresis loops when the temperature approaches T_d.

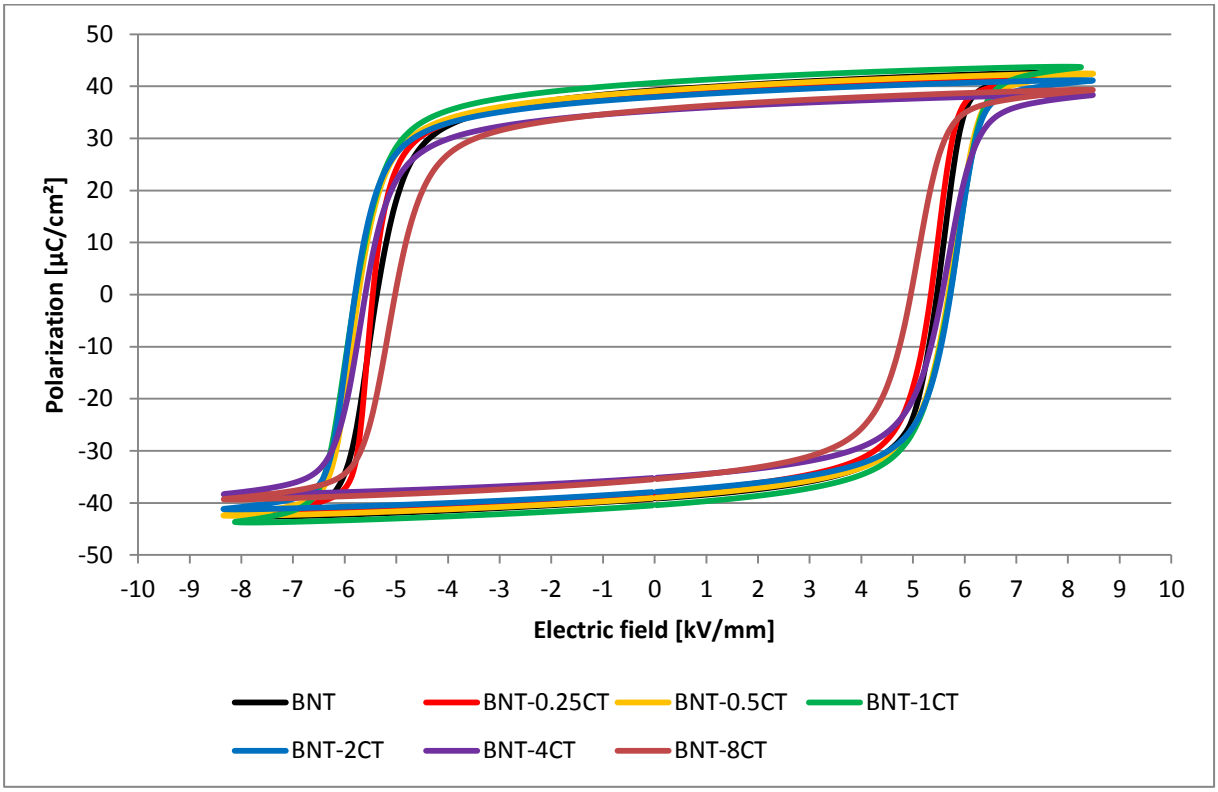


Figure 38: Hysteresis loops of solid solutions of BNT and CT.

The hysteresis loops in the Figure 38 show almost no deviation from BNT. There is no impact on E_c or P_r, P_{max} also can be considered constant. On one hand, the impact of CT on the hysteresis loops is quite disappointing, having no influence at all. On the other hand, the maximum polarization of BNT is retained, despite the addition of a non-ferroelectric material.

The temperature dependant measurements (Figure 39) clearly show the impact of CT in BNT. CT not only lowers the depolarization temperature, but also makes every single transition point very diffuse. The hysteresis loops in Figure 38 would look very different at elevated temperatures. Due to the high diffusivity of the transitions, a T_d or a relation of T_d-shift and CT concentration cannot be given.

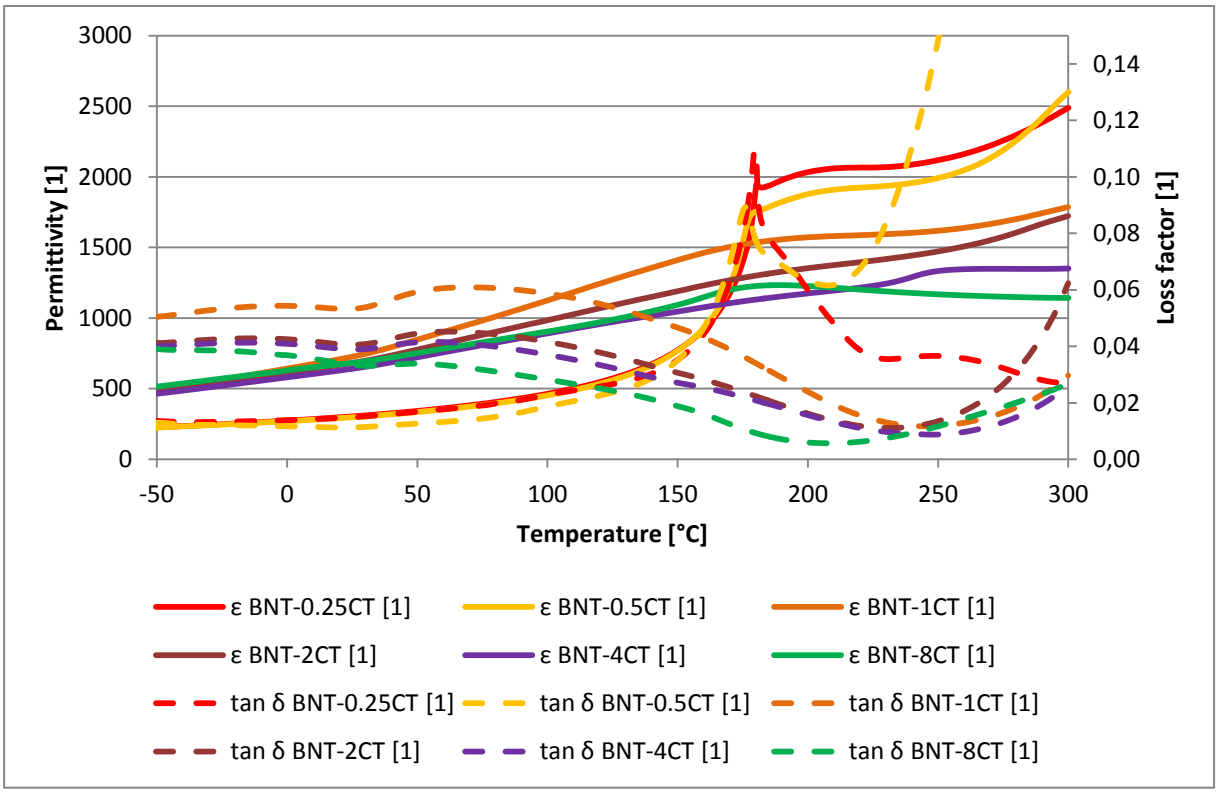


Figure 39: **Temperature dependence of permittivity and loss tangent in BNT-xCT.**

The diffusivity of the transitions can be very useful in a possible application, since the small signal parameters become much more stable in a broad temperature range. BNT-xCT with $x \geq 1$ shows no distinct transition point from the ferroelectric to the antiferroelectric or nonpolar phase anymore. Samples with less CT content have a nice and sharp transition point at 179 °C, which is higher than the transition in BNT, taking place at 161 °C.

The addition of a third A-site ion promotes very diffuse transitions at higher dopant concentrations (≥ 1 % CT). Sintering is not affected by the CT-content, said diffusivity can be usable to lower the

temperature dependence of the material. The impact of the CT addition is very high, changing the temperature response of the material already at 1 % addition. CT can therefore be considered a very potent dopant.

4.4.2. Solid solution of BNT and CG

The addition of CG to BNT should basically have parameters that can be combined from the findings in chapter 4.3.4 and chapter 4.4.1. Germanium substituted BNT shows a lower T_d in relation to the doping concentration, calcium doping using CT also lowers T_d and introduces diffuse transitions. Both doping agents act similar, so the effect of CG should be stronger than the single effects of germanium and calcium doping. The polarization loops (Figure 40) confirm this assumption.

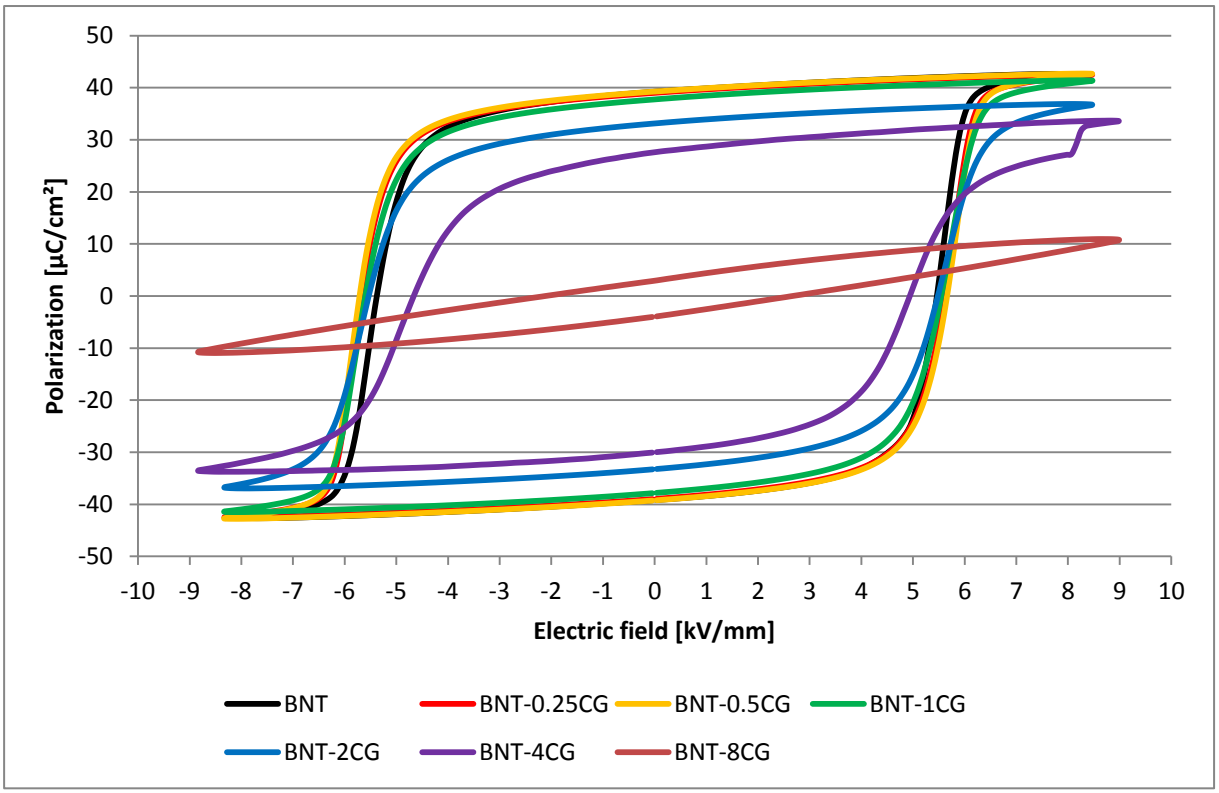


Figure 40: Hysteresis loops of solid solutions of BNT and CG.

The hysteresis loops show the combined behavior of germanium and calcium doping. The maximum polarization drops with higher doping contents, which is a feature of the germanium doped samples. The needed field to reach saturation also rises with higher germanium content. The impact of both dopants on T_d leads to a nonpolar hysteresis loop for BNT-8CG; the measurement temperature is obviously in the antiferroelectric / nonpolar temperature regime which leads to this cigar shaped loop. The sintering behavior of the samples is also very alike to the germanium doped samples, showing poor densification in almost molten discs.

4.4.3. Solid solution of BNT and CS

The solid solution of BNT and CS is a very promising candidate in regard of high impact on the polarization loops. Both tin (chapter 2.5.5) and calcium (chapter 2.6.1) shift the depolarization temperature to lower temperatures without strongly reducing the maximum polarization. The influence of tin is much stronger compared to calcium, as the hysteresis loops of the respective chapters show. The combination of both doping agents in BNT-xCS leads to very interesting material parameters (Figure 41).

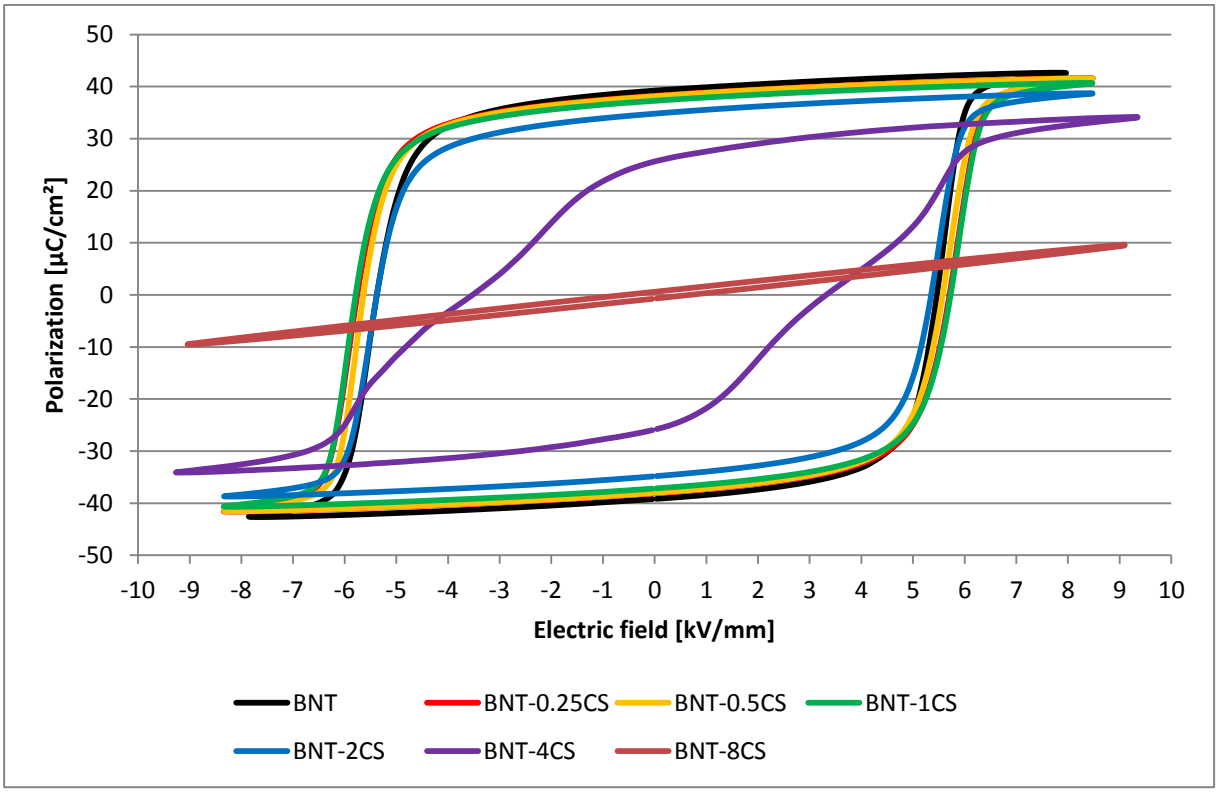


Figure 41: **Hysteresis loops of solid solutions of BNT and CS.**

Up to concentrations of 2 % CS, the hysteresis loops are almost congruent. In the case of tin doping, the first visible influence was at 4 % tin. Calcium doping with CT did not show any influence over the whole concentration range at room temperature measurements.

The impact of both tin and calcium doping revealed at the temperature dependent measurements, where big shifts of T_d were observed. In the case of BNT-xCS, the effects of tin and calcium doping add up, which results in a much more potent doping agent. The hysteresis loop of BNT-4CS resembles the shape of BNT-8CS with only half the dopant concentration. At a doping level of 8 %, the applied field is below the needed field for saturation, the hysteresis loop looks paraelectric.

The combination of tin and calcium leads to a very powerful doping system without any influences on the densification behavior. Its impact on BNT at room temperature is higher than in any other modifications studied before (except BNT-25BKT). The low amount of needed dopant reduces the risk of secondary phase formation caused by side reactions between the ingredients.

4.4.4. Solid solution of BNT and CZ

BNT-CZ is the combination of zirconium and calcium doped BNT and also a very promising candidate for favorable properties. The results of tin (chapter 4.3.5) and zirconium (chapter 4.3.6) doping show very similar impacts on BNT, the difference is almost indistinguishable. The hysteresis loops in Figure 42 also show a behavior which is very much alike.

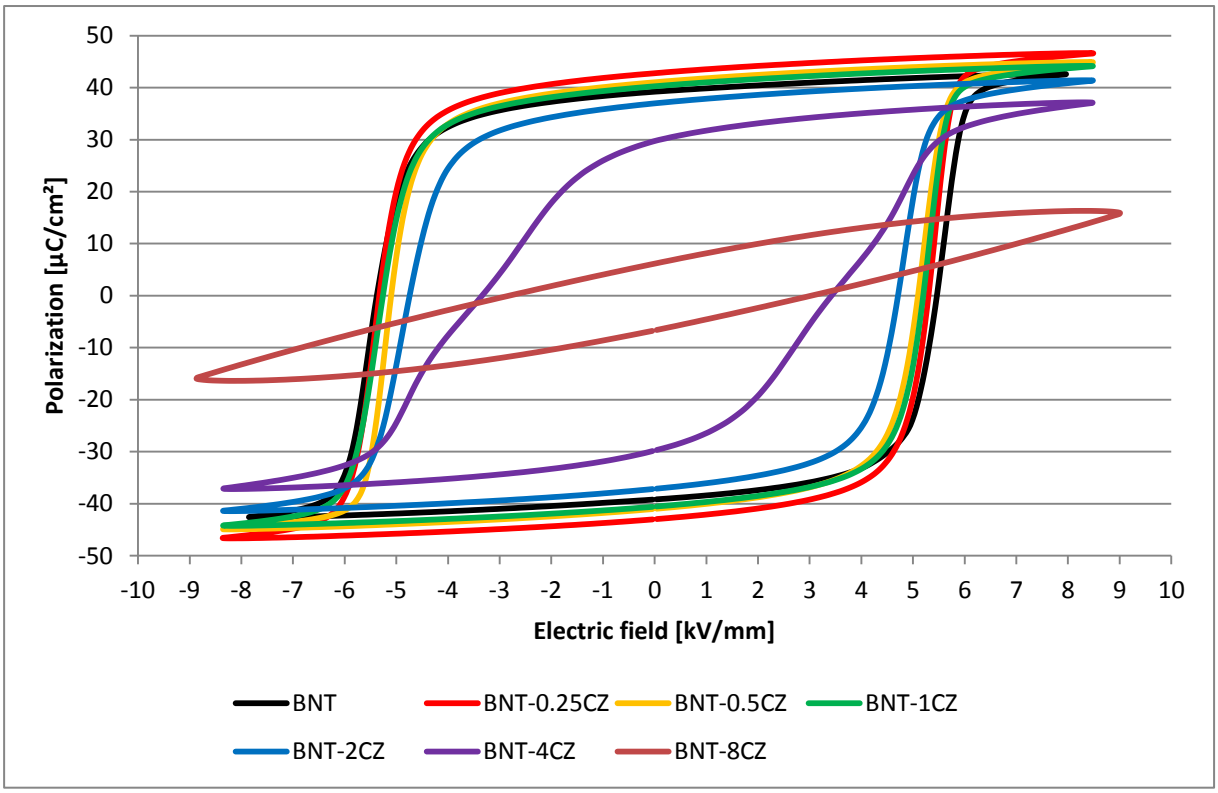


Figure 42: Hysteresis loops of solid solutions of BNT and CZ.

Like before, in the case of CS doping, the hysteresis loops of CZ doped BNT sum up the impact of zirconium and calcium on BNT. Below 4 % CZ, the influence on the room temperature hysteresis is very limited, at 4 % CZ content, the shape of the hysteresis loop changes drastically to a significantly softer loop. At 8 % CZ doping the applied field was not sufficient to reach saturation.

The comparison of CS and CZ shows that the influence of the d^{10}-electron configuration is limited and the modification of the material behavior is much stronger influenced by the ionic radius. Compared to single tin and zirconium doped materials, the influence of tin in a solid solution like CS on the

material is higher than the influence of CZ. The CZ doped samples suffered from electrical breakdown during the hysteresis loop measurements despite good densities. This point and the higher influence make CS the superior doping agent for BNT.

4.4.5. Solid solution of BNT and MT

$MgTiO_3$ or abbreviated MT is a possibility to introduce Mg^{2+} on the A-site of the perovskite structure of BNT. Compared to CT, MT does not crystallize in a perovskite structure which is caused by the small ionic radius of magnesium. As mentioned in chapter 2.6.5, magnesium can also occupy the B-site of the perovskite and therefore can cause problems regarding the ratio between A and B-site occupation and continuative defect chemistry.

The reason magnesium is used in this work is its small radius. Literature data[28] and the results of the previous chapters show a strong correlation between ionic radius and the influence on the transition temperatures.

The XRD-patterns in Figure 43 show no noticeable shifts of the reflection positions but some reflection which can be caused by a secondary phase in BNT-8MT.

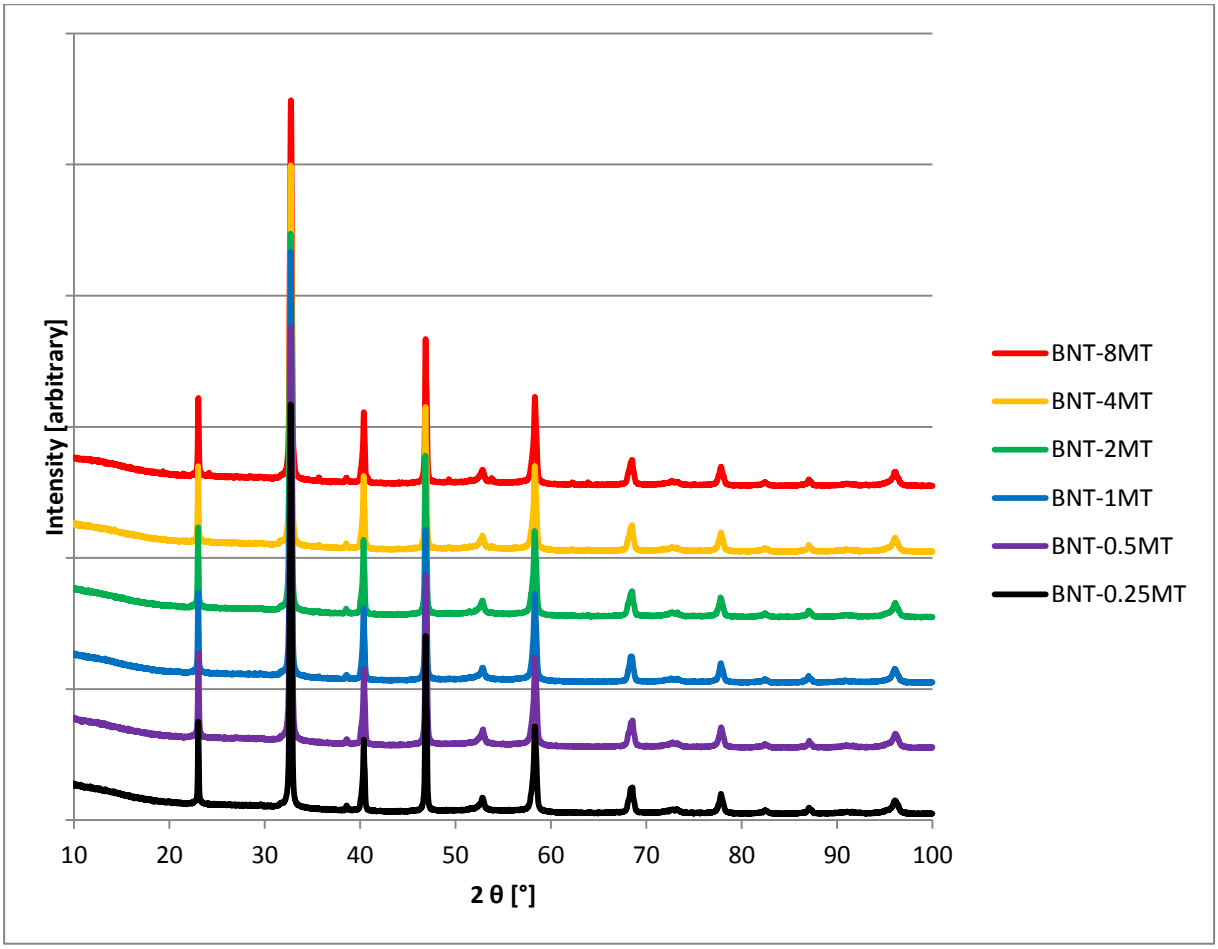


Figure 43: XRD-patterns of BNT-xMT solid solutions.

The lack of shift of the reflection positions is a strong indication that magnesium is not completely inserted into the BNT lattice. The absence of easily visible secondary phase reflections can be caused by many circumstances like amorphous structures, overlap of reflections or small reflection yields. The grain size and the cell volume are shown in Table 16.

Table 16: Comparison of the cell volume and the grain size of BNT-xMT solid solutions.

	BNT-0.25MT	BNT-0.5MT	BNT-1MT	BNT-2MT	BNT-4MT	BNT-8MT
Grain size [µm]	7.0	7.0	8.9	2.7	2.9	4.0
Cell volume [Å]	352.0587	352.0473	352.1743	352.1002	352.2625	352.3868

The reduction of the cell volume is the result of magnesium being inserted on the B-site of the material which starts at concentrations > 0.5 % MT. Up to 0.5 % MT, the cell volume drops because the ionic radius in 12-fold coordination of magnesium (1.20 Å) is smaller than the average radius of bismuth (1.45 Å) and sodium (1.39 Å). At concentrations > 0.5 % MT, the cell volume grows because the radius in 6-fold coordination of magnesium (0.72 Å) is larger than the radius of

titanium (0.605 Å). The reaction shown in Equation 14 shows the migration of magnesium to the B-site of the structure.

Equation 14: **Migration reaction of magnesium from A- to B-site of the perovskite.**

Magnesium acts as an acceptor on the B-site, the reaction of the material to maintain electro neutrality is the formation of oxygen vacancies. Oxygen vacancies are very mobile and contribute to conductivity, especially at elevated temperatures.

The hysteresis loops in Figure 44 show no influences of conductivity caused by oxygen vacancies. The different compositions show very little deviation and similar behavior like BNT doped with CT.

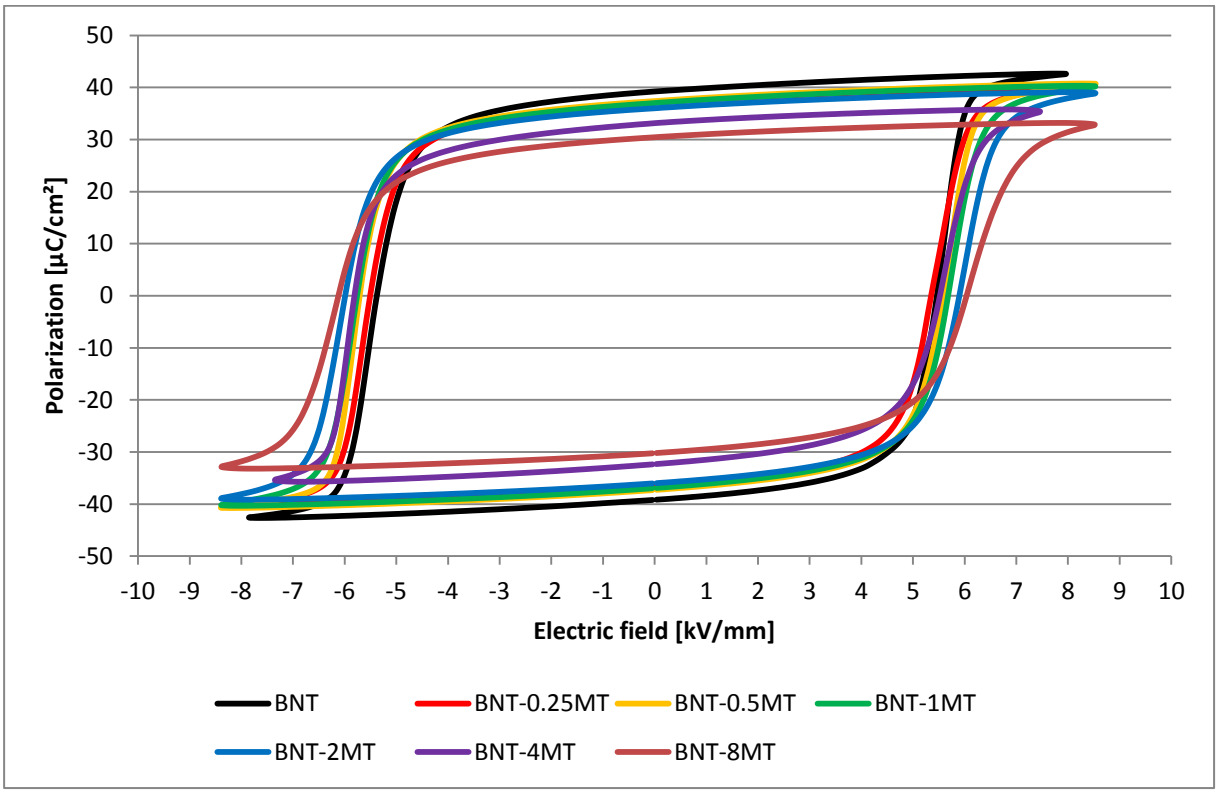


Figure 44: **Hysteresis loops of solid solutions of BNT and MT.**

An exception to the statement above is the composition BNT-8MT, which has a significantly lower maximum polarization than the other compositions. This is caused by the electrically inactive secondary phase TiO_2. The general properties of the hysteresis loops stay relatively unchanged to BNT. Since the ionic radius of magnesium is very low, a higher impact had been anticipated.

The temperature dependence of the permittivity and the loss factor shown in Figure 45 displays a very different behavior to the compositions discussed before.

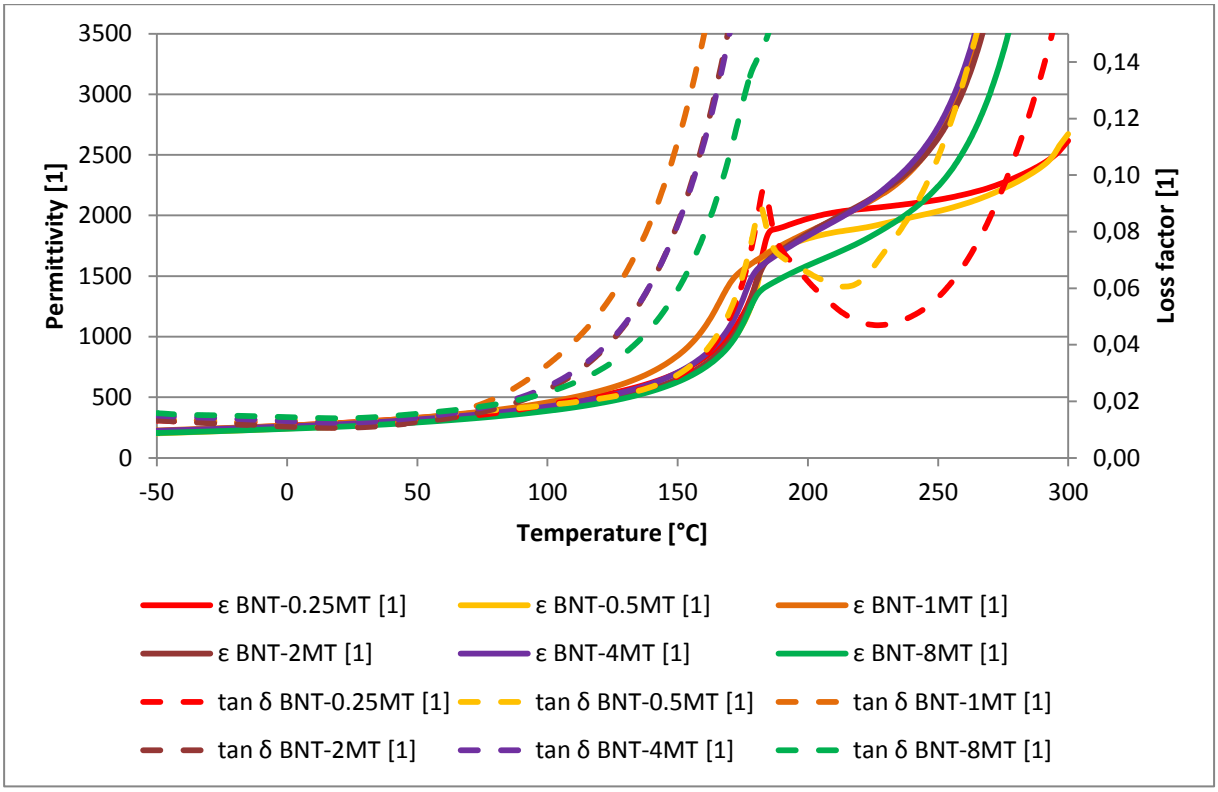


Figure 45: **Temperature dependence of permitivitty and loss tangent in BNT-xMT.**

The temperature dependence shows two very different responses of the various compositions. At MT concentrations ≤ 0.5 % both the permittivity and the loss tangent show a "BNT-like" behavior, with a distinct maximum of the loss tangent at T_d. At temperatures > T_d, the introduction of magnesium seems to lower T_m or, more likely, the material gets conductive due to oxygen vacancies. Compound with a magnesium content > 0.5 % have huge losses at temperatures > 150 °C combined with unaffected hysteresis loops at room temperature. Since there is no evidence of a decomposition reaction visible in the XRD-patterns or the microstructure, this behavior can only be the result of oxygen vacancies, caused by the migration of magnesium from the A-site to the B-site of the perovskite.

The overall performance of magnesium as a dopant is disappointing. It has no visible influence on the material behavior at room temperature, the introduction of oxygen vacancies leads to very high losses caused by conductivity at temperatures > 150 °C. At least sintering is not affected by magnesium doping. Due to the worsened properties, MT is not considered as a possible dopant for a prototype material.

4.4.6. Solid solution of BNT and MG

The combination magnesium and germanium (MG) as a dopant for BNT is used to introduce the changes caused by both elements into the material. As described in previous chapters, magnesium and germanium do not change the parameters of BNT in a favorable way. Germanium doping has a certain influence on T_d, unfortunately it hinders sintering and reduces the maximum polarization. Magnesium has very low influence at room temperature, but makes the ceramic conducting at higher doping levels and temperatures > 150 °C.

MG also does not crystallize as a perovskite, but since both ions have very small ionic radii, the introduction of both at the same time could lead to a better solubility of both elements in the structure. The hysteresis loops measured at room temperature (Figure 46) show almost the same behavior as BNT doped with germanium.

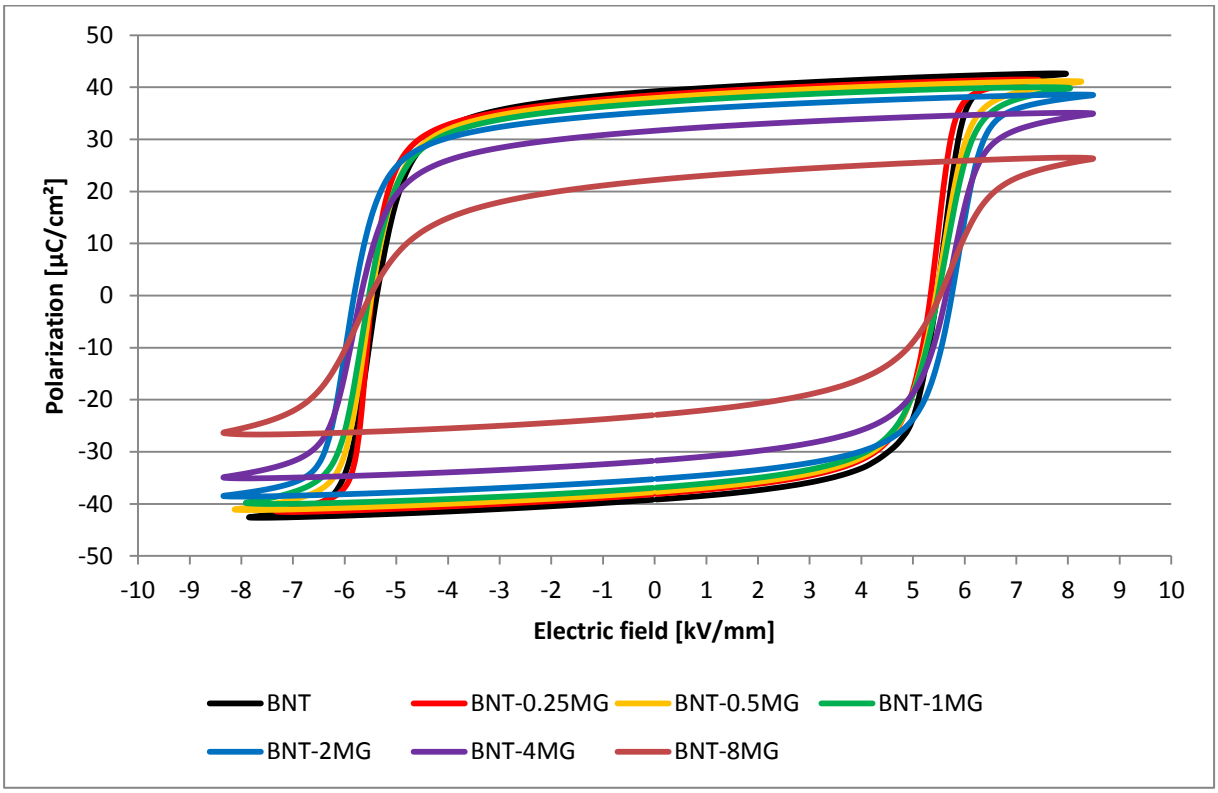


Figure 46: Hysteresis loops of solid solutions of BNT and MG.

At room temperature, the influence of CG doping is exactly the same as single germanium doping. The shift of the depolarization temperature T_d is not sufficient to reach the antiferroelectric / nonpolar phase at room temperature. Also, the addition of germanium worsens the sintering behavior in the known way; leading to partially molten samples with low densities.

4.4.7. Solid solution of BNT and MS

Doping with tin has delivered very good results; this chapter discusses the influence of tin and magnesium on the electrical parameters. Like the other magnesium compounds, MS does not crystallize as a perovskite, so the same problems as before can be anticipated. The hysteresis loops (Figure 47) show little differences compared to pure tin doping described in chapter 4.3.5.

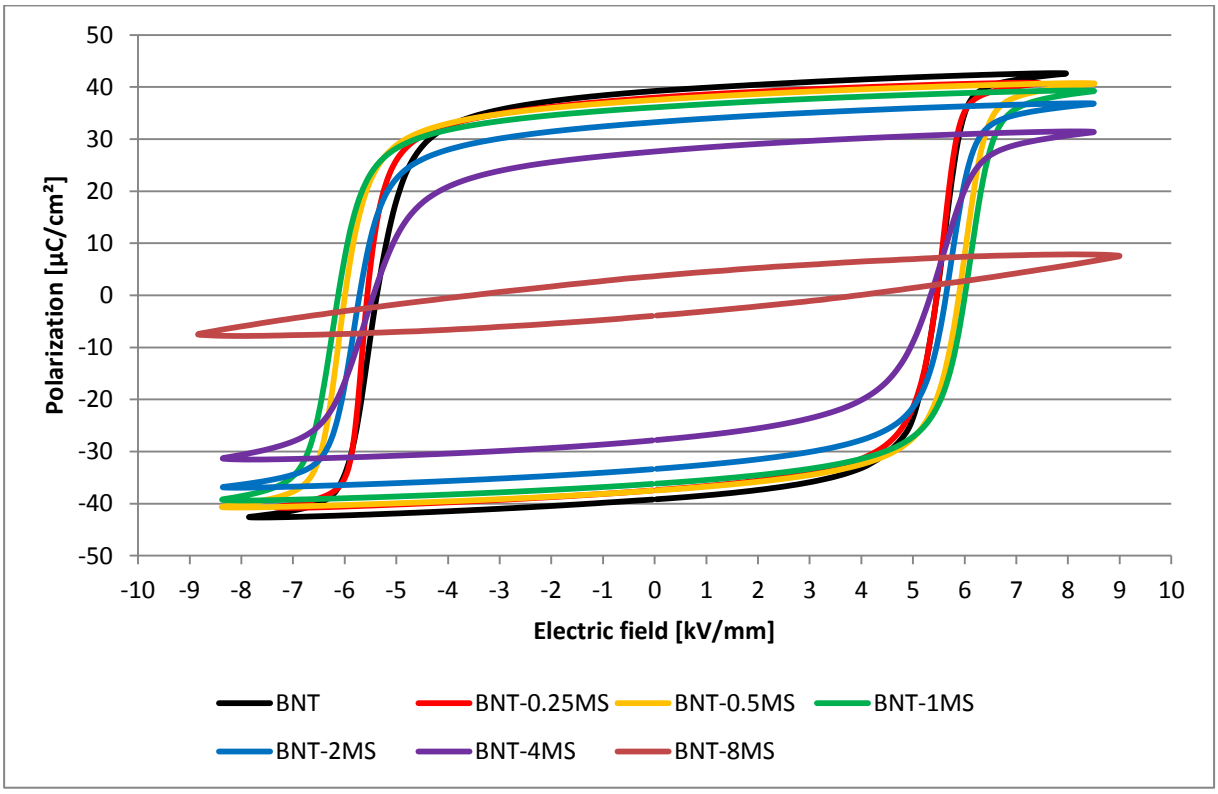


Figure 47: Hysteresis loops of solid solutions of BNT and MS.

The only visible difference between the polarization loops of BNT-xMS and BNT-xSn can be found in the case of 8 % doping. The hysteresis loop of BNT-8Sn is pinched and shows a maximum polarization while BNT-8MS does not. The reason for this behavior is the magnitude of the electric field which was 10 kV/mm for BNT-8Sn but only 9 kV/mm for BNT-8MS. The addition of MS to BNT also seems to hinder sintering because no sample BNT-8MS could withstand 10 kV/mm without suffering electrical breakdown.

4.4.8. Solid solution of BNT and MZ

The last composition of interest is BNT doped with MZ. MZ has the biggest impact on the Goldschmidt tolerance factor since it combines the smallest A-site with the biggest B-site ion. However, previous chapters show, that the position of magnesium in the lattice is not as exactly determined as wished. The influence of the doping agent MZ is shown in Figure 48.

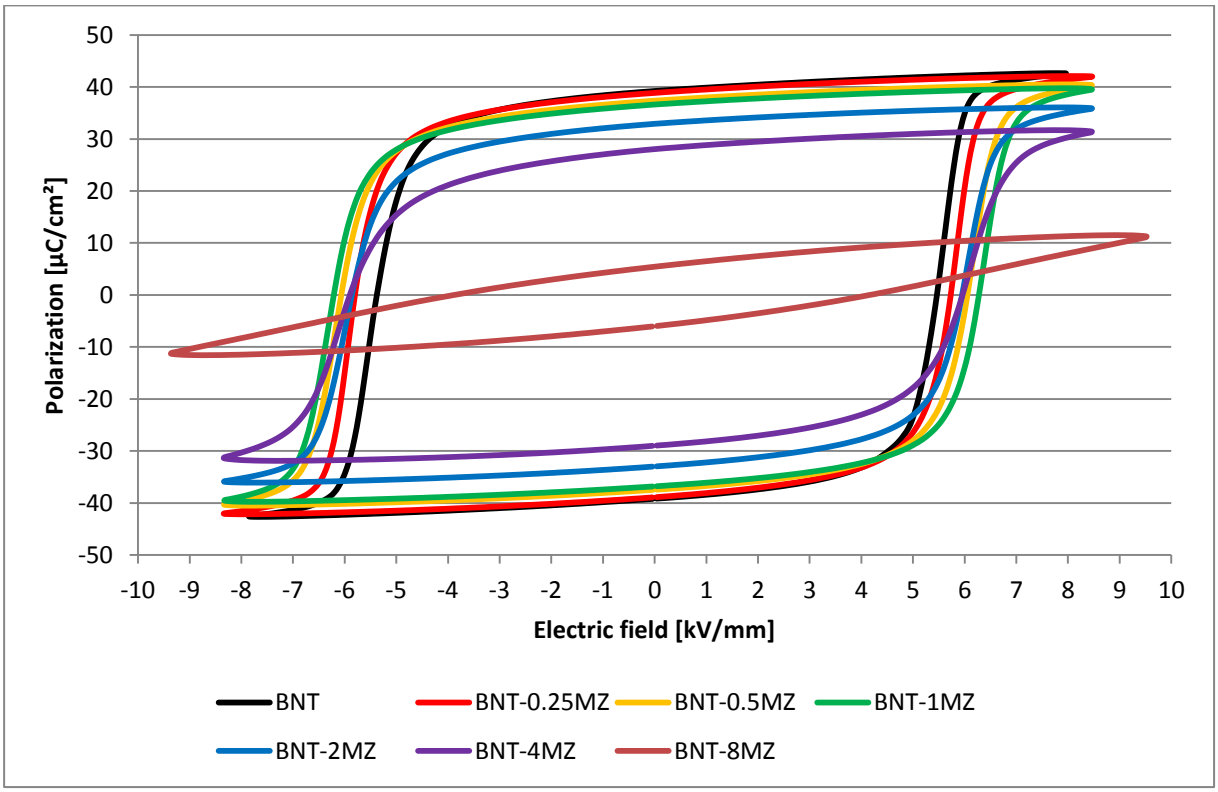


Figure 48: Hysteresis loops of solid solutions of BNT and MZ.

Like in the case of MS doping, the materials doped with MZ and only zirconium can hardly be distinguished. The combined influence of magnesium and zirconium is too low to push T_d below room temperature. Also, with more different elements, more possible reactions can take place after and during the migration of magnesium to the B-site. The results of this chapter do not qualify MZ as a desired doping agent for BNT.

4.5.Summary of findings

The doping methods in BNT are various, as the previous chapters show. The parameters of BNT can be strongly altered with doping, the impact on the transition temperature T_d, which is of certain interest, can be very large.

Donor doping with calcium, cerium and niobium has a very high impact on the hysteresis loops at room temperature, but it relies on the formation of vacancies. The results of donor doping show, that BNT only tolerates a very small vacancy concentration on either A- or B-site. High donor concentrations lead to the formation of secondary phase inclusions, which alter the stoichiometry of the matrix material.

The titanium substitutions using germanium, tin and zirconium do not create vacancies of any kind because they are isovalent to titanium. Germanium, being the smallest substituent, has an impact on T_d, shifting it to lower levels. The Goldschmidt tolerance factor rises with the amount of germanium doping. Doping with tin and zirconium also moves T_d to lower levels, since both substituents have larger ionic radii than titanium, the Goldschmidt tolerance factor decreases. Figure 49 shows the change of the depolarization temperature over the tolerance factor.

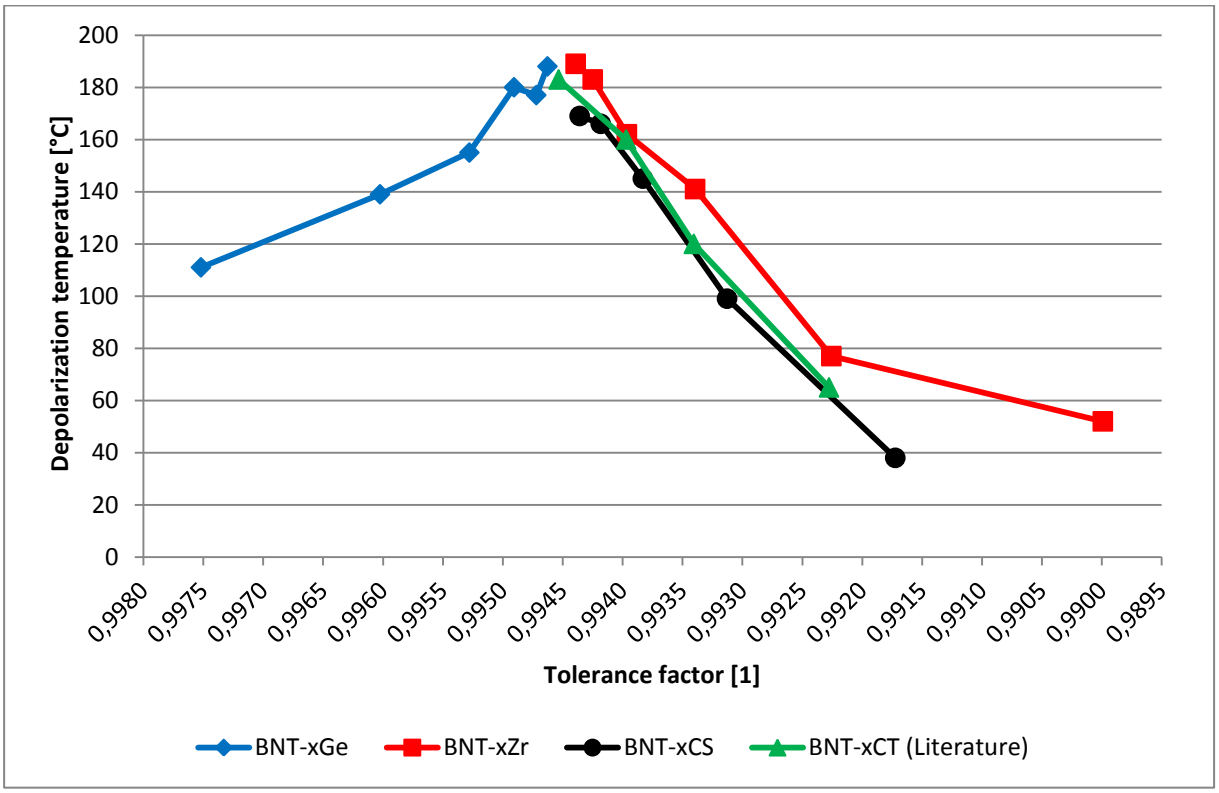


Figure 49: Development of T_d over the Goldschmidt tolerance factor derived from BNT-xGe and BNT-xZr.

The main conclusion taken from Figure 49 is that every deviation from the tolerance factor of BNT decreases T_d. B-site doping with germanium, shifting the tolerance actor to higher values, has a little less influence than zirconium, which lowers the tolerance factor. This model is also applicable for A-site doping, as the diagram shows. The green graph for BNT-xCT is taken from literature[27] and shows almost exactly the behavior as the red graph, which resembles the data of zirconium doped BNT. The black line shows BNT-xCS, which combines A- and B-site doping. Even this complex composition follows the rules introduced by BNT-xZr. The most right data point in the diagram was derived from BNT-8Zr, a material which was not fully poled during the high field measurement process. The deviation from the linear connected data points before can be attributed to the lack of complete poling.

The perovskite mixtures containing CT also show a very good influence on the electrical behavior of BNT. Unfortunately, CT as a single dopant is not effective enough to shift T_d to approximately room temperature at a maximum concentration of 8 %. The temperature level gets lower and more diffuse, but the needed dopant content is clearly above 8 %.

The compositions CS and CZ combine the effects of BNT-xSn, BNT-xZr and BNT-xCT. All of those dopants reduce T_d in a different way and the effects of A- and B-site doping add up. BNT-4CS has a similar room temperature hysteresis as BNT-8Sn, doubling the impact of the solely B-site dopant. The effect of BNT-xCZ is directly comparable to BNT-xCS, making the material changing property mostly a function of the ionic radius of the B-site ion. The electron configuration (Sn^{4+}: d^{10}; Zr^{4+}: d^0) may have a small impact as well, since BNT-xCS has lower remnant polarizations and lower coercive fields at equal doping concentrations compared to BNT-xCZ. The different perovskite solid solutions also introduce very diffuse phase transitions, a property that is very useful in this case, since sudden jumps of the permittivity or loss factor are repressed.

Other B-site dopants like lithium / vanadium and lithium / tungsten do not show favorable impacts on the electrical parameters or sintering, so they are not considered in the next chapter. The same argument is valid for all magnesium containing materials.

4.5.1. Combination of findings to a prototype material

The composition for a prototype material was determined using the results from previous chapters. Because of its superior properties in the undoped state, BNT-25BKT was chosen as a starting compound over BNT. The pinched hysteresis loop of BNT-25BKT already combines a very high maximum polarization with low coercive field and remnant polarization.

BNT-25BKT needs a sintering temperature of 1150 °C to produce sufficiently dense samples. In order to reduce this temperature, sodium and potassium were substituted with lithium. Lithium is known to reduce the sintering temperature of BNT, also it reduces T_d as a positive side effect[35]. Like magnesium, lithium is small enough to occupy the B-site of the perovskite, so the concentration of lithium is limited. In this work, a substitution of 10 % of the single charged A-site ions was chosen.

To reduce the depolarization temperature to very low levels, CS has been chosen as a modifying agent. In BNT, 4 % CS lead to a strongly pinched hysteresis loop, while doping with 8 % CS lead to an almost paraelectric hysteresis loop which did not recover even at high electric fields. An amount of 5 % CS is added to the proposed compound, giving it the following composition:

Equation 15: Composition of BNK25L10T-5CS, the prototype material.

This compound unites all previous findings in one structure, without any vacancies. The combination BNT-xCS did not show any secondary phase reflections in the XRD-pattern and is not prone to secondary phase formation. The sintering temperature of this material is reduced to 1100 °C, which reduces possible losses due to evaporation.

4.5.2. Detailed results, temperature dependant hysteresis loops

The combination of the materials discussed in the previous chapters changes BNT, consisting of four ions to a complex, heavy doped material with no less than eight different ions. Since different elements show different affinities to each other, every added element increases the probability of side reactions, leading to secondary phase inclusions. In the case of BNK25L10T-5CS, there are reflections in the XRD-pattern (Figure 50) at 25.3 ° and 32.9 °, which are most likely caused by impurities in the material.

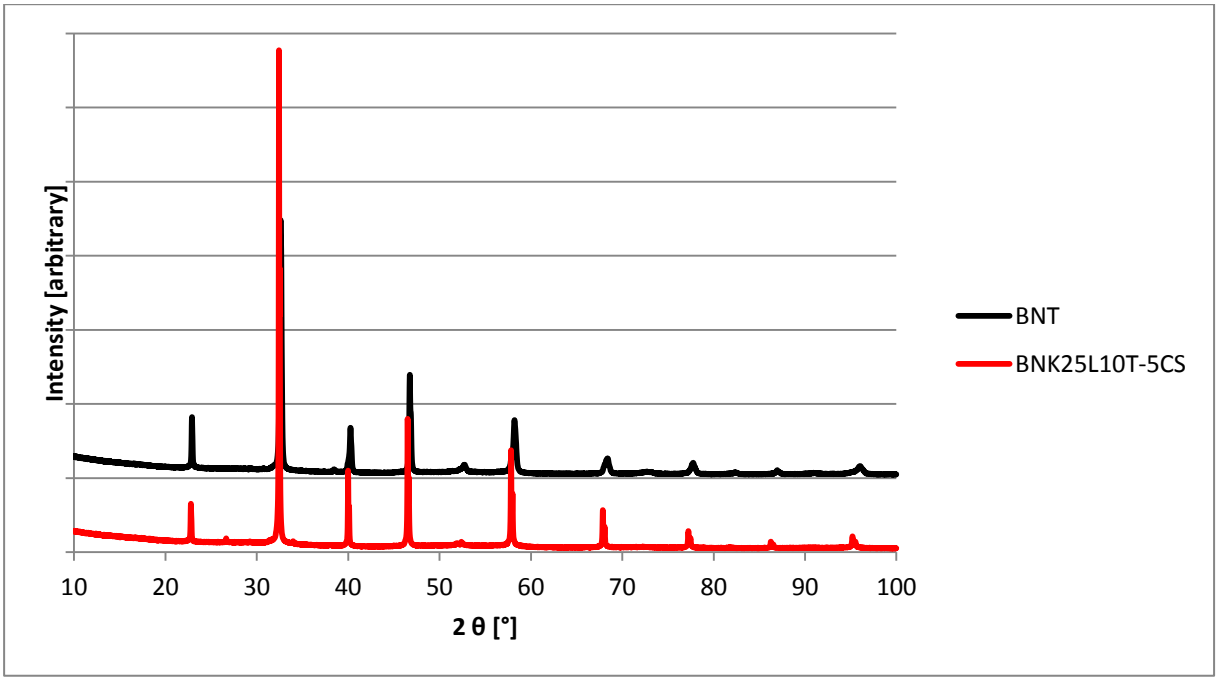


Figure 50: XRD-patterns of BNT and BNK25L10T-5CS.

The elemental composition of BNK25L10T-5CS leads to a rhombohedral perovskite with a cell volume of 356.9835 Å³ (Table 17) which is 1.47 % larger than BNT. This growth of the volume is caused by the very big potassium ion and the large tin ion. The influence of the small ions lithium and calcium is too low to reduce the cell volume, mainly a reason of the small dopant concentrations.

Table 17: Comparison of grain size and cell volume of BNT and BNK25L10T-5CS.

	BNT	**BNK25L10T-5CS**
Grain size [µm]	2.0	1.0
Cell volume [Å³]	351.8229	356.9835

The reduction of the grain size in the ceramic is a phenomenon, which is also visible in BNT-25BKT, which shows a grain size of 0.56 µm. The SEM image (Figure 51) shows some secondary phase inclusions, the composition could not be determined with EDX because of the lithium content of the material. The EDX spectrum suggests a tin-rich composition.

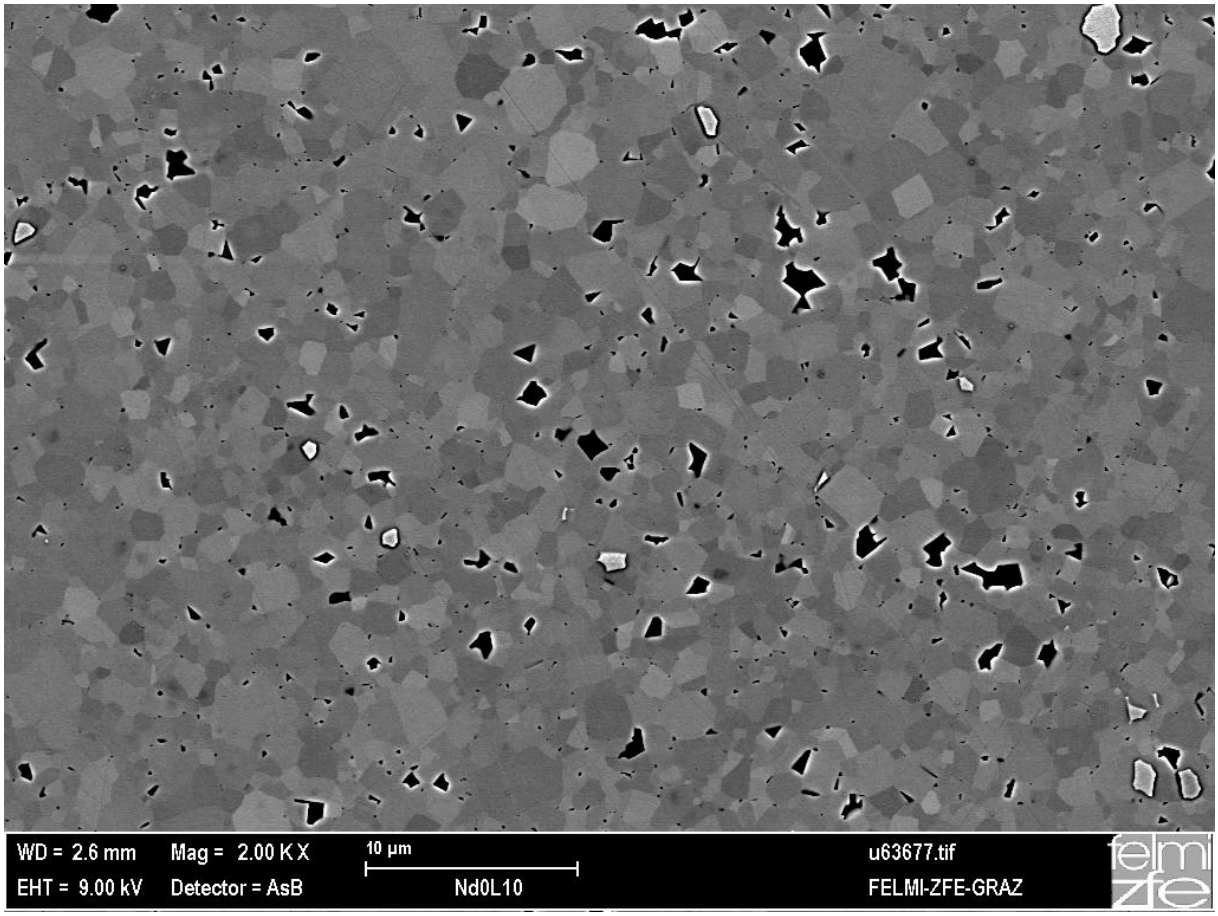


Figure 51: **Microstructure of BNK25L10T-5CS.**

The microstructure of BNK25L10T-5CS shows a very uniform material with little porosity. The relative density of the ceramic is > 95 %, making electrical measurements with high electric fields possible. The used doping materials and the base composition BNT-25BKT lead to the evolution of a thin hysteresis loop with low remnant polarization and low coercive field, which is shown in Figure 52.

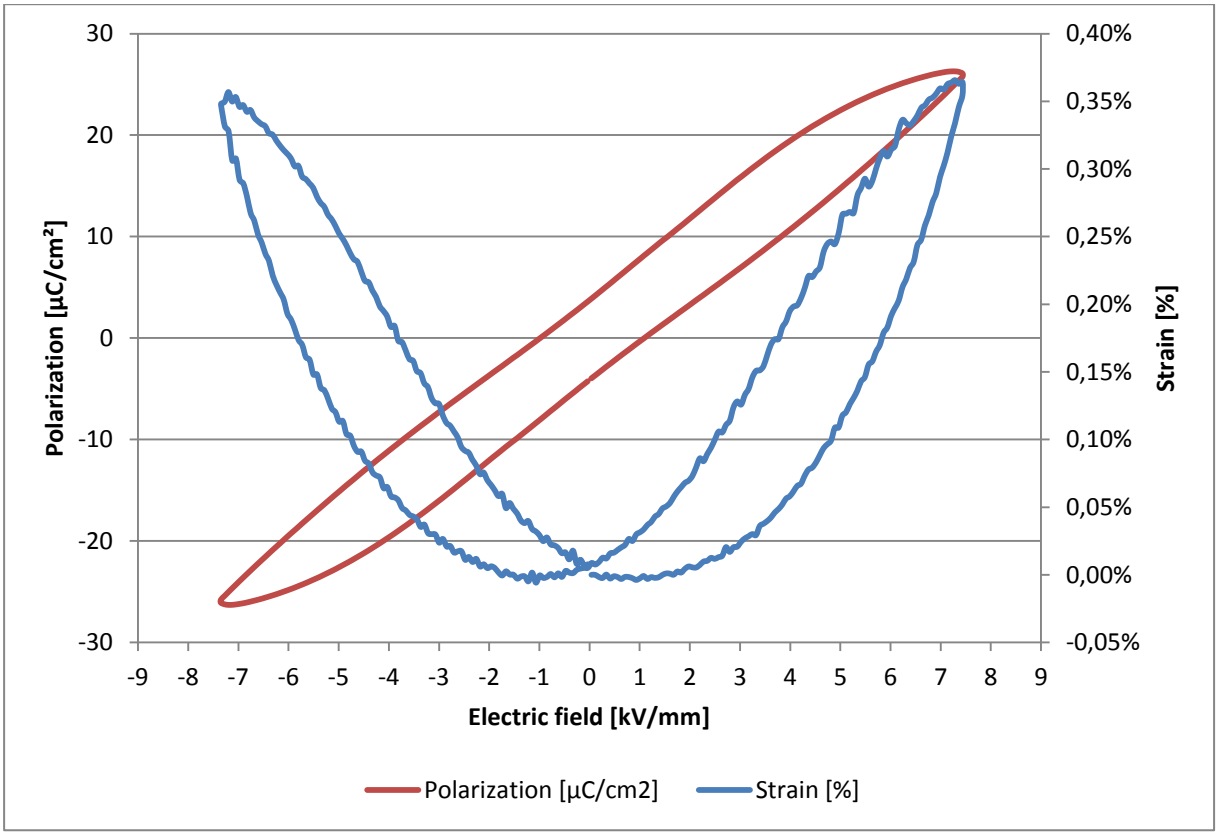


Figure 52: **Bipolar hysteresis loop of BNK25L10T-5CS.**

The bipolar hysteresis with a driving field of 7.44 kV/mm is not sufficient to reach saturation of the material. The gathered values for E_c and P_r are therefore not valid. The material breaks down mechanically at higher driving fields because of the huge strain. Even though the hysteresis loop is far from being saturated, the strain reaches a maximum 0.36 % or a d_{33} of 437 pm/V. Under the influence of a unipolar electric field, saturation can be achieved (Figure 53).

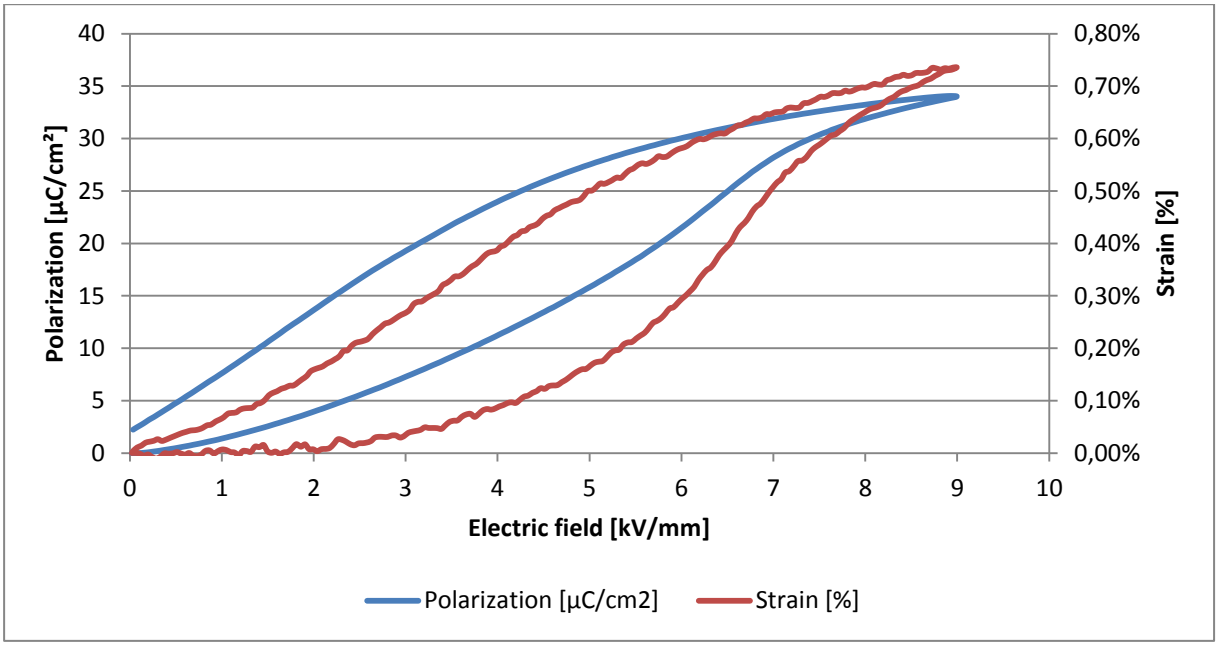


Figure 53: Unipolar hysteresis loop of BNK25L10T-5CS.

Under the influence of an unipolar field with a strength of 8.99 kV/mm, the material reaches saturation. The maximum polarization reaches a value of 33.8 µC/cm², the remnant polarization is with 2.71 µC/cm² very low. The strain reaches a maximum of 0.73 % or a d_{33} of 590 pm/V which is a very high value. Measurements with higher driving fields were also conducted, but the disc-shaped samples collapse under the mechanical stress introduced by the strain.

As with the materials discussed in the chapters 4.1 to 4.4.8, temperature dependence of the permittivity and the loss factor have to be concerned for application. A temperature stable material is more easy to use, since it does not require a temperature controlled driving field or temperature tuning with other devices. Figure 54 shows the dependence of the permittivity and the loss factor of the ceramic.

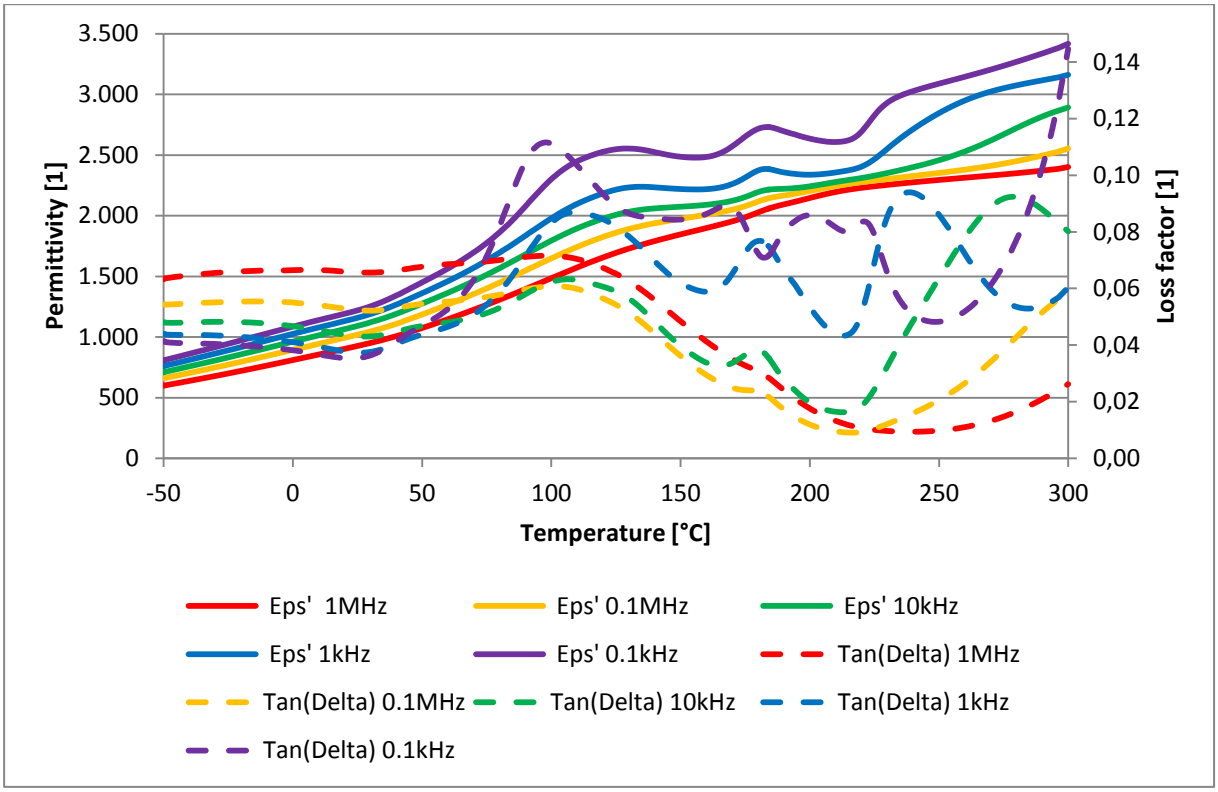


Figure 54: **Temperature dependence of permittivity and loss tangent of BNK25L10T-5CS.**

As expected, the transition temperatures are very diffuse; a result of the high count of different ions, especially on the A-site of the perovskite. T_d is located at approximately 95 °C, the diffusivity of this transition is the reason for the slim hysteresis loop measured at room temperature. There are no jumps of the permittivity at transition temperatures, giving the material an almost linear raise of permittivity over temperature and high frequencies. The wavy character of the loss factor at low measurement frequencies is caused by the superimposed transition points of the used material, which become present only at low frequencies. The losses are very low in general, application temperatures over 100 °C and frequencies > 100 Hz enhance the performance.

Temperature dependence is of course also an important point in high field applications. The small signal data shown in Figure 54 gives hope to good parameters in this respect, since there are no sharp transition points. Figure 55 and Figure 56 show the influence of temperature on the polarization and strain, measured at 8.5 kV/mm and 0.1 Hz.

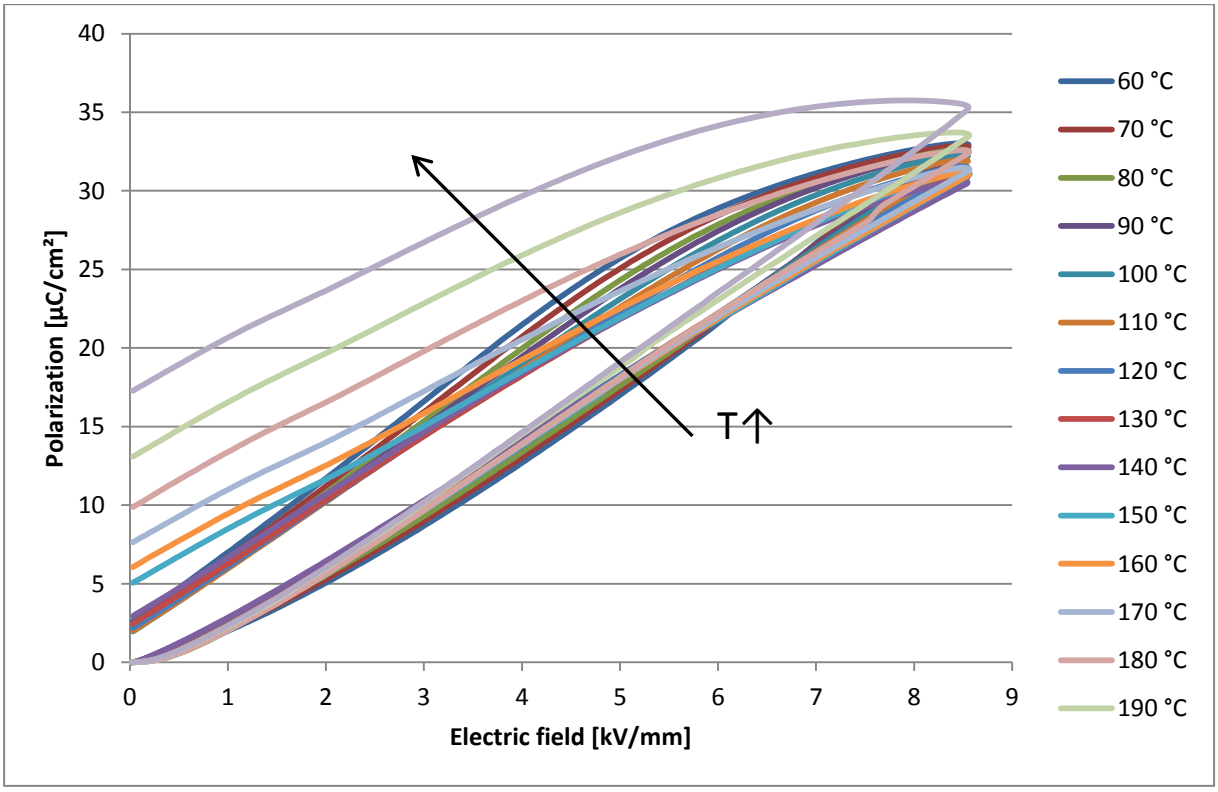


Figure 55: **Temperature dependant unipolar polarization loops of BNK25L10T-5CS.**

The polarization loops measured from 60 °C to 140 °C are almost indistinguishable, at temperatures > 140 °C the material gets lossy, possibly caused by conduction. Overall, the material behaves very well in this respect showing very little response over a large temperature window.

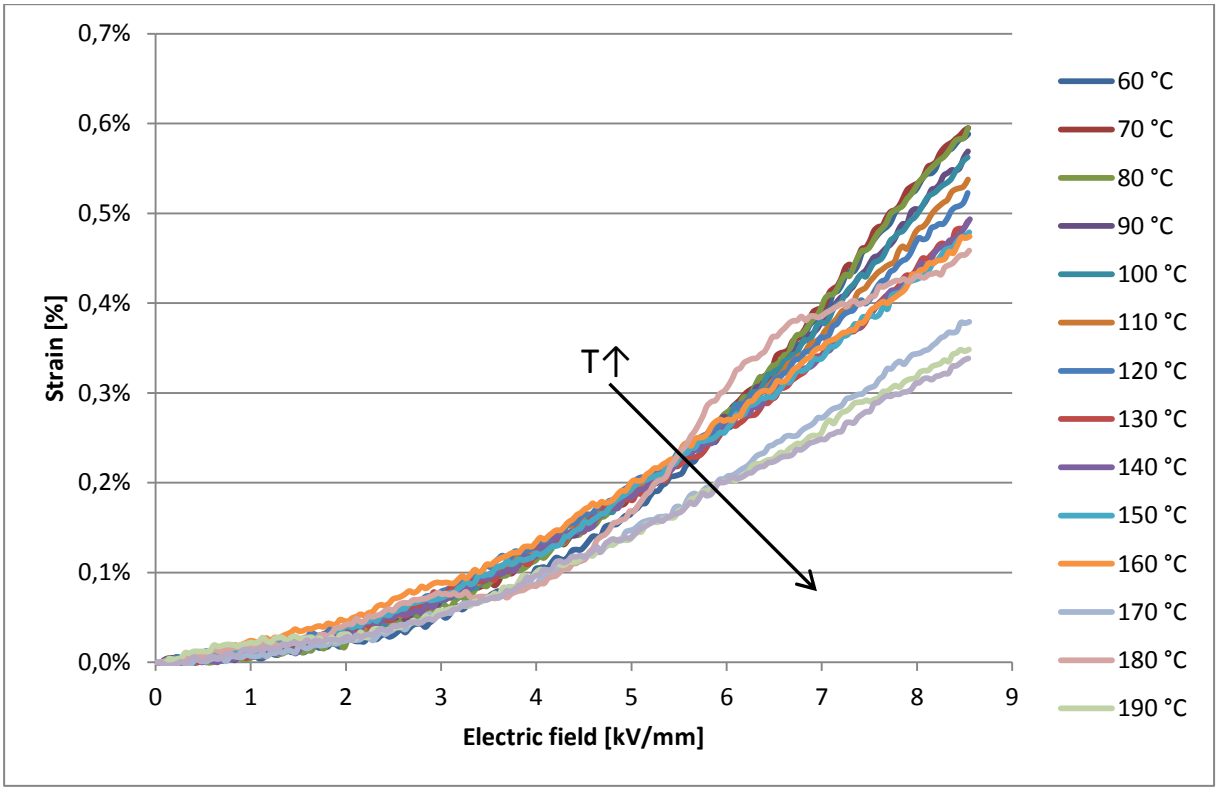


Figure 56: Temperature dependant unipolar strain loops of BNK25L10T-5CS.

Comparable to the polarization before, the strain shows very low temperature dependence up to temperatures of even 160 °C. At higher temperatures, the strain drops to still very high levels of 0.33 % at 190 °C. The reduction of the strain can of course be caused by a reduction of the internal electric field of the sample, caused by conduction.

4.5.2.1. BNK25L10T-5CS as actor material

The performance of BNK25L10T-5CS can be described as outstanding. It shows excellent strain data, both in respect of value and temperature dependence. The sample geometry used in this work (discs) prohibited the measurement of the full potential of the material at electric fields > 10 kV/cm, which would be very interesting. The high field piezoelectric coefficient of 590 pm/V is among the largest reported for lead-free materials. Materials making use of a morphotropic phase boundary like 0.92BNT-0.06BT-0.02KNN reach values of 567 pm/V[20] but usually suffer from high temperature dependence.

5. Conclusion

This work gives an overview of the possible methods to influence the electric properties of the lead-free ferroelectric material BNT. The effect of different substituents on the A- and B-site of the material is clarified and discussed. The main focus of this work is the reduction of the transition temperature T_d to stabilize the antiferroelectric or nonpolar phase with its benefits such as high permittivity and low loss factor at temperatures at and below room temperature.

Donor doping of BNT has a high impact on the shape of the hysteresis loop, regarding the reduction of the ferroelectric hardness of the material. The used dopants calcium, cerium and niobium show mixed results. Calcium and niobium effectively reduce the ferroelectricity of BNT, whereas cerium doping delivers very lossy hysteresis loops. Cerium doped samples also show very poor densification at the used sintering temperatures. Also, donor doped samples are very prone to secondary phase formation; the decomposition reaction reduces the vacancy concentration induced by the donors to a stable level. Hence the concentration range for an effective donor doping is limited to xxx mol%. Therefore the doping concept of PLZT with its La-concentration exceeding 10% seems to be not applicable in BNT.

Isovalent doping and solid solutions with other perovskites also show very high impacts on the material parameters of BNT. Substitutions of titanium with tin or zirconium with concentrations up to 8 % deliver single phase ceramics without evidence for decomposition reactions. Also, the formation of solid solutions with other perovskites such as $CaTiO_3$ and $CaSnO_3$ up to concentrations of 8 % is possible without evidence for secondary phase inclusions; the impact on the electrical parameters is very high in the case of $CaSnO_3$ doping.

The experiments show that the high impact of $CaSnO_3$ on BNT is a result of adding up the effects of single calcium and tin doping. Calcium, being smaller than the average ionic radius of bismuth and sodium shifts the tolerance factor of BNT to lower values. Tin, with its larger ionic radius, but placed on B-site, also reduces the value of the tolerance factor. The combination of both doping elements results in a large shift of the tolerance factor, which has a major impact on T_d.

Figure 49 shows the evolution of T_d over the Goldschmidt tolerance factor of doped BNT. A deviation of the tolerance factor from 0.9945 always leads to a reduction of T_d in BNT. Since the choice of elements with suitable radius is limited, a combination of A- and B-site dopants like in BNT-xCS is a suitable way to adjust the properties of BNT. The formation of a single phase solid solution preserves the stoichiometry of the ceramic.

The knowledge gained by the experiments based on BNT was applied in a prototype material consisting of a solid solution based on BNT-25BKT with outstanding results. The material BNK25L10T-5CS shows very high strain values of 0.73 % or a d_{33} of 590 pm/V at 9 kV/mm with very low temperature dependence. The small signal permittivity reaches values of 1140 with a loss factor of 0.036 (1 kHz, room temperature). At an electric field of 8 kV/mm the relative permittivity reaches a value of 4540.

6. References

[1] Amtsblatt der Europäischen Union, "RICHTLINIE 2002/95/EG DES EUROPÄISCHEN PARLAMENTS UND DES RATES vom 27. Januar 2003 zur Beschränkung der Verwendung bestimmter gefährlicher Stoffe in Elektro- und Elektronikgeräten," vol. L 37, pp. 19–23, 2003.

[2] J. Rödel, W. Jo, K. T. P. Seifert, E. Anton, T. Granzow, and D. Damjanovic, "Perspective on the Development of Lead-free Piezoceramics," *J. Am. Ceram. Soc.*, vol. 92, no. 6, pp. 1153–1177, Jun. 2009.

[3] T. Takenaka and H. Nagata, "Current status and prospects of lead-free piezoelectric ceramics," *J. Eur. Ceram. Soc.*, vol. 25, pp. 2693–2700, 2005.

[4] H. Schaumburg, *Werkstoffe und Bauelemente der Elektrotechnik, Bd.5, Keramik*. 1994.

[5] B. Jaffe and W. R. Cook, *Piezoelectric Ceramics*. 1971, p. 317.

[6] A. J. Moulson and J. M. Herbert, *Electroceramics*. 2003.

[7] G. H. Haertling, "Ferroelectric Ceramics: History and Technology," *J. Am. Ceram. Soc.*, vol. 82, no. 4, pp. 797–818, 1999.

[8] R. D. Shannon, "Revised effective ionic radii and systematic studies of interatomic distances in halides and chalcogenides," *Acta Crystallogr. Sect. A*, vol. 32, no. 5, pp. 751–767, Sep. 1976.

[9] V. M. Goldschmidt, "Die Gesetze der Krystallochemie," *Naturwissenschaften*, vol. 14, no. 21, pp. 477–485, 1926.

[10] F. A. Kröger and H. J. Vink, "Relations between the Concentrations of Imperfections in Crystalline Solids," *Solid State Phys.*, vol. 3, pp. 307–435, 1956.

[11] T. Takenaka, H. Nagata, and Y. Hiruma, "Phase Transition Temperatures and Piezoelectric Properties of $(Bi_{0.5}Na_{0.5})TiO_3$- and $(Bi_{0.5}K_{0.5})TiO_3$-Based Bismuth Perovskite Lead-Free Ferroelectric Ceramics," *IEEE Trans. Ultrason. Ferroelectr. Freq. Control*, vol. 56, no. 8, pp. 1595–1612, 2009.

[12] M. Otoničar, S. D. Škapin, M. Spreitzer, and D. Suvorov, "Compositional range and electrical properties of the morphotropic phase boundary in the $Na_{0.5}Bi_{0.5}TiO_3$–$K_{0.5}Bi_{0.5}TiO_3$ system," *J. Eur. Ceram. Soc.*, vol. 30, no. 4, pp. 971–979, Mar. 2010.

[13] M. Spreitzer, M. Valant, and D. Suvorov, "Sodium deficiency in $Na_{0.5}Bi_{0.5}TiO_3$," *J. Mater. Chem.*, vol. 17, no. 2, pp. 185–192, 2007.

[14] Y. S. Sung, J. M. Kim, J. H. Cho, T. K. Song, M. H. Kim, and T. G. Park, "Effects of Bi nonstoichiometry in $(Bi_{0.5+x}Na)TiO_3$ ceramics," *Appl. Phys. Lett.*, vol. 98, no. 1, p. 012902, 2011.

[15] R. Zuo, S. Su, Y. Wu, J. Fu, M. Wang, and L. Li, "Influence of A-site nonstoichiometry on sintering, microstructure and electrical properties of $(Bi_{0.5}Na_{0.5})TiO_3$ ceramics," *Mater. Chem. Phys.*, vol. 110, no. 2–3, pp. 311–315, Aug. 2008.

[16] M. Naderer, D. Schütz, T. Kainz, K. Reichmann, and F. Mittermayr, “The formation of secondary phases in $Bi_{0.5}Na_{0.375}K_{0.125}TiO_3$ ceramics,” *J. Eur. Ceram. Soc.*, vol. 32, no. 10, pp. 3–8, Mar. 2012.

[17] J.-S. Lee, K.-N. Pham, H.-S. Han, H.-B. Lee, and V. D. N. Tran, “Strain enhancement of lead-free $Bi_{1/2}(Na_{0.82}K_{0.18})_{1/2}TiO3$ ceramics by Sn doping,” *J. Korean Phys. Soc.*, vol. 60, no. 2, pp. 212–215, Jan. 2012.

[18] A. Hussain, C. W. Ahn, J.-S. Lee, A. Ullah, and I. W. Kim, “Large electric-field-induced strain in Zr-modified lead-free $Bi_{0.5}(Na_{0.78}K_{0.22})_{0.5}TiO_3$ piezoelectric ceramics,” *Sensors Actuators A Phys.*, vol. 158, no. 1, pp. 84–89, Mar. 2010.

[19] F. Craciun, C. Galassi, and R. Birjega, “Electric-field-induced and spontaneous relaxor-ferroelectric phase transitions in $(Na_{1/2}Bi_{1/2})_{1-x}Ba_xTiO_3$,” *J. Appl. Phys.*, vol. 112, no. 12, p. 124106, 2012.

[20] - - , and H. Ehrenberg, “Lead-free piezoceramics with giant strain in the system $Bi_{0.5}Na_{0.5}TiO_3$–$BaTiO_3$–$K_{0.5}Na_{0.5}NbO_3$. I. Structure and room temperature properties,” *J. Appl. Phys.*, vol. 103, no. 3, p. 034107, 2008.

[21] W. Krauss, D. Schütz, F. A. Mautner, A. Feteira, and K. Reichmann, “Piezoelectric properties and phase transition temperatures of the solid solution of $(1-x)(Bi_{0.5}Na_{0.5})TiO_3$–$xSrTiO_3$,” *J. Eur. Ceram. Soc.*, vol. 30, no. 8, pp. 1827–1832, Jun. 2010.

[22] J. König, M. Spreitzer, and D. Suvorov, “Influence of the synthesis conditions on the dielectric properties in the $Bi_{0.5}Na_{0.5}TiO_3$–$KTaO_3$ system,” *J. Eur. Ceram. Soc.*, vol. 31, no. 11, pp. 1987–1995, Oct. 2011.

[23] G. H. Haertling and C. E. Land, “Hot-Pressd $(Pb,La)(Zr,Ti)O_3$ Ferroelectric Ceramics for Electrooptic Applications,” *J. Am. Ceram. Soc.*, vol. 54, no. 1, pp. 1–11, 1971.

[24] P. Jaiban, A. Rachakom, S. Jiansirisomboon, and A. Watcharapasorn, “Effects of Sintering Temperatures on Preparation of BNZ Ceramic,” *J. Microsc. Soc. Thail.*, vol. 4, no. 1, pp. 20–23, 2011.

[25] P. Jaiban, A. Rachakom, S. Jiansirisomboon, and A. Watcharapasorn, “Influences of phase transition and microstructure on dielectric properties of $Bi_{0.5}Na_{0.5}Zr_{1-x}Ti_xO_3$ ceramics.,” *Nanoscale Res. Lett.*, vol. 7, no. 1, p. 45, Jan. 2012.

[26] B. K. Barick, R. N. P. Choudhary, and D. K. Pradhan, “Dielectric and impedance spectroscopy of zirconium modified $(Na_{0.5}Bi_{0.5})TiO_3$ ceramics,” *Ceram. Int.*, vol. 39, no. 5, pp. 5695–5704, Jul. 2013.

[27] Y. Watanabe, Y. Hiruma, H. Nagata, and T. Takenaka, “Phase transition temperatures and electrical properties of divalent ions (Ca^{2+}, Sr^{2+} and Ba^{2+}) substituted $(Bi_{1/2}Na_{1/2})TiO_3$ ceramics,” *Ceram. Int.*, vol. 34, no. 4, pp. 761–764, May 2008.

[28] T. Takenaka, Y. Watanabe, H. Nagata, and Y. Hiruma, “Phase Transition Temperatures of Divalent and Trivalent Ions Substituted BNT Ceramics,” *Key Eng. Mater.*, vol. 350, pp. 93–96, 2007.

[29] R. Ranjan and A. Dviwedi, “Structure and dielectric properties of $(Na_{0.50}Bi_{0.50})_{1-x}Ba_xTiO_3$: 0≤x≤0.10,” *Solid State Commun.*, vol. 135, no. 6, pp. 394–399, Aug. 2005.

[30] G. O. Jones, J. Kreisel, and P. A. Thomas, “A structural study of the $(Na_{1-x}K_x)_{0.5}Bi_{0.5}TiO_3$ perovskite series as a function of substitution (x) and temperature,” *Powder Diffr.*, vol. 17, no. 4, pp. 301–319, 2002.

[31] International Organization for Standardization, “DIN EN ISO 643:2003.” 2003.

[32] R. Yimnirun, a. Ngamjarurojana, R. Wongmaneerung, S. Wongsaenmai, S. Ananta, and Y. Laosiritaworn, “Temperature scaling of ferroelectric hysteresis in hard lead zirconate titanate bulk ceramic,” *Appl. Phys. A*, vol. 89, no. 3, pp. 737–741, Jun. 2007.

[33] M. Naderer, T. Kainz, D. Schütz, and K. Reichmann, “The influence of Ti-nonstoichiometry in $Bi_{0.5}Na_{0.5}TiO_3$,” *J. Eur. Ceram. Soc.*, 2013.

[34] G. Shirane and R. Newnham, “Dielectric Properties and Phase Transitions of $NaNbO_3$ and (Na, K)NbO_3,” *Phys. Rev.*, vol. 96, no. 8, 1954.

[35] D. Lin, C. Xu, Q. Zheng, Y. Wei, and D. Gao, “Piezoelectric and dielectric properties of $Bi_{0.5}Na_{0.5}TiO_3$–$Bi_{0.5}Li_{0.5}TiO_3$ lead-free ceramics,” *J. Mater. Sci. Mater. Electron.*, vol. 20, no. 5, pp. 393–397, May 2008.

7. Image directory

Figure 1: Schematic drawing of perovskite structure[7]. 9

Figure 2: Polarization mechanisms in dielectric materials[6]. 12

Figure 3: Schematic illustration of the direct (a) and converse (b) piezoelectric effect. 13

Figure 4: Comparison of a hard (left) and a soft (right) ferroelectric hysteresis loop[6]. 14

Figure 5: Phase diagram of (1-x)BNT-xBKT showing the BNT-rich side, including transition temperatures[11]. 16

Figure 6: Workflow mixed oxide route. 26

Figure 7 Temperature characteristic for the calcination process. 27

Figure 8: Temperature characteristic for the sintering step. 29

Figure 9: XRD pattern of BNT. 32

Figure 10: Channeling contrast SEM image of BNT. 33

Figure 11: Hysteresis loop of BNT. 34

Figure 12: Temperature dependence of permittivity and loss tangent in BNT. 35

Figure 13: XRD pattern of BNT-25BKT. 37

Figure 14: SEM image of the microstructure of BNT-25BKT, sintered at 1150 °C. 38

Figure 15: Polarization loops for BNT and BNT-25BKT. 39

Figure 16: Strain loops for BNT and BNT-25BKT 40

Figure 17: Temperature dependence of permittivity and loss tangent in BNT-25BKT. 41

Figure 18: XRD patterns of donor doped BNT with calcium. The emerging peaks at Ca-concentrations > 0.5 % are caused by inclusions of $Bi_2Ti_3O_9$. 43

Figure 19: Hysteresis loops of Ca-donor doped BNT. 44

Figure 20: XRD patterns of BNT donor doped with cerium. 45

Figure 21: Hysteresis loops of Ce-donor doped BNT. 46

Figure 22: XRD patterns of donor doped BNT with niobium. The emerging peaks at Nb-concentrations > 2 % are caused by inclusions of $Bi_2Ti_2O_7$. 48

Figure 23: Hysteresis loops of Nb-donor doped BNT. 49

Figure 24: XRD patterns of Ti-substituted BNT with germanium. 50

Figure 25: Hysteresis loops of Ge-doped BNT. 51

Figure 26: Temperature dependence of permittivity and loss tangent in BNT-xGe. 52

Figure 27: XRD patterns of Ti-substituted BNT with tin. 53

Figure 28: Hysteresis loops of Sn-doped BNT. 54

Figure 29: Temperature dependence of permittivity and loss tangent in BNT-xSn. 55

Figure 30: XRD patterns of Ti-substituted BNT with zirconium. 56

Figure 31: Hysteresis loops of Zr-doped BNT. 57
Figure 32: Temperature dependence of permittivity and loss tangent in BNT-xZr. 58
Figure 33: XRD patterns of Ti-substituted BNT with a compensated lithium / vanadium mixture. ..
..... 59
Figure 34: Hysteresis loops of Li / V-doped BNT. 60
Figure 35: XRD patterns of Ti-substituted BNT with a compensated lithium / tungsten mixture. 61
Figure 36: Hysteresis loops of Li / W-doped BNT. 62
Figure 37: XRD-patterns of BNT-xCT solid solutions. 63
Figure 38: Hysteresis loops of solid solutions of BNT and CT. 64
Figure 39: Temperature dependence of permittivity and loss tangent in BNT-xCT. 65
Figure 40: Hysteresis loops of solid solutions of BNT and CG. 66
Figure 41: Hysteresis loops of solid solutions of BNT and CS. 67
Figure 42: Hysteresis loops of solid solutions of BNT and CZ. 68
Figure 43: XRD-patterns of BNT-xMT solid solutions. 70
Figure 44: Hysteresis loops of solid solutions of BNT and MT. 71
Figure 45: Temperature dependence of permitivitty and loss tangent in BNT-xMT. 72
Figure 46: Hysteresis loops of solid solutions of BNT and MG. 73
Figure 47: Hysteresis loops of solid solutions of BNT and MS. 74
Figure 48: Hysteresis loops of solid solutions of BNT and MZ. 75
Figure 49: Development of T_d over the Goldschmidt tolerance factor derived from BNT-xGe and
BNT-xZr. 76
Figure 50: XRD-patterns of BNT and BNK25L10T-5CS. 79
Figure 51: Microstructure of BNK25L10T-5CS. 80
Figure 52: Bipolar hysteresis loop of BNK25L10T-5CS. 81
Figure 53: Unipolar hysteresis loop of BNK25L10T-5CS. 82
Figure 54: Temperature dependence of permittivity and loss tangent of BNK25L10T-5CS. 83
Figure 55: Temperature dependant unipolar polarization loops of BNK25L10T-5CS. 84
Figure 56: Temperature dependant unipolar strain loops of BNK25L10T-5CS. 85
Figure 57: Microstructure of BNT-0.25Ge. 96
Figure 58: Microstructure of BNT-0.5Ge. 96
Figure 59: Microstructure of BNT-1Ge. 97
Figure 60: Microstructure of BNT-2Ge. 97
Figure 61: Microstructure of BNT-4Ge. 98
Figure 62: Microstructure of BNT-8Ge. 98
Figure 63: Microstructure of BNT-0.25Sn. 99

Figure 64: Microstructure of BNT-0.5Sn..... 99
Figure 65: Microstructure of BNT-1Sn..... 100
Figure 66: Microstructure of BNT-2Sn..... 100
Figure 67: Microstructure of BNT-4Sn..... 101
Figure 68: Microstructure of BNT-8Sn..... 101
Figure 69: Microstructure of BNT-0.25Zr. 102
Figure 70: Microstructure of BNT-0.5Zr. 102
Figure 71: Microstructure of BNT-1Zr. 103
Figure 72: Microstructure of BNT-2Zr. 103
Figure 73: Microstructure of BNT-4Zr. 104
Figure 74: Microstructure of BNT-8Zr. 104
Figure 75: Microstructure of BNT-0.25CT. 105
Figure 76: Microstructure of BNT-0.5CT. 105
Figure 77: Microstructure of BNT-1CT. 106
Figure 78: Microstructure of BNT-2CT. 106
Figure 79: Microstructure of BNT-4CT. 107
Figure 80: Microstructure of BNT-8CT. 107
Figure 81: Microstructure of BNT-0.25MT. 108
Figure 82: Microstructure of BNT-0.5MT. 108
Figure 83: Microstructure of BNT-1MT. 109
Figure 84: Microstructure of BNT-2MT. 109
Figure 85: Microstructure of BNT-4MT. 110
Figure 86: Microstructure of BNT-8MT. 110

8. Table directory

Table 1: Ionic radii at different coordination numbers for ions used in BNT-BKT. The starred values for Bi^{3+}(XII) and Ti^{4+}(XII) are linear extrapolated from literature values[8]. 9

Table 2: Possible substituents for metal ions incorporated in BNT[8]. 18

Table 3: Possible donor dopants in BNT[8]. 19

Table 4: Milling parameters. 27

Table 5: Average grain size and cell volume of BNT. 34

Table 6: Average grain size and cell volume of BNT-25BKT. 38

Table 7: Comparison of the cell volume of BNT and calcium donor doped materials. 43

Table 8: Comparison of the cell volume of BNT and Ce donor doped materials 46

Table 9: Comparison of the cell volume of BNT and niobium donor doped materials. 48

Table 10: Comparison of the cell volume of BNT and Ge doped materials. 51

Table 11: Comparison of the cell volume of BNT and tin doped materials. 53

Table 12: Comparison of the cell volume of BNT and zirconium doped materials. 56

Table 13: Comparison of the cell volume of BNT and LV doped materials. 59

Table 14: Comparison of the cell volume of BNT and LW doped materials. 61

Table 15: Comparison of the cell volume and grain size of BNT-xCT solid solutions. 64

Table 16: Comparison of the cell volume and the grain size of BNT-xMT solid solutions. 70

Table 17: Comparison of grain size and cell volume of BNT and BNK25L10T-5CS 79

9. Equation directory

Equation 1: Calculation of the Goldschmidt tolerance factor. 10

Equation 2: Calculation of the capacitance of a simple capacitor. 11

Equation 3: Calculation of the relative permittivity. 11

Equation 4: Calculation of the polarization. 12

Equation 5: Calculation of the loss factor. 12

Equation 6: Composition of PLZT, donor doped with lanthanum. 20

Equation 7: Composition of Ca-doped samples. 20

Equation 8: Composition of Ce-doped samples. 21

Equation 9: Composition of Nb-doped samples. 21

Equation 10: Composition of Ge-doped samples. 21

Equation 11: Composition of Sn-doped samples. 22

Equation 12: Composition of Zr-doped samples. 22

Equation 13: Decomposition reaction of calcium donor doped BNT. 43

Equation 14: Migration reaction of magnesium from A- to B-site of the perovskite. 71

Equation 15: Composition of BNK25L10T-5CS, the prototype material. 78

10. Appendix

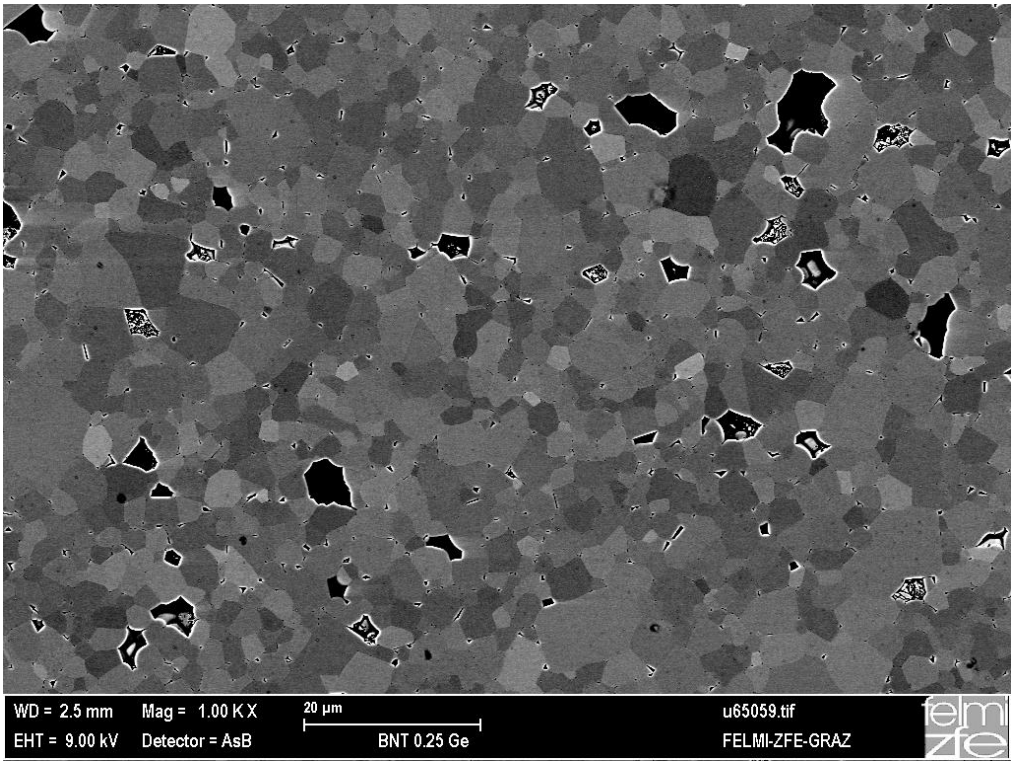


Figure 57: Microstructure of BNT-0.25Ge.

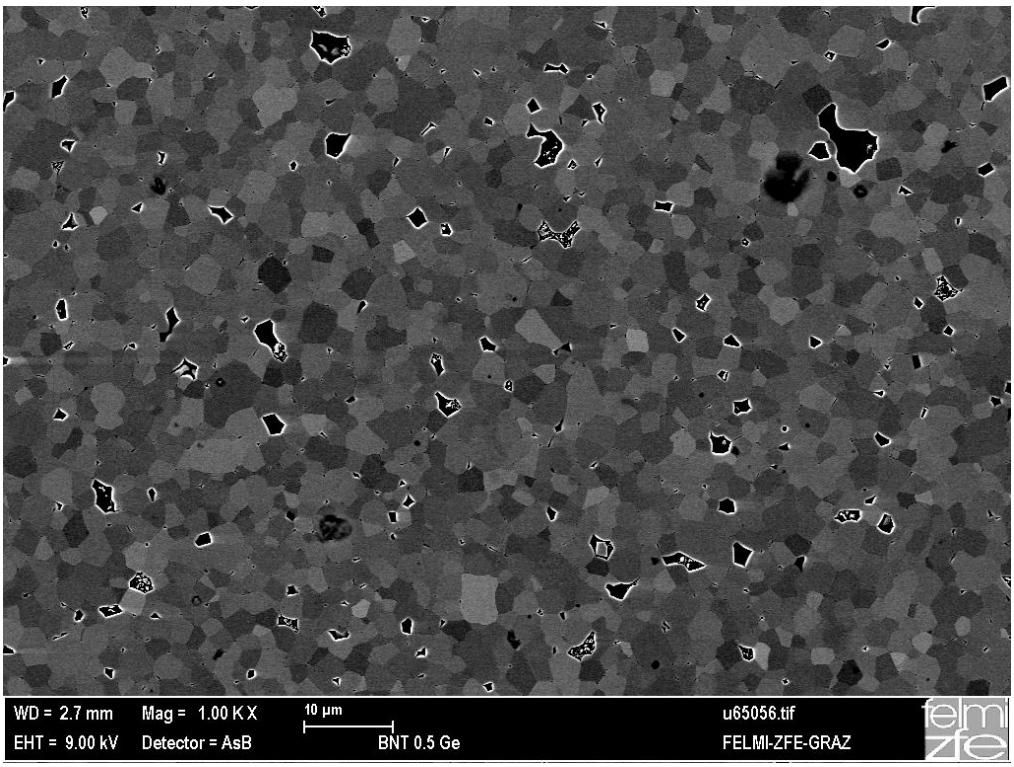


Figure 58: Microstructure of BNT-0.5Ge.

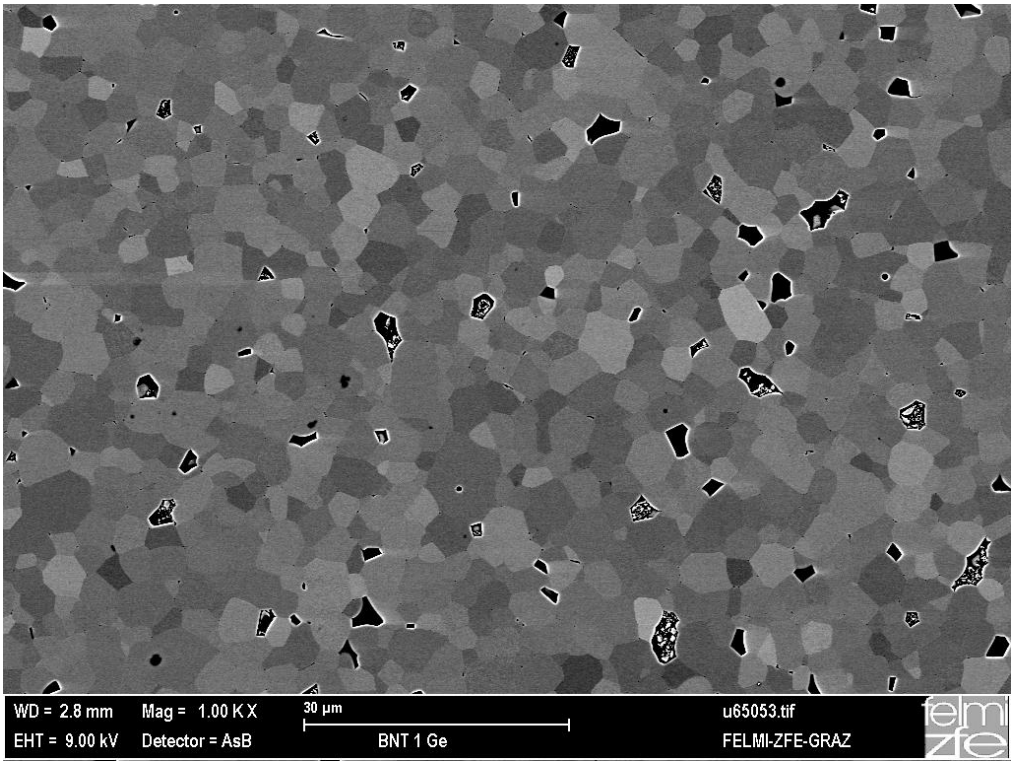


Figure 59: Microstructure of BNT-1Ge.

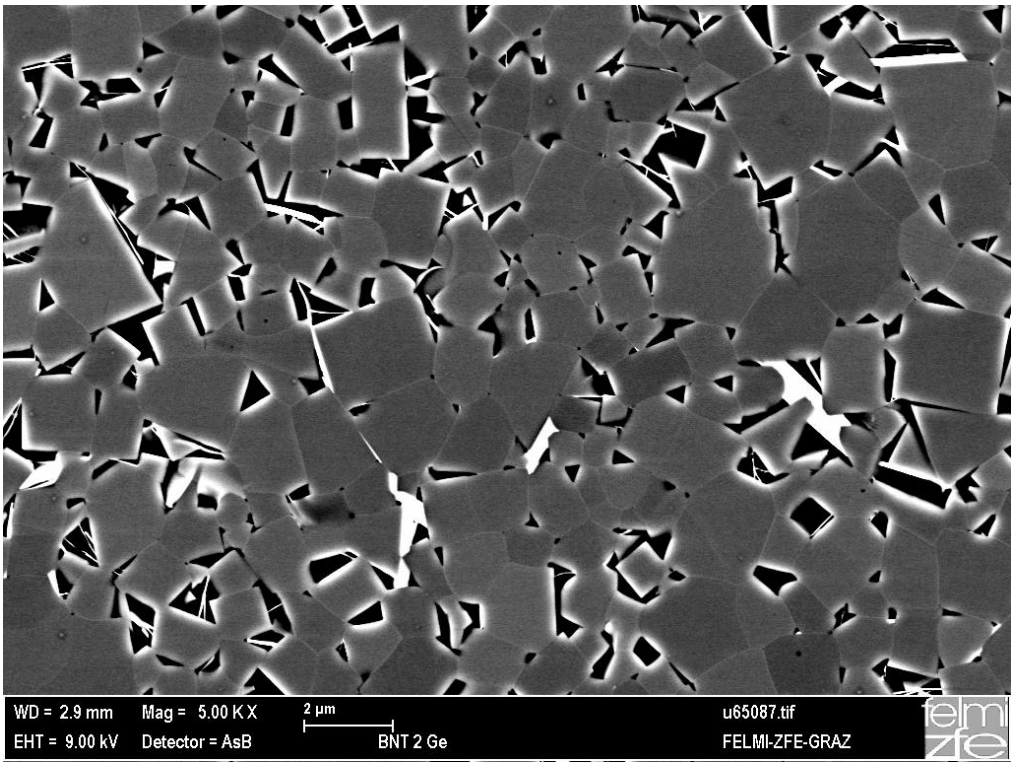


Figure 60: Microstructure of BNT-2Ge.

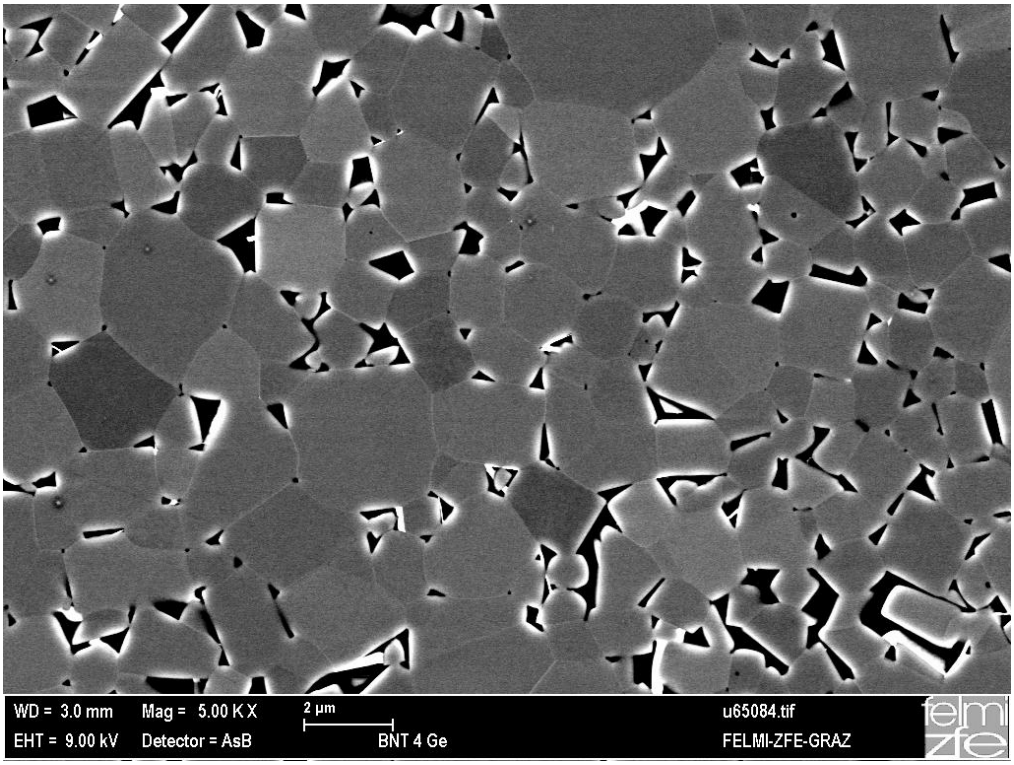


Figure 61: Microstructure of BNT-4Ge.

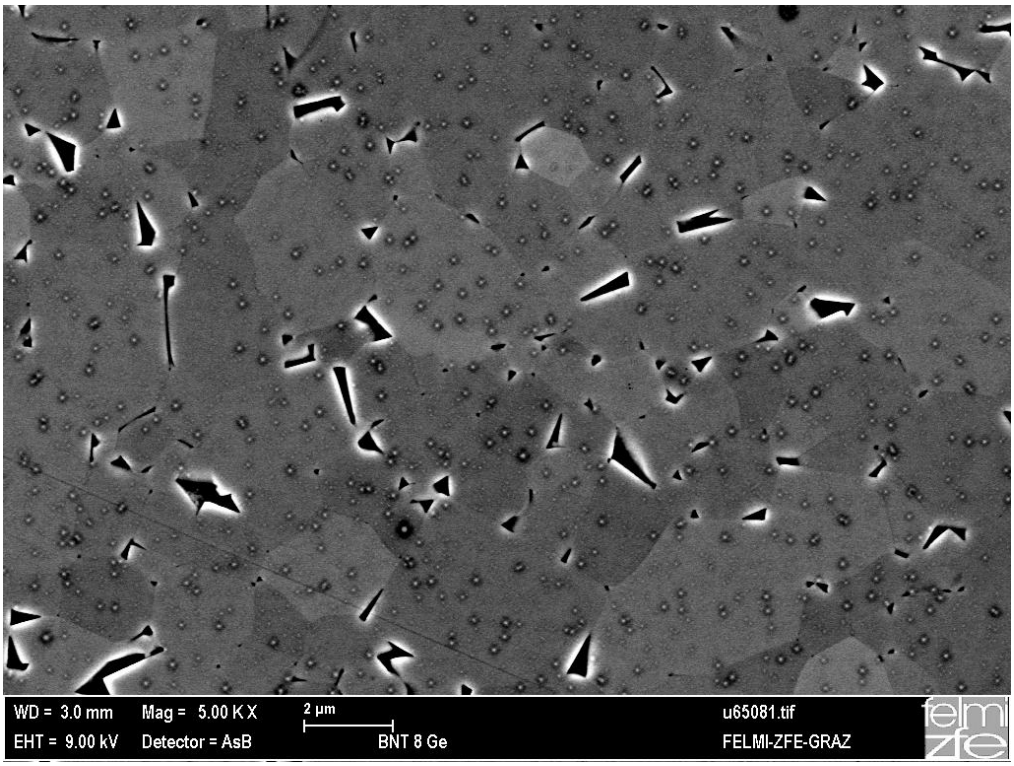


Figure 62: Microstructure of BNT-8Ge.

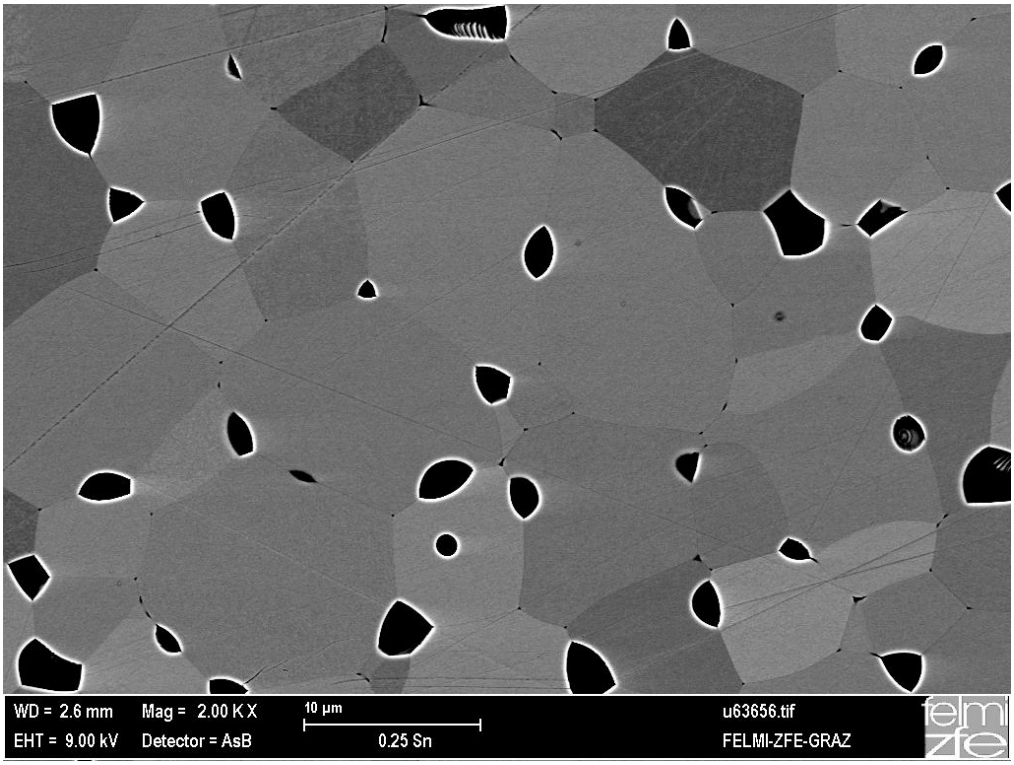


Figure 63: Microstructure of BNT-0.25Sn.

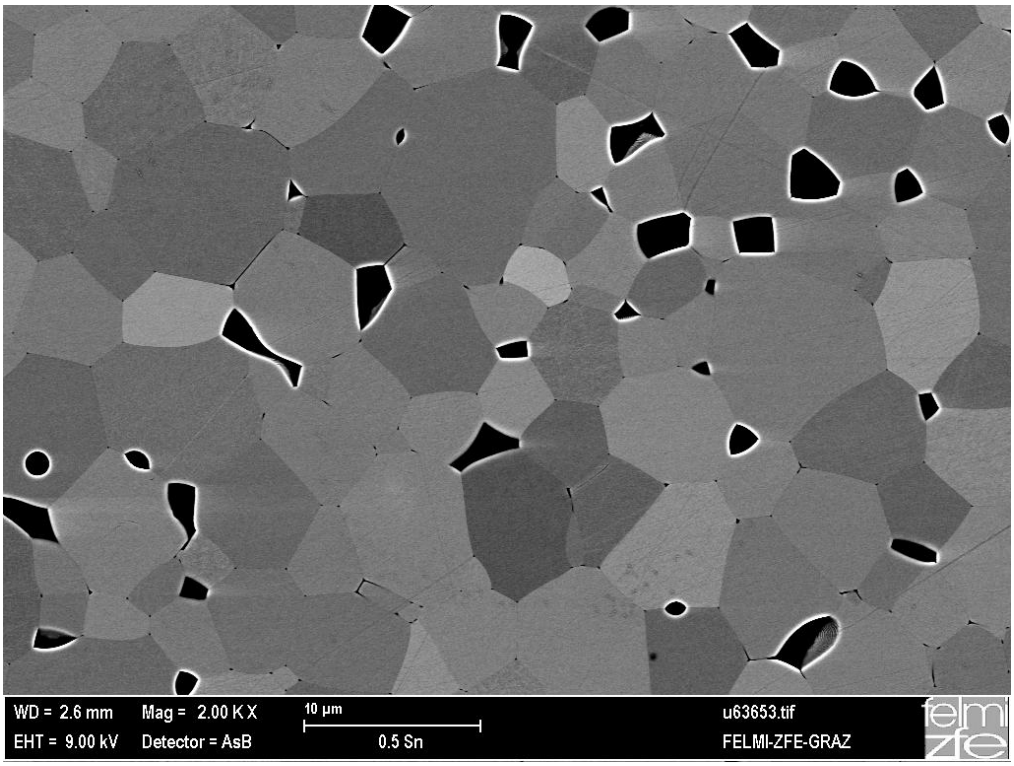


Figure 64: Microstructure of BNT-0.5Sn.

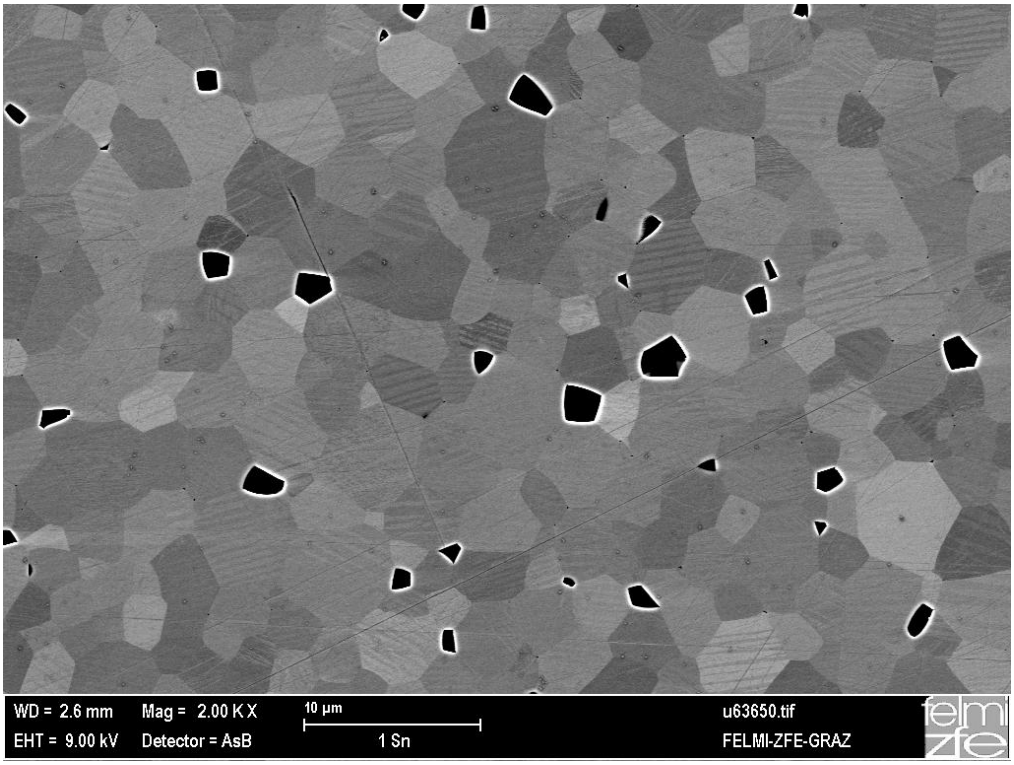


Figure 65: Microstructure of BNT-1Sn.

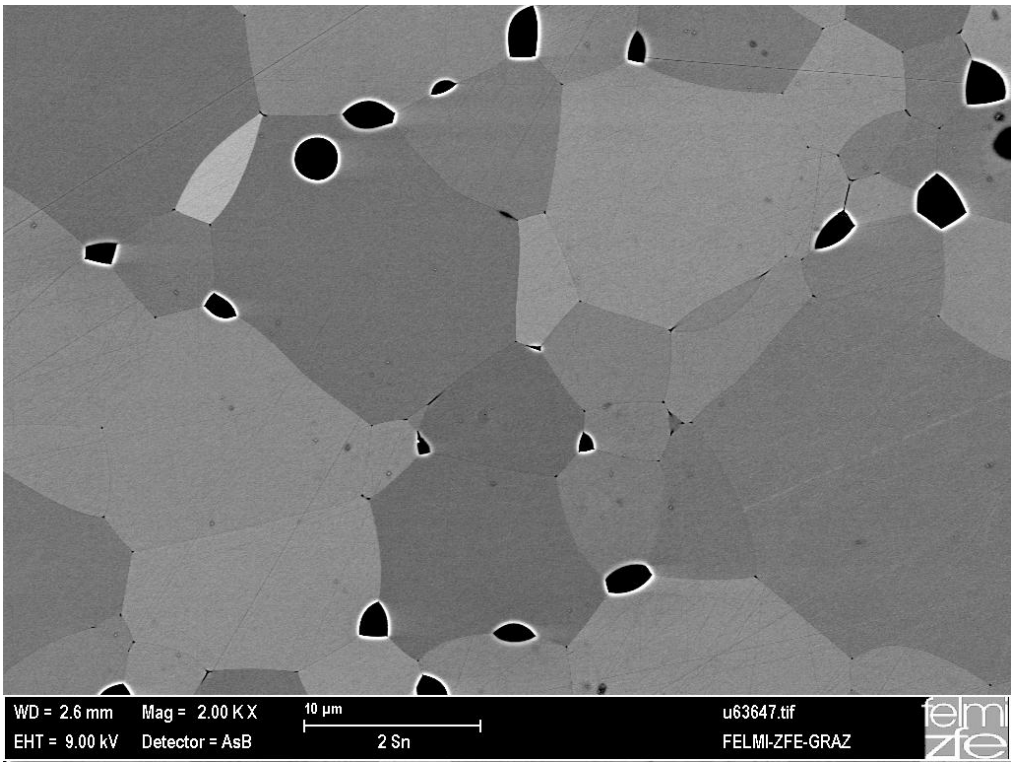


Figure 66: Microstructure of BNT-2Sn.

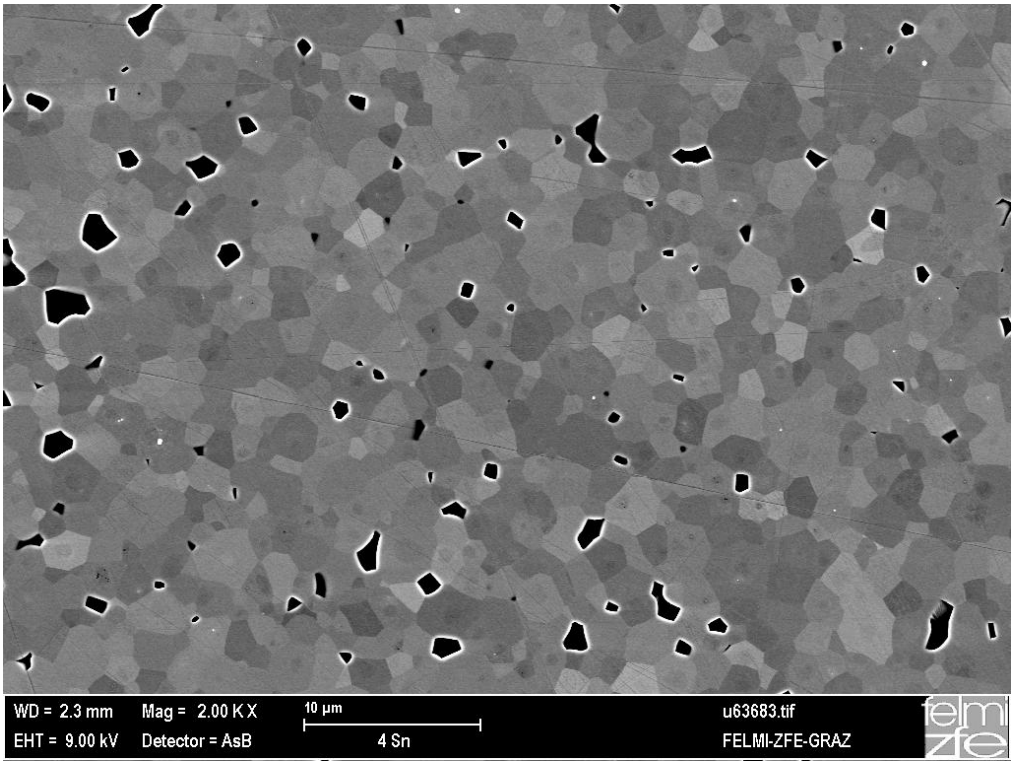


Figure 67: Microstructure of BNT-4Sn.

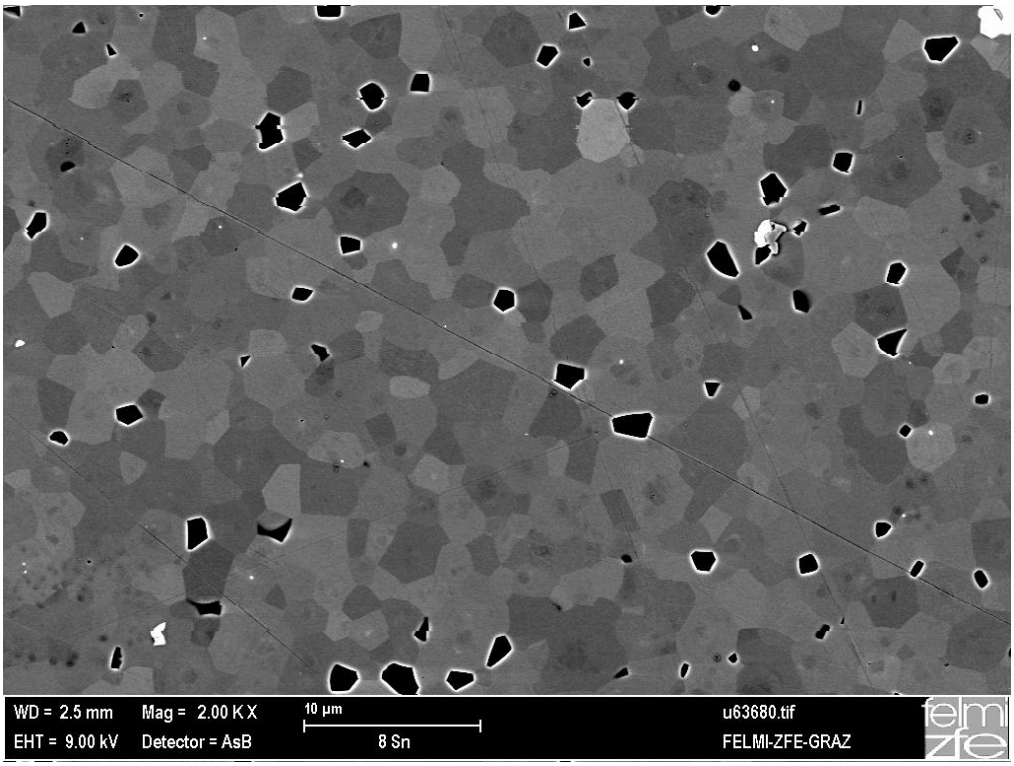


Figure 68: Microstructure of BNT-8Sn.

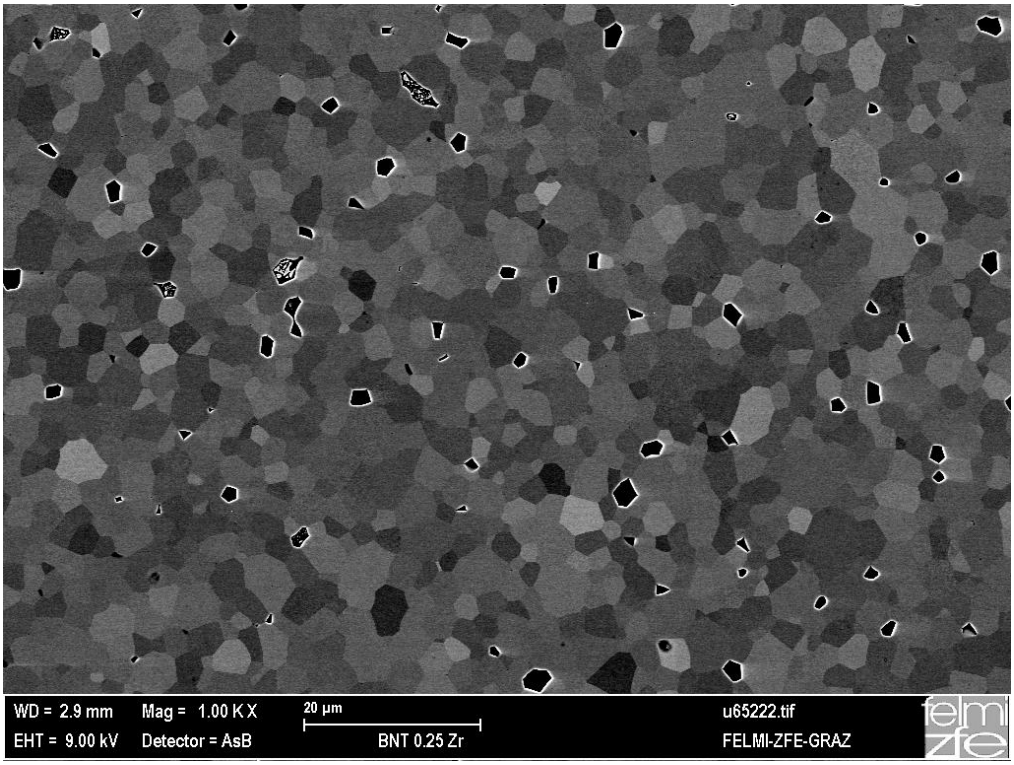


Figure 69: Microstructure of BNT-0.25Zr.

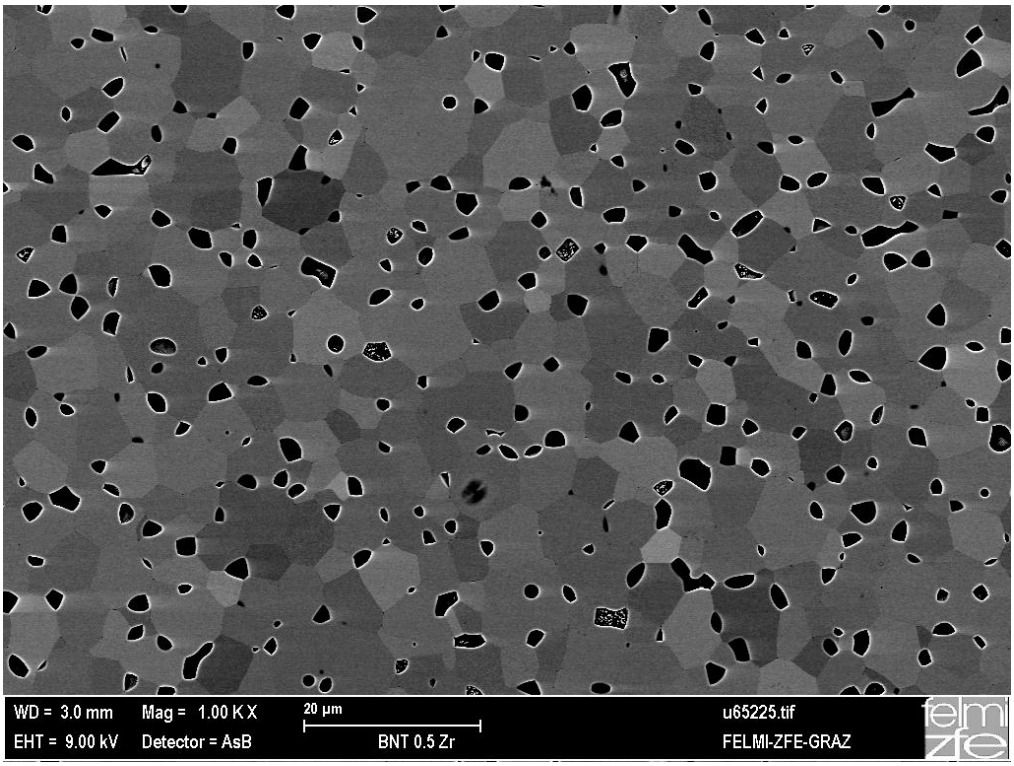


Figure 70: Microstructure of BNT-0.5Zr.

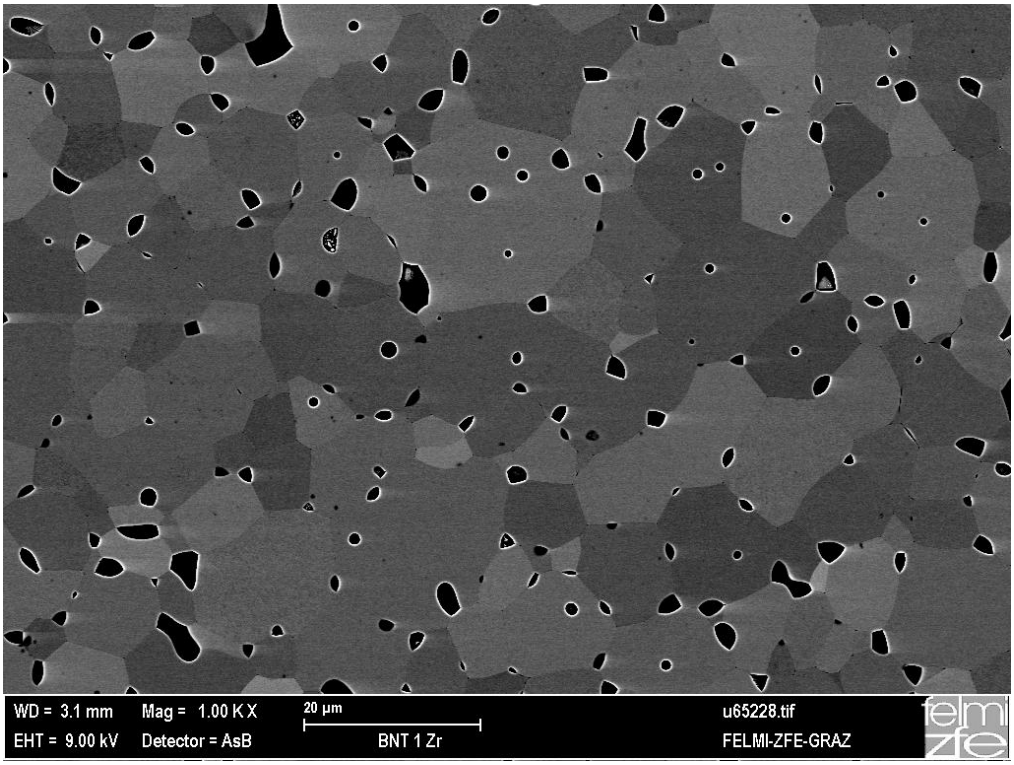


Figure 71: Microstructure of BNT-1Zr.

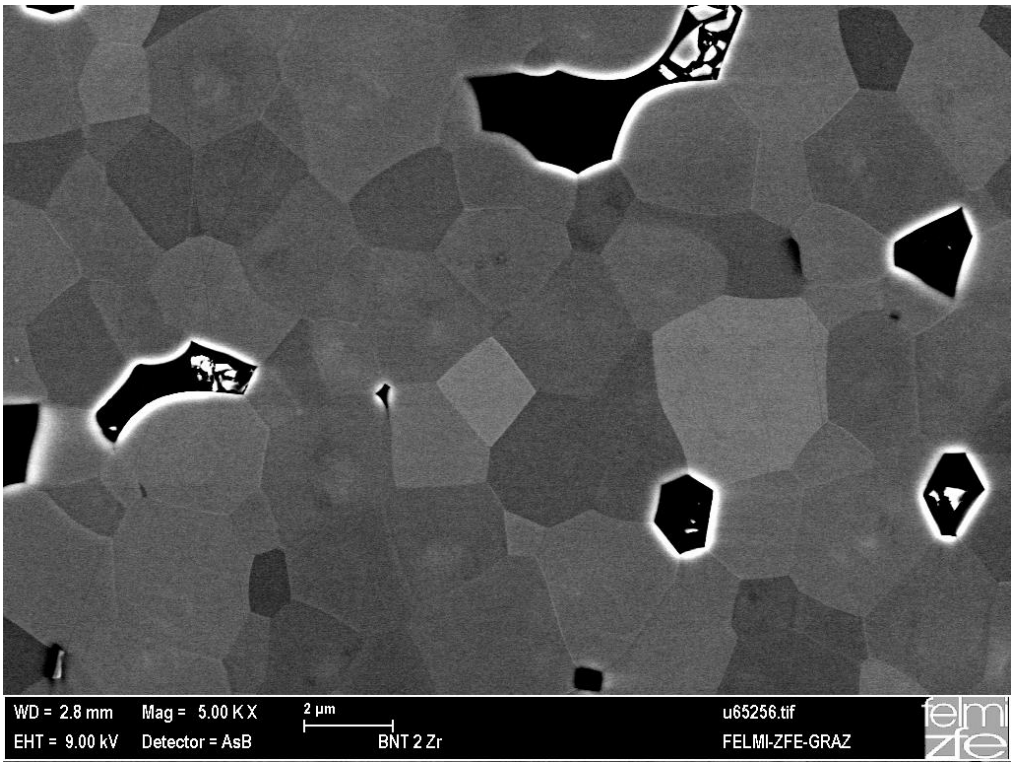


Figure 72: Microstructure of BNT-2Zr.

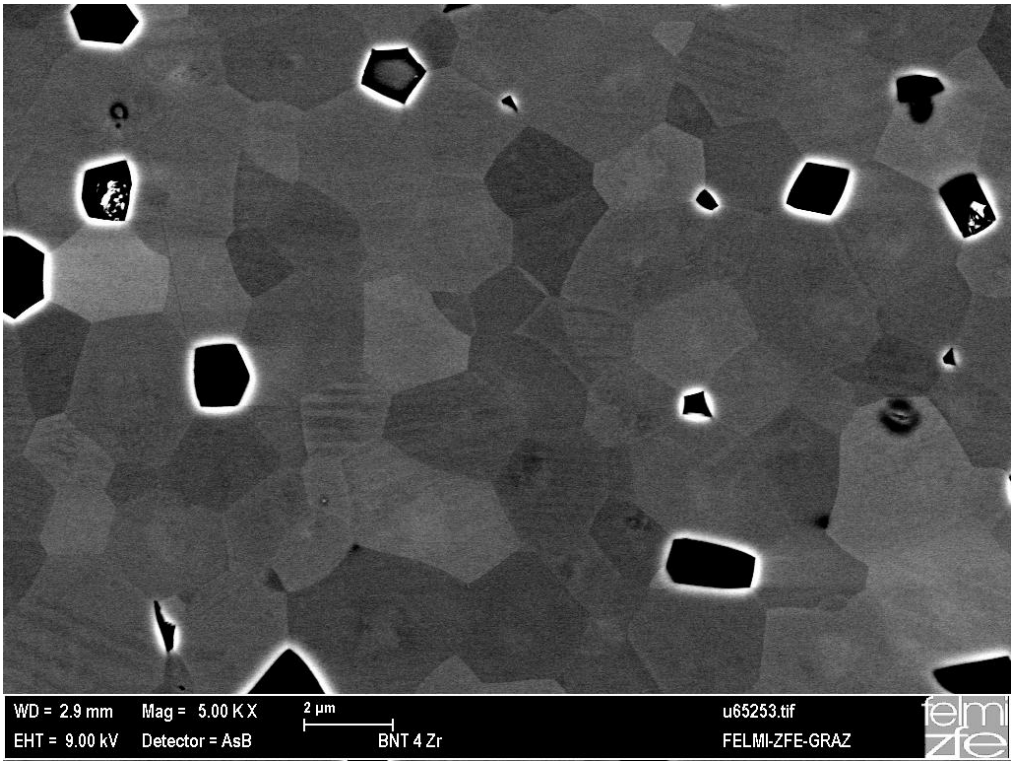


Figure 73: Microstructure of BNT-4Zr.

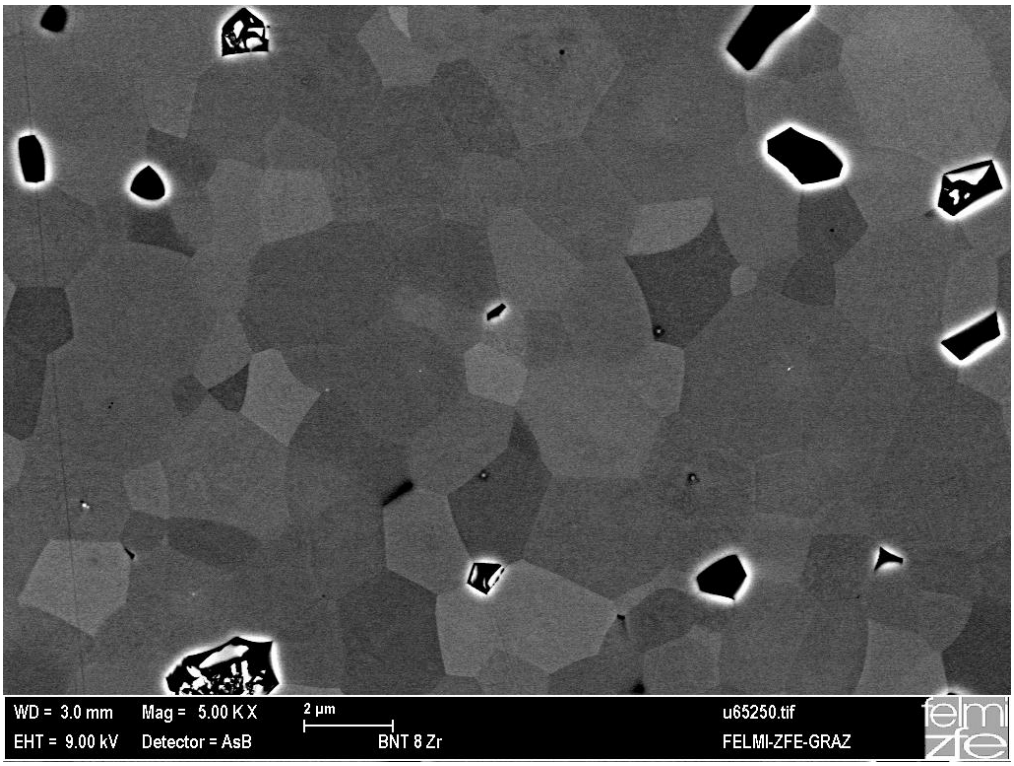


Figure 74: Microstructure of BNT-8Zr.

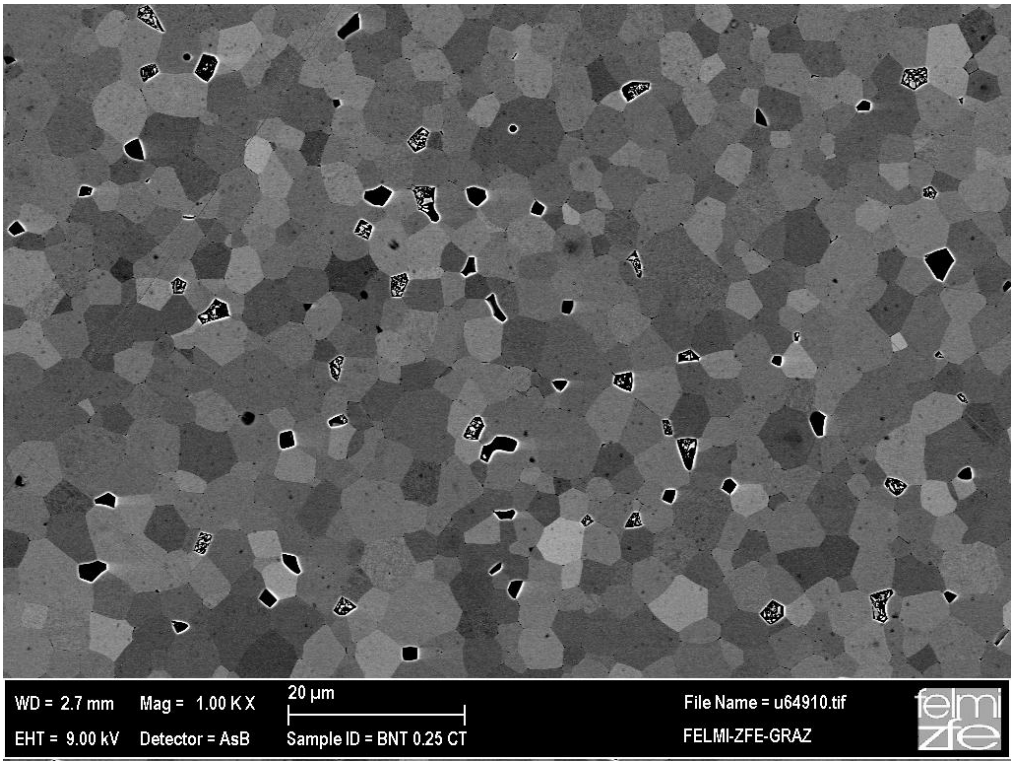


Figure 75: Microstructure of BNT-0.25CT.

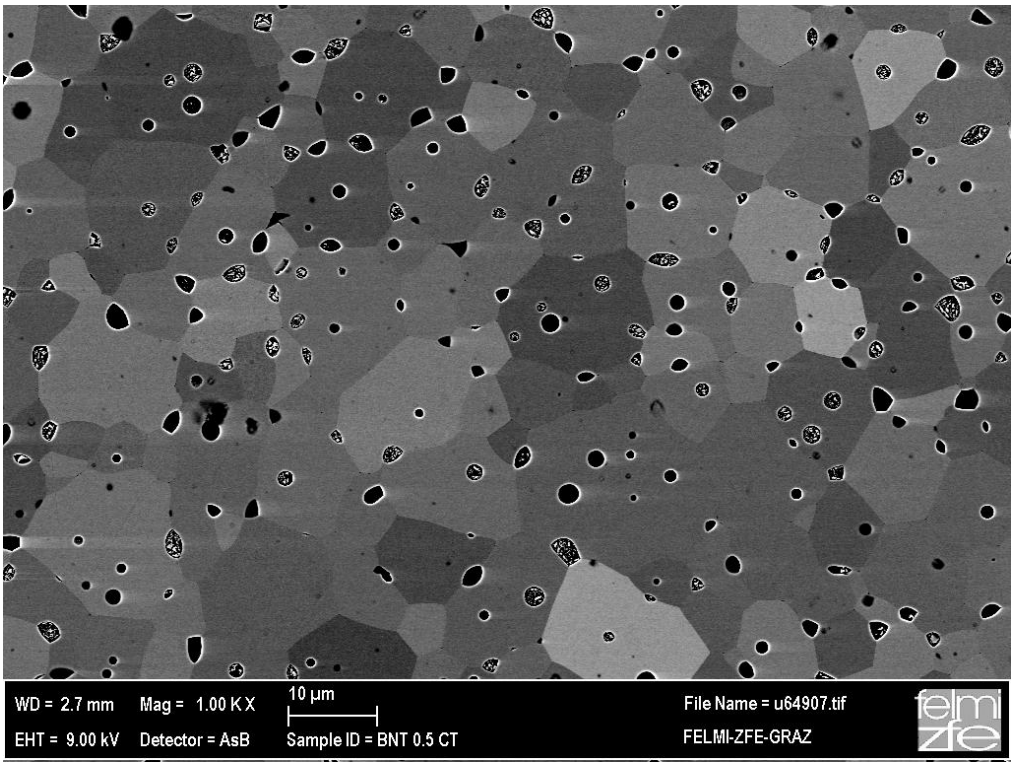


Figure 76: Microstructure of BNT-0.5CT.

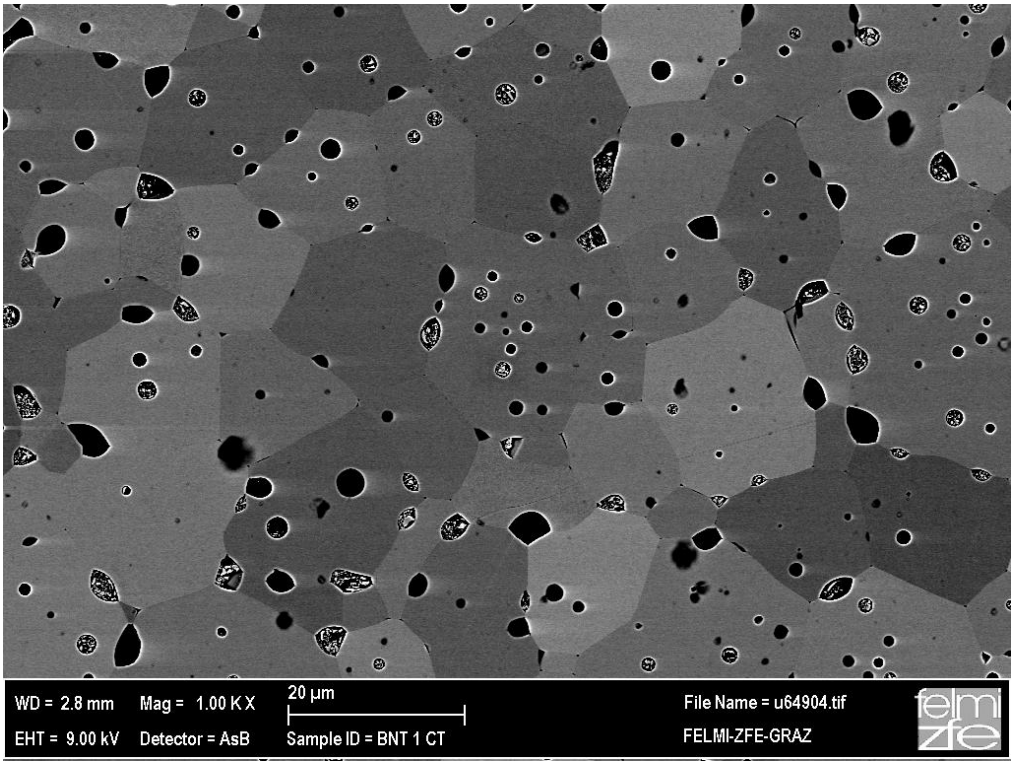


Figure 77: Microstructure of BNT-1CT.

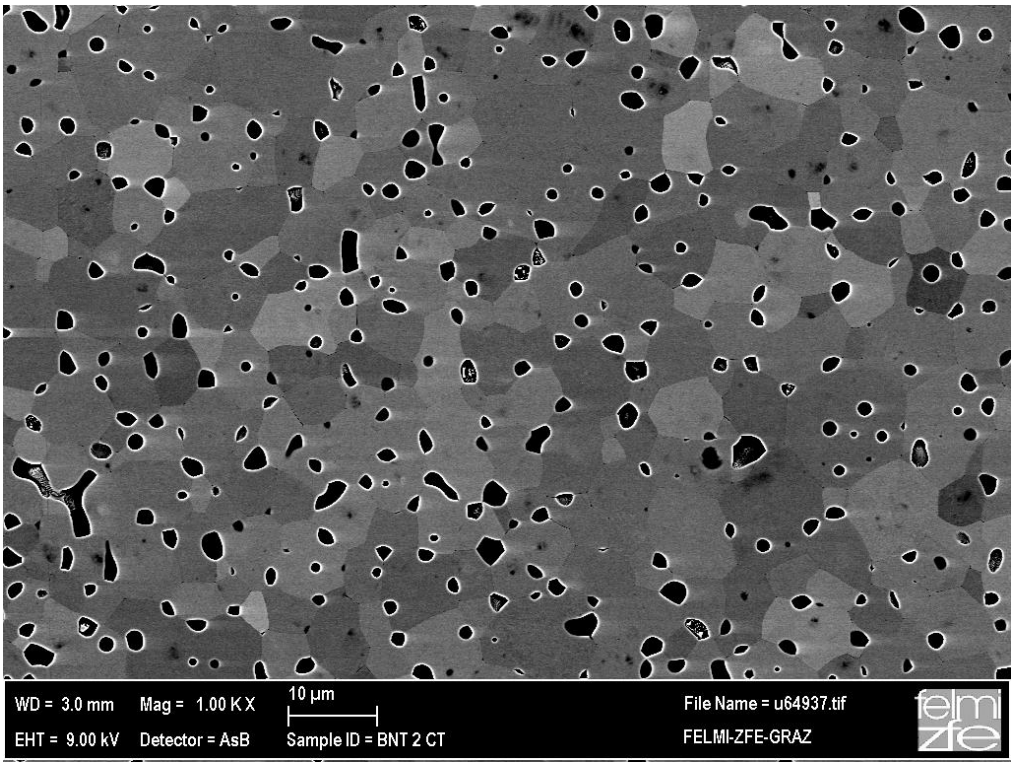


Figure 78: Microstructure of BNT-2CT.

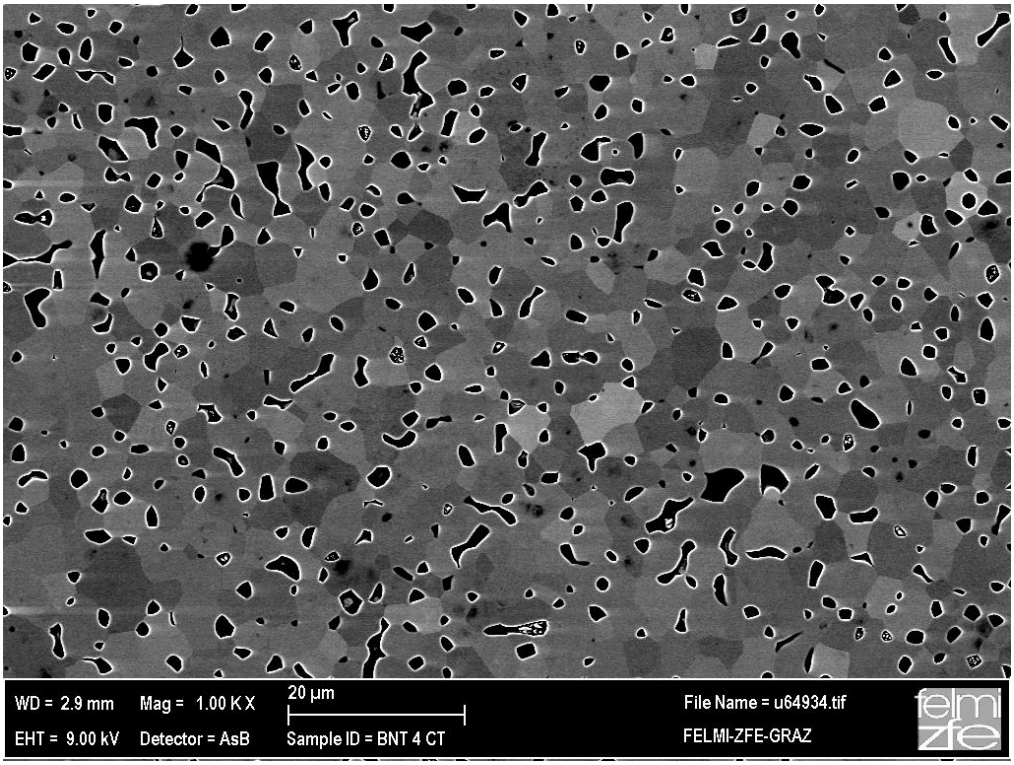


Figure 79: Microstructure of BNT-4CT.

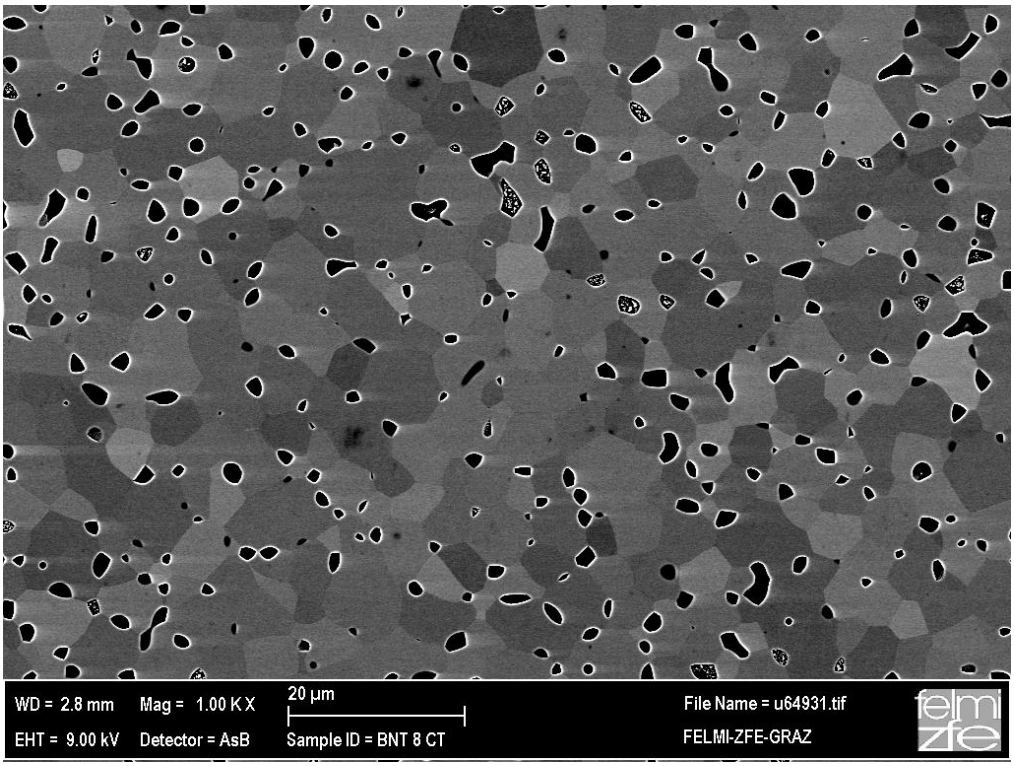


Figure 80: Microstructure of BNT-8CT.

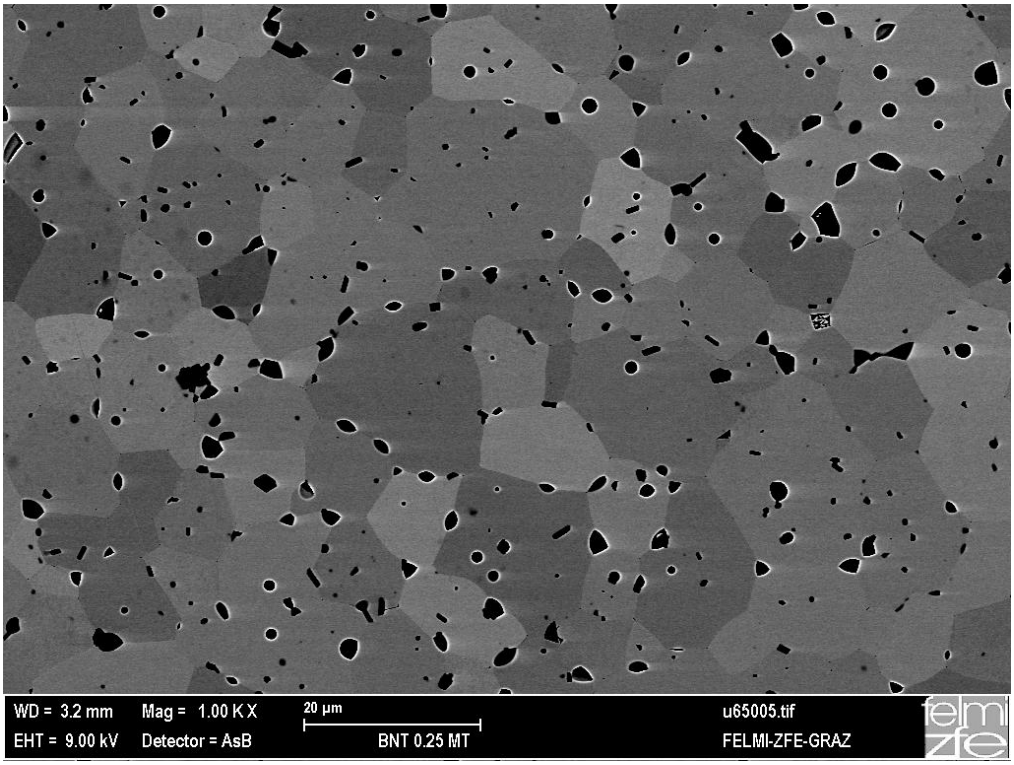


Figure 81: Microstructure of BNT-0.25MT.

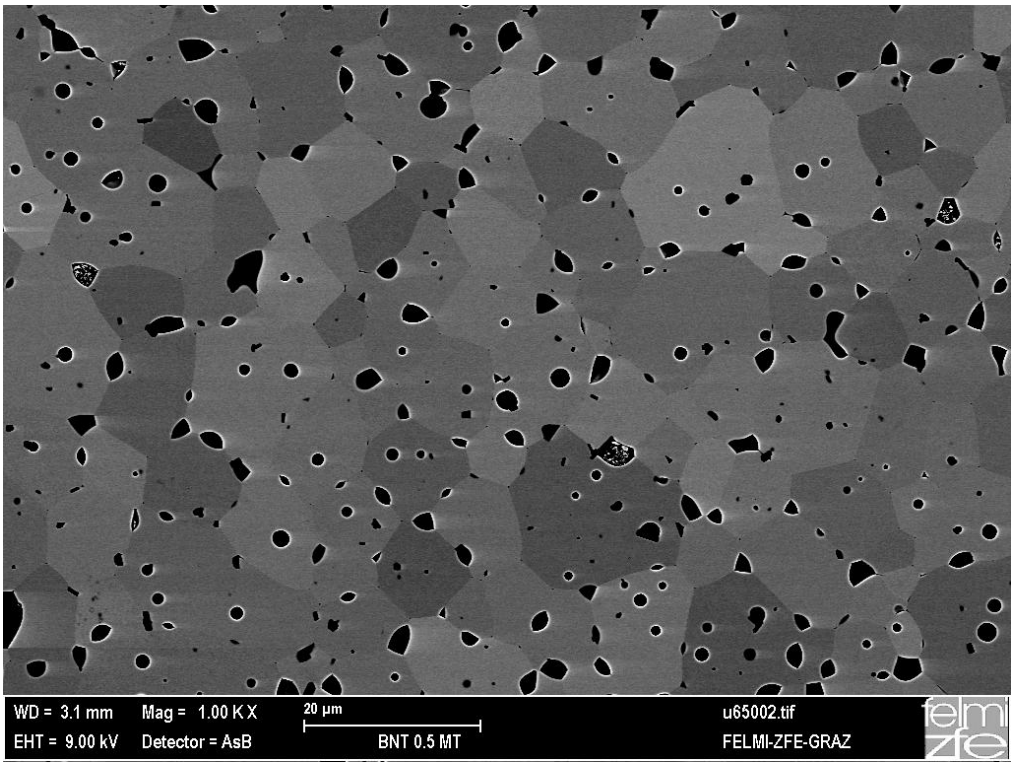


Figure 82: Microstructure of BNT-0.5MT.

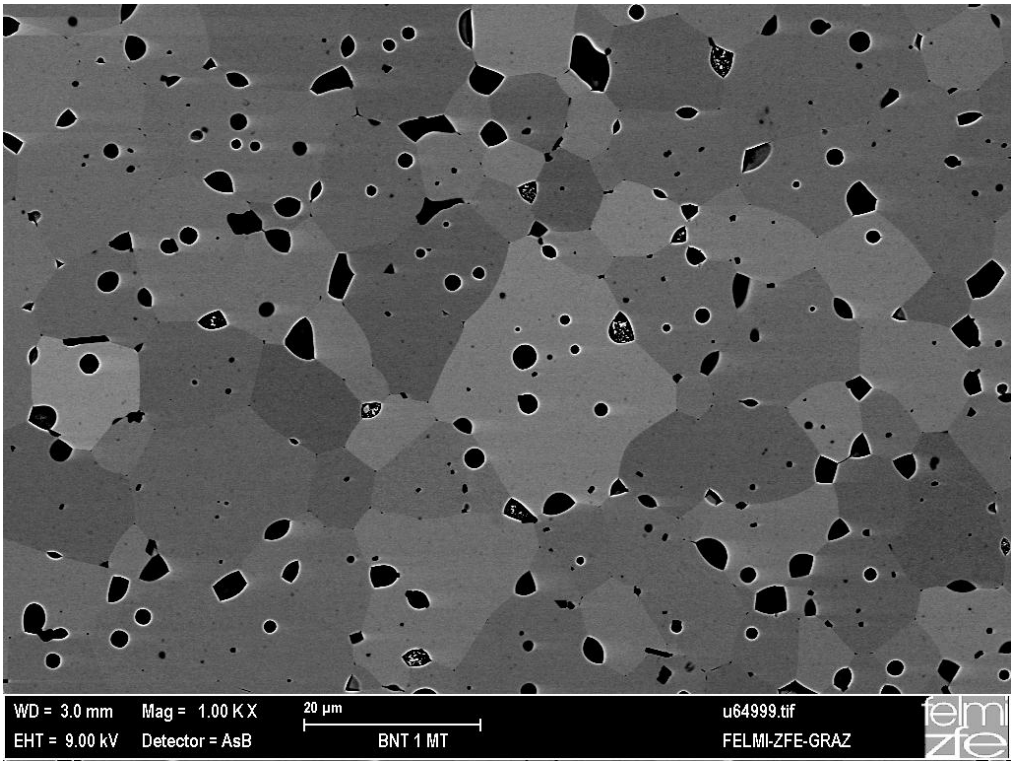


Figure 83: Microstructure of BNT-1MT.

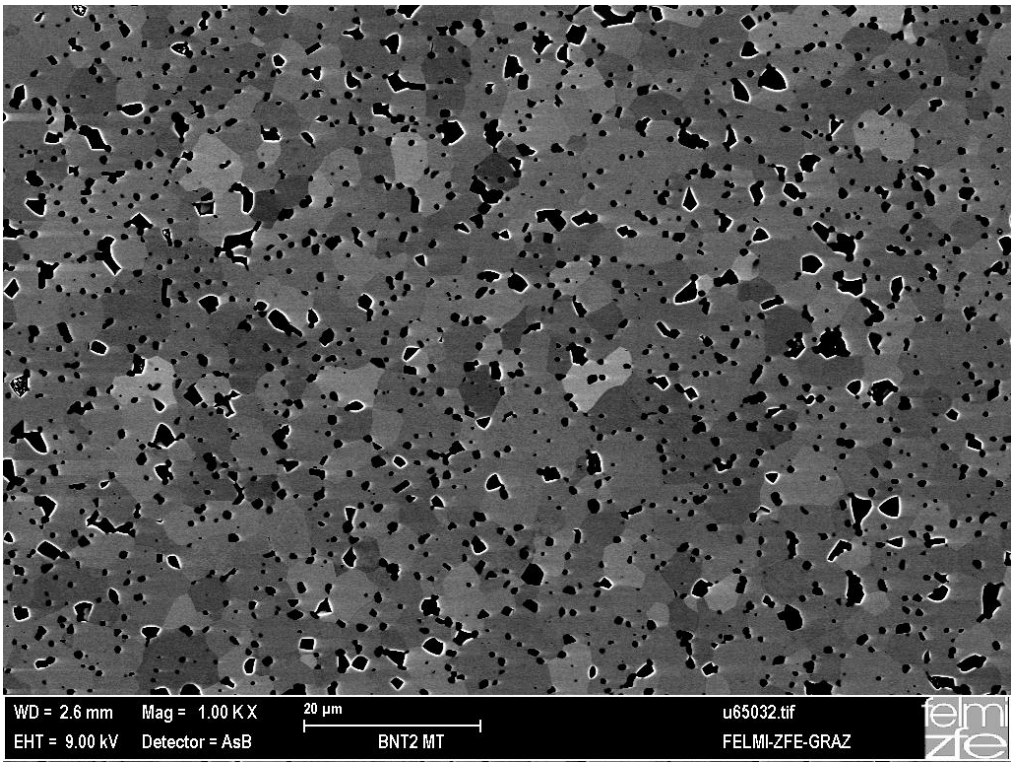


Figure 84: Microstructure of BNT-2MT.

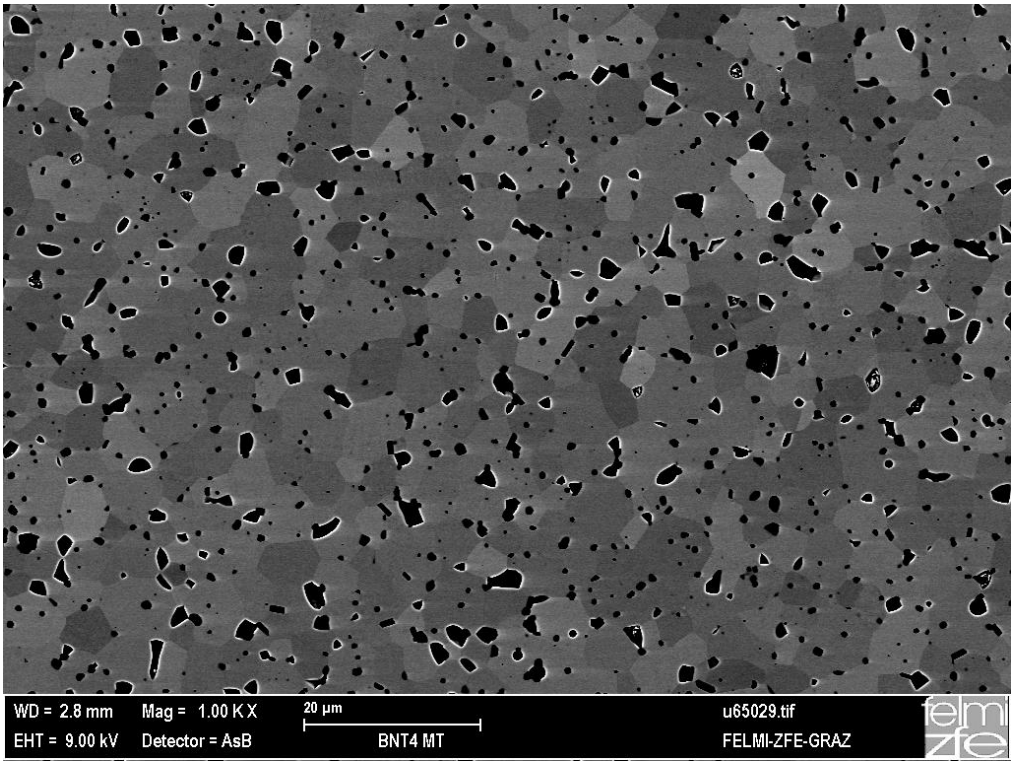


Figure 85: Microstructure of BNT-4MT.

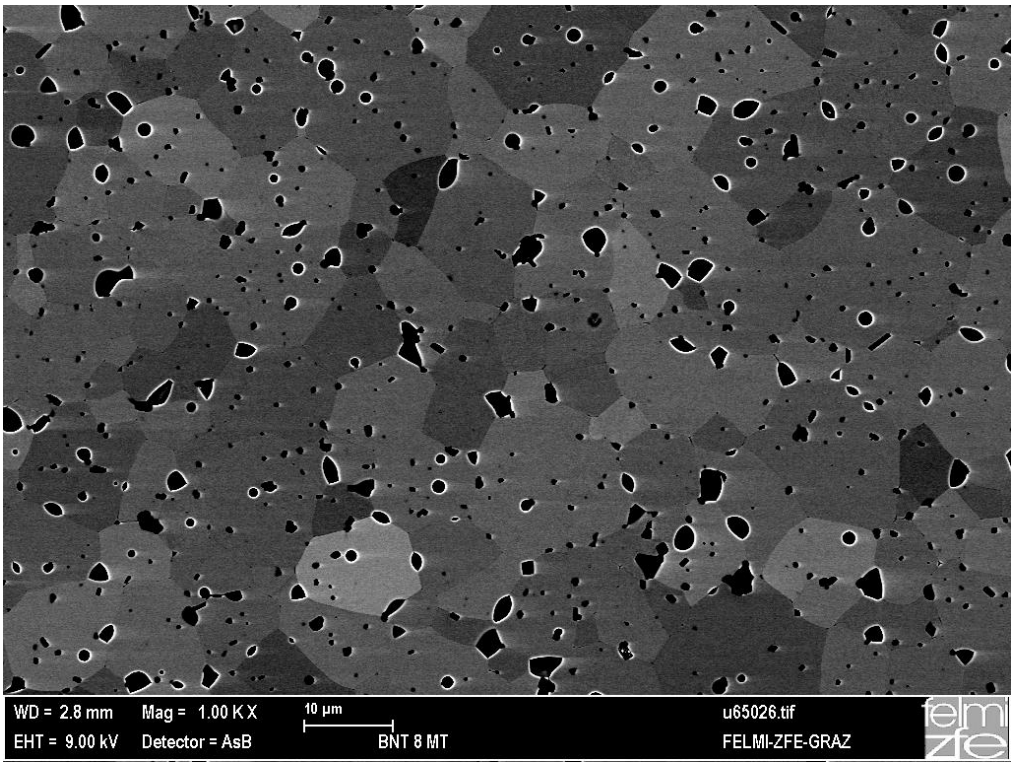


Figure 86: Microstructure of BNT-8MT.